



저작자표시-비영리-변경금지 2.0 대한민국

이용자는 아래의 조건을 따르는 경우에 한하여 자유롭게

- 이 저작물을 복제, 배포, 전송, 전시, 공연 및 방송할 수 있습니다.

다음과 같은 조건을 따라야 합니다:



저작자표시. 귀하는 원저작자를 표시하여야 합니다.



비영리. 귀하는 이 저작물을 영리 목적으로 이용할 수 없습니다.



변경금지. 귀하는 이 저작물을 개작, 변형 또는 가공할 수 없습니다.

- 귀하는, 이 저작물의 재이용이나 배포의 경우, 이 저작물에 적용된 이용허락조건을 명확하게 나타내어야 합니다.
- 저작권자로부터 별도의 허가를 받으면 이러한 조건들은 적용되지 않습니다.

저작권법에 따른 이용자의 권리는 위의 내용에 의하여 영향을 받지 않습니다.

이것은 [이용허락규약\(Legal Code\)](#)을 이해하기 쉽게 요약한 것입니다.

[Disclaimer](#)

理學碩士 學位論文

**Pseudo-antiperovskite 구조인 Li_2OHCl 계의
이온전도도와 전기화학적 안정성 연구**

Study of ionic conductivity and electrochemical
stability for Li_2OHCl systems with
pseudo-antiperovskite structure

蔚山大學校大學院

化學科

李容碩

Pseudo-antiperovskite 구조인 Li_2OHCl 계의

이온전도도와 전기화학적 안정성 연구

Study of ionic conductivity and electrochemical
stability for Li_2OHCl systems with
pseudo-antiperovskite structure

指導教授 류광선

이 論文을 理學碩士學位 論文으로 제출함


2017年 12月

蔚山大學校大學院

化學科

李容碩

李容碩의 理學碩士學位 論文을 認准함

審査委員 정재훈 

審査委員 오은석 

審査委員 류광선 

蔚山大學校大學院

2017년 12

Acknowledgement

2015년 1월 5일에 정식으로 들어와 3년이라는 시간이 지났습니다. 그동안 정말 많이 웃기도 하고 힘들기도 하고 제 인생에 있어 버라이어티한 시간이었던 것 같습니다. 우선 제일 먼저 3년동안 저에게 정말 많은 경험을 쌓도록 기회를 주신 류광선 교수님께 정말 감사하다는 말씀을 드리고 싶습니다. 교수님을 만나 인연을 맺어 무료했던 제인생에 있어 새로운 터닝 포인트가 된 것 같습니다. 교수님께 배운 철학, 교육 잘 되새기면서 살아 가겠습니다. 정말 감사합니다. 제가 실험실에 막내로 들어왔을 때 곧 졸업이었던 정의형에게는 많은 도움을 받은 것 같습니다. 졸업하시고도 실험실에 애정이 많은 형 덕분에 위기였던 실험실 분위기도 계속 유지할 수 있었고 형이 울산에 안 계셨으면 정말 힘든 1년이 되었을 거예요. 항상 오실 때 맞난것도 많이 사오시고 후배들 격려도 해주셔서 정말 감사드립니다. 가끔 제가 없는 일요일에 저를 찾으시던 원근이 형. 자주 보지는 못하지만 형의 그 푸근한 이미지와 재미있는 입담으로 항상 볼때마다 편하게 해주셔서 감사합니다. 그리고 제 기억속의 만누나 다정이 누나. 처음 들어왔을 때 누나에게 혼도 많이 났지만 그만큼 저에게 많은 관심과 제가 잘 적응할 수 있는 분위기를 만들어주셔서 감사합니다. 졸업 후에도 제가 연락드릴때마다 반갑게 받아주셔서 너무 감사해요. 자주 연락 못드린건 죄송합니다... 앞으로는 자주 할 수 있도록 할게요! 그 다음으로는 동기이자 실험실 선배였던 희원씨. 너 덕분에 정말 어색할 수 있었던 처음이 너무 힘들지 않고 지나갈 수 있었던 것 같아. 항상 긍정적이고 똑부러진 모습으로 실험실 분위기를 만들어주던 너의 모습이 아직도 생생하구나. 너가 실험실에 날 끌고 와줘서 이런 멋진 경험을 할 수 있었던 것 같아 정말 고마워. 귀여운 외모와는 달리 시크한 분위기를 풍기던 성훈이형. 형의 걱정 덕분에 제가 무사히 졸업하는 것 같아요. 제가 이상한 질문이나 부탁을 해도 들어줘서 고마워요. 졸업후에도 포항 갈때마다 볼 수 있어서 정말 좋은 것 같아요. 형한테도 진짜 많은 도움을 받았는데 취업하면 거하게 쓰겠습니다. 앞으로도 편하게 연락하고 우리만의 계를 만들어 봅시다. 호탕하게 웃으며 실험실 분위기를 밝게 만들어주던 후배이자 실험실 선배 다정이. 너한테는 혼도 많이 났지만 그만큼 배운것도 많고 너 덕분에 남자만 있을 뻔한 삭막한 실험실을 모면할 수 있었던 것 같아. 2년차가 되고 후배들을 가르쳐보니 너의 심정을 알 것 같더라. 너와 성훈이형의 장점을 잘 조합해서 내 나름대로 후배들을 가르친다고 했는데 잘되었는지는 잘 모르겠다. 아무튼 졸업후에도 나의 졸업을 신경써주고 연락해줘서 너무 고마워. 우리 계를 만들어보자구나. 그리고 제일 먼저 들어온 후배 수연이. 매사에 있어 의욕은 없지만 내가 가르치고 지시하는데로 잘 따라 줘서 고마워. 특히 영진이와 내가 의사소통이 잘 안될 때 중간에서 통역해줘서 정말 고마워. 삭막할 뻔한 실험실에 유일한 꽃이 되주어 정말 고맙다. 앞으로는 실험실을 이끌어 가야할텐데 걱정이 많지만 잘 할 수 있을 거야. 영진이를 잘 부탁해. 투머치 토크 영진이. 너한테 정말 혼도 많이 났지만 그것은 다 너를 위해서 한말이니 나쁘게 생각하지 않았으면 한다. 너도 정말 걱정이 많이 되지만 정말 열심히 하는 만큼 잘 될거라 믿는다. 교수님을 잘 보필하도록 하거라. 술땡기면 연락해라 취업하면 자주 사줄게. 그리고 저와 같이 생활은 하지않았지만 많은 조언과 격려를 해주시는 SMDL 선배님들께 정말 감사의 말씀 드립니다. 멋진 선배님들 보며 저도 그렇게 될 수 있도록 노력 하겠습니다. 마지막으로 저를 27년동안 지극 정성으로 저의 몸과 정신을 케어해주신 우리 촌데레 엄마, 투머치 토크이긴 하지만 항상 제가 굶은 일이 없게 힘들게 돈 버시면서 지원해주시고 항상 믿어주시는 아버지, 27년동안 못난 아들 항상 믿어주고 조건 없는 사랑을 베풀어주셔서 정말 너무 감사드립니다. 두 분의 은혜에 보답하도록 덜 불효자가 되도록 끊임없이 노력하고 행복하게 사는 모습 꼭 보여드릴게요!

Abstract

Recently, Li_3OX ($\text{X}=\text{Cl}, \text{Br}$) called lithium rich antiperovskite electrolyte have been studied by Los-Alamos Lab. Because the materials have low melting point and high electrochemical stability, these materials have showed low interface resistance causing good ionic conductivity (10^{-6} - 10^{-3} Scm^{-1}) by melting method and high anodic electrochemical stability. But, the materials have also showed air sensitivity and difficult synthesis conditions. Li_2OHX ($\text{X}=\text{Cl}, \text{Br}$) replaced from one Li to one H have some advantages such as short time and low temperature for calcination but showed low ionic conductivity. To overcome this problem, we investigated $\text{Li}_2(\text{OH})_{0.9}\text{X}_{0.1}\text{Cl}$ and $\text{Li}_2\text{OH}_{0.8}\text{X}_{0.2}\text{Cl}$ ($\text{X}=\text{F}$ and Br) to study the size effect of halogens and improved ionic conductivity and electrochemical stability mechanism by the substitution at the doping site.

The substituted materials exhibited the improved electrochemical stability and Li^+ conductivity than Li_2OHCl which is pristine material. Among these materials, $\text{Li}_2(\text{OH})_{0.9}\text{F}_{0.1}\text{Cl}$ showed the higher chemical and electrochemical stability due to strong chemical binary bond such as Li-F and H-F than Li-Br and H-B. $\text{Li}_2(\text{OH})_{0.9}\text{Br}_{0.1}\text{Cl}$ also showed highest Li^+ conductivity because of larger interstitial site, phonon softening, and low OH^- concentration. Comparison with the Li^+ conductivity of $\text{Li}_2(\text{OH})_{0.9}\text{F}_{0.1}\text{Cl}$ and $\text{Li}_2\text{OHCl}_{0.8}\text{Br}_{0.2}$, the Li^+ conductivity of the antiperovskite electrolytes is more influenced by the concentration of OH than other mechanisms.

Contents

Acknowledgement -----	I
Abstract -----	II
Contents -----	III
List of tables -----	VII
List of Figures -----	VIII

Chapter 1. Introduction

1-1. Lithium secondary batteries -----	1
1-1-1. Composition of lithium secondary batteries -----	1
1-1-2. Principle of lithium secondary batteries -----	2
1-1-3. Properties and limitation of organic liquid electrolyte -----	3
1-2. Ceramic solid electrolytes -----	7
1-2-1. Properties of ceramic solid electrolytes -----	7
1-2-2. Li ⁺ diffusion mechanism of ceramic solid electrolyte -----	9
1-2-3. Representative ceramic solid electrolytes -----	13
1-2-3-1. NASION -----	13
1-2-3-2. Perovskite -----	15
1-2-3-3. Garnet -----	17
1-2-3-4. LISICON -----	19
1-2-4. Requirements for commercialized solid electrolyte in lithium secondary batteries -----	23
1.3. Lithium rich antiperovskites -----	27

1-3-1. Introduction of lithium rich antiperovskites -----	27
1-3-1-1. Crystal structure and lithium diffusion mechanism-----	27
1-3-3-2. Strategy for increasing lithium ion conductivity of antiperovskites -----	31
1-3-2. Anodic stability of lithium rich antiperovskites-----	34
1-3-3. Grain boundary control by melting method from antiperovskite materials -----	36
1-3-4. Pseudo antiperovskite materials for simple synthesized solid electrolytes -----	39
1.4. Purpose-----	45
References -----	46

Chapter 2. General experimental

2-1. Physical characterization -----	51
2-1-1. X-ray diffraction (XRD) -----	51
2-1-2. Fourier transform-infrared spectroscopy (FT-IR) -----	55
2-1-3. Field emission scanning electron microscopy (FE-SEM) -----	55
2-1-4. Thermogravimetric analysis (TGA) and differential scanning calorimeter (DSC) --	56
2-2. Electrochemical analysis -----	58
2-2-1. Cell assembly -----	58
2-2-2. Cyclic voltammetry -----	58
2-2-3. Direct current cycling (DC-cycling) -----	59
2-2-4. Electrochemical impedance spectroscopy (EIS) -----	60
Reference -----	63

Chapter 3. Study of electrochemical stability and ionic conductivity for Li_2OHCl

3-1. Introduction	64
3-2. Experimental	65
3-2-1. Synthesis of Li_2OHCl	65
3-2-2. Characterization	67
3-2-3. Cell assembly	68
3-2-4. Electrochemical analysis	70
3-3. Results and discussion	70
3-3-1. Characterization	70
3-3-2. Electrochemical analysis	77
3-4. Conclusion	87
Reference	88

Chapter 4. Study of ionic conductivity and electrochemical stability for $\text{Li}_2(\text{OH})_{0.9}\text{X}_{0.1}\text{Cl}$ and $\text{Li}_2\text{OHCl}_{0.8}\text{X}_{0.2}$ ($\text{X}=\text{F}, \text{Br}$)

4-1. Introduction	89
4-2. Experimental	90
4-2-1. Synthesis of $\text{Li}_2(\text{OH})_{0.9}\text{X}_{0.1}\text{Cl}$ and $\text{Li}_2\text{OHCl}_{0.8}\text{X}_{0.2}$	90
4-2-2. Characterization	90
4-2-3. Cell assembly	91
4-2-4. Electrochemical analysis	91
4-3. Results and discussion	92

4-3-1. Characterization -----	92
4-3-2. Electrochemical analysis -----	104
4-4. Conclusion -----	116
Reference -----	118
Chapter 5. Summary -----	119

List of tables

Table 1.1 Phase equilibria and decomposition energies for $\text{Li}_{10\pm 1}\text{MP}_2\text{X}_{12}$.

Table 1.2 Ionic conductivity and chemical properties of lithium rich antiperovskites.

Table 1.3 Synthesis conditions of lithium rich antiperovskites.

Table 4.1 Melting points and calculated mass loss of antiperovskites.

Table 4.2 Bond dissociation energies of the binary bonding related with F and Br substituted antiperovskites.

Table 4.3 List of the calculated electronic conductivities of the antiperovskites.

Table 4.4 Calculated Li^+ conductivities and activation energies of the antiperovskite materials.

List of figures

Figure 1.1 Illustration of operating principle of lithium secondary batteries.

Figure 1.2 Schematic open-circuit energy diagram of lithium cell.

Figure 1.3 Schematic illustration of lithium diffusion mechanism of solid electrolyte.

Figure 1.4 Schematic illustration of lithium diffusion mechanism of by Schottky migration and Frenkel migration.

Figure 1.5 Structural schematic of NASICON-like.

Figure 1.6 Structural schematic of perovskite (LLTO).

Figure 1.7 Structural schematic of (a) garnet and (b) garnet-related $\text{Li}_5\text{La}_3\text{M}_2\text{O}_{12}$.

Figure 1.8 Structural schematic of LISICON like.

Figure 1.9 Nyquist plot of LAGP with fit result.

Figure 1.10 Calculated electrochemical stability window of solid electrolytes.

Figure 1.11 Schematic illustration of structure for lithium rich antiperovskites.

Figure 1.12 Schematic illustration of lithium diffusion mechanism in the structure of lithium rich antiperovskites.

Figure 1.13 Schematic illustration of structural model about doped Li_3OX materials.

Figure 1.14 Example DC-cycling data of Li_3OCl .

Figure 1.15 (a) Example DSC data of Li_3OCl and (b) schematic illustration of melting method of antiperovskites.

Figure 1.16 Energy difference between Li_3OCl and the starting materials ($\text{Li}_2\text{O} + \text{LiCl}$)

as a function of cell volume.

Figure 1.17 SEM images of Li/Li₂OHCl/Li cell after 160 charge/discharge cycles.

Figure 2.1 Bragg reflection on a set of atomic planes.

Figure 2.2 Table of seven crystal system and 14 Bravais lattice.

Figure 2.3 (a) The Li⁺ diffusion mechanism of lithium ion batteries, (b) Nyquist plot of an electrode, and (c) equivalent circuit from the Nyquist plot.

Figure 3.1 Schematic illustration for synthesis procedure of Li₂OHCl.

Figure 3.2 (a) Configurations of the symmetric cells for cyclic voltammetry, (b) DC-cycling, and (c) EIS measurements.

Figure 3.3 (a) XRD patterns of Li₂OHCl and (b) the Li₂OHCl samples exposed to air depend on time.

Figure 3.4 (a) FT-IR spectra of Li₂OHCl and (b) the Li₂OHCl samples exposed to air depend on time.

Figure 3.5 (a) TGA and (b) DSC data of Li₂OHCl from 25°C to 600 °C with heating rate 5°C/min in N₂ atmosphere.

Figure 3.6 (a) SEM images of Li₂OHCl pellet, (b) mapping image for overall elements in Li₂OHCl pellet, (c) oxygen, (d) chloride, and (e) result from EDS analysis of the pellet.

Figure 3.7 (a) Cyclic voltammetry for Li₂OHCl at scan rate 0.5 mV/s from -1V to 6V and (b) the Hebb-Wagner polarization curves obtained from the cell Li/Li₂OHCl/SUS

Figure 3.8 Results of DC-cycling tests of the symmetric cell Li/Li₂OHCl/Li with a applied current density 1mA/cm² at (a) 25°C and (b) 140°C for 72hr.

Figure 3.9 (a) Disassembled symmetric cells Li/Li₂OHCl/Li after DC-cycling tests at 25°C and (b) 140°C, (c) SEM images of Li₂OHCl pellet, (d) SEM images of the surface of SEI layer, (e) SEM images of the surface in the red box, and (f) mapping images of the red box.

Figure 3.10 (a) Results of EDS analysis for the SEI layer and (b) mapping images.

Figure 3.11 (a) schema for composition of resistance of solid electrolyte, (b) Nyquist plot from EIS data of Li₂OHCl at 25°C, (c) the plot with increasing temperature 25°C to 145°C, and (d) Arrhenius plot of the total conductivity of the antiperovskite materials with In foil as electrodes; the activation energy E_a is derived by linear fitting of $\log\sigma T$ versus $1/T$.

Figure 4.1 XRD patterns of the antiperovskite materials of (a) Li₂OHCl, (b) Li₂(OH)_{0.9}F_{0.1}Cl, (c) Li₂OHCl_{0.8}F_{0.2}, (d) Li₂(OH)_{0.9}Br_{0.1}Cl, and (e) Li₂OHCl_{0.8}Br_{0.2}.

Figure 4.2 Magnified reflections magnified reflections around $2\theta = 32^\circ$ in the XRD patterns of (a) Li₂OHCl, (b) Li₂(OH)_{0.9}F_{0.1}Cl, (c) Li₂OHCl_{0.8}F_{0.2}, (d) Li₂(OH)_{0.9}Br_{0.1}Cl, and (e) Li₂OHCl_{0.8}Br_{0.2}.

Figure 4.3 FT-IR spectra of the antiperovskites of (a) Li₂OHCl, (b) Li₂(OH)_{0.9}F_{0.1}Cl, (c) Li₂OHCl_{0.8}F_{0.2}, (d) Li₂(OH)_{0.9}Br_{0.1}Cl, and (e) Li₂OHCl_{0.8}Br_{0.2}.

Figure 4.4 Results of (a) TGA and (b) DSC (A: Li₂OHCl, B: Li₂(OH)_{0.9}F_{0.1}Cl, C: Li₂OHCl_{0.8}F_{0.2}, D: Li₂(OH)_{0.9}Br_{0.1}Cl, and E: Li₂OHCl_{0.8}Br_{0.2}).

Figure 4.5 SEM image, mapping images, and EDS result of the (a) Li₂(OH)_{0.9}F_{0.1}Cl and (b) Li₂OHCl_{0.8}F_{0.2} pellets.

Figure 4.6 SEM image, mapping images, and EDS result of (a) the Li₂(OH)_{0.9}Br_{0.1}Cl and (b) Li₂OHBr_{0.8}F_{0.2} pellets.

Figure 4.7 (a) Cyclic voltammetry for Li₂OHCl at a scan rate 0.5 mV/s from -1V to 6V

and (b) the Hebb-Wagner polarization curves obtained from the cell Li/Li₂OHCl/SUS (A: Li₂OHCl, B: Li₂(OH)_{0.9}F_{0.1}Cl, C: Li₂OHCl_{0.8}F_{0.2}, D: Li₂(OH)_{0.9}Br_{0.1}Cl, and E: Li₂OHCl_{0.8}Br_{0.2}).

Figure 4.8 Results of DC-cycling tests for the symmetric cell Li/Li₂OHCl/ /Li with applied current density 1 mA/cm² at 140°C for 72hr (a) Li₂(OH)_{0.9}F_{0.1}Cl, (b) Li₂OHCl_{0.8}F_{0.2}, (c) Li₂(OH)_{0.9}Br_{0.1}Cl, and (d) Li₂OHCl_{0.8}F_{0.2}.

Figure 4.9 Results of EDS and mapping images of the symmetric cell Li/electrolyte/Li after DC-cycling tests at 140°C: (a) Li₂(OH)_{0.9}F_{0.1}Cl, (b) Li₂OHCl_{0.8}F_{0.2}, (c) Li₂(OH)_{0.9}Br_{0.1}Cl, and (d) Li₂OHCl_{0.8}Br_{0.2}.

Figure 4.10 Results of (a) Nyquist plot from EIS measurements for the antiperovskite electrolytes and (b) Arrhenius plot of the total conductivity of the antiperovskite materials between 25°C and 145°C with In foil as electrodes; the activation energy E_a is derived by linear fitting of $\log\sigma T$ versus $1/T$.

Figure 4.11 Results of Nyquist plot from EIS measurements for (a) Li₂(OH)_{0.9}F_{0.1}Cl, (b) Li₂OHCl_{0.8}F_{0.2}, (c) Li₂(OH)_{0.9}Br_{0.1}Cl, and (d) Li₂OHCl_{0.8}Br_{0.2} with a range of the temperature from 25°C and 145°C.

Chapter 1. Introduction

1-1. Lithium secondary batteries

Since rechargeable lithium secondary batteries were firstly developed and commercialized by Sony in 1991, the batteries have been used in various electronic devices such as cell phone, laptop, and many portable electronic devices. Among the rechargeable batteries commercialized, lithium secondary batteries have showed the highest energy (250Wh Kg^{-1}), powder density, and long cycle life. Recently, the batteries have been applied to large scale energy devices such as electrical vehicles (EVs), hybrid electrical vehicles (HEVs), and energy storage system (ESS). However, the current lithium secondary batteries have some drawbacks to be used to large scale devices. Among many problems, the important thing is the safety of the batteries. There are some examples about explosion accident. The smartphones of Samsung and Apple caused explosion in 2016. For examples about large scale devices, EVs of Tesla were also exploded due to the batteries in the vehicles in 2013 and 2016. To solve this problem, many studies and efforts are needed.

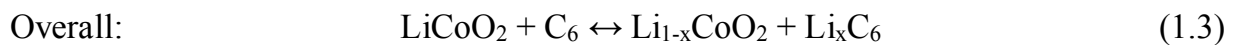
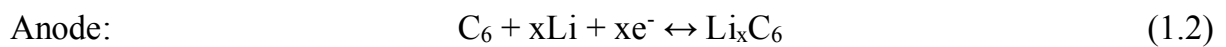
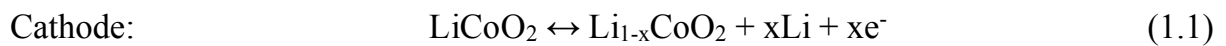
1-1-1. Composition of lithium secondary batteries

Basically, lithium secondary batteries are composed of cathode, anode, separator, and organic liquid electrolyte. Generally, the conventional cathode materials are intercalation materials involving 1-D olivine (LiFePO_4), 2-D layered (LiCoO_2), and 3-D spinel structures (LiMn_2O_4). Typically, LiCoO_2 have been used due to its working voltage (3.0-4.5V vs. Li/Li^+), high energy density, and cycle stabilities. Representatively,

there are anode materials such as carbon graphite, SiO₂, and Li₄Ti₅O₁₂. The carbon base materials have been used due to its large lithium storage capability, low cell voltage (0-2.0V vs. Li/Li⁺), and low volume exchange during charging and discharging. Separator to allow penetrate electrolyte and prevent short between cathode and anode is made by using polyethylene and polypropylene porous thin films. Finally, organic liquid materials such as ethylene carbonate and di-ethyl or methyl carbonate including lithium salt (LiPF₆) are used due to its high ionic conductivity in organic electrolyte and broad stability voltage window (0-4.5V vs. Li/Li⁺).

1-1-2. Principle of lithium secondary batteries

The operating principle of lithium secondary battery are presented in Figure 1.1. For example, at charging step, the cathode and anode materials are oxidized and reduced respectively first. The chemical reactions during charging and discharging can be represented as follows equations.



Throughout this chemical reaction, the electrons move through the external circuit connected to the current collectors to anode materials and make them reduce. After chemical reaction of two electrode materials, lithium ions are released from cathode to maintain electronic charge neutrality of the materials. The ions released are diffused and

intercalated to surface and structure of an anode reduced by accept electrons. During this step, the chemical energy made by the chemical reaction can be converted and stored to electronic energy by followed Nernst equation (eq. 1.4).

$$\Delta G = -nFE \quad (1.4)$$

where G is Gibbs energy, n is number of electrons, F is Faraday's constant number, and E is electric potential. This equation means that electric potential energies are proportional to chemical energies, which means that large chemical potential difference between cathode and anode induce large electric potential and energy. The electric potential proportioning to chemical energies is called to open circuit voltage (OCV) and is determined within the band gap of the electrolyte, which is determined energy difference between the highest occupied molecular orbital (HOMO) and the lowest unoccupied molecular orbital (LUMO) of the electrolyte in Figure 1.2 [2-4].

1-1-3. Properties and limitation of organic liquid electrolyte

Commercial organic liquid electrolytes consist of mixture of two or more carbonate-based materials and a lithium salt such as ethyl carbonate (EC)/di-methyl carbonate (DMC)=1:1 in 1M LiFP₆. The electrolytes have been applied to many lithium based batteries due to its good dielectric constant and electrochemical stability compare with aqueous electrolyte. But, in order to be applied to the large scale energy devices, the electrolytes must be satisfy several requirements such as: [12]

- 1) Retention of the SEI during charge and discharge
- 2) A Li^+ ion conductivity $\sigma_{\text{Li}} > 10^{-4} \text{Scm}^{-1}$
- 3) An electronic conductivity $\sigma_e < 10^{-10} \text{Scm}^{-1}$
- 4) A transference number $\sigma_{\text{Li}}/\sigma_{\text{total}} \approx 1$, where σ_{total} includes conductivities by other ions in the electrolyte
- 5) Chemical stability over wide temperature ranges

Among these requirements, there are conditions that the organic electrolyte not meet such as low transference number, chemical stability, and electrochemical stability. Usually, lithium salt electrolytes have showed a low transference number of lithium ions (0.3-0.5/1), which occur poor high-rate performances and limits the powder output of the cell [2] due to their dielectric mechanism such as solvation and dissociation. However, the most important thing to solve is safety related with thermal stability and leakage of the liquid types. As the organic electrolytes are decomposed and occur high thermal energy at high temperature, the lithium batteries expand and induce shrinkage of the membrane. Finally, the short between cathode and anode occurs and leads to explosion. To solve these problem, the various types of electrolytes have been developed such as gel-type and solid-state electrolyte due to their no leak properties and good thermal and electrochemical stability.

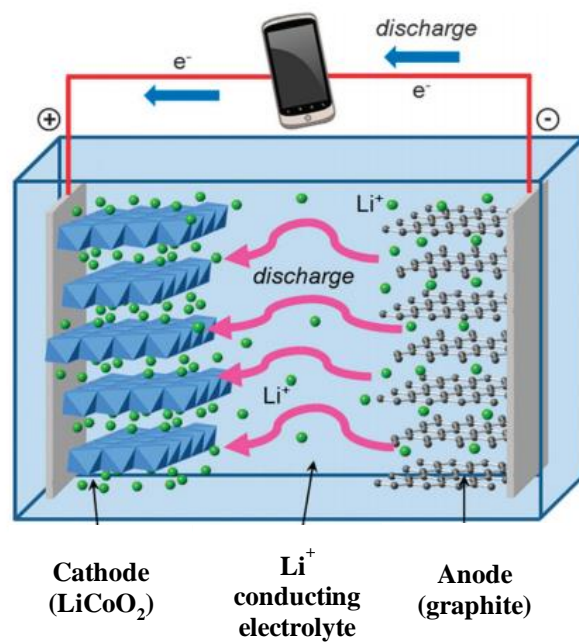


Figure 1.1 Illustration of operating principle of lithium secondary batteries [1].

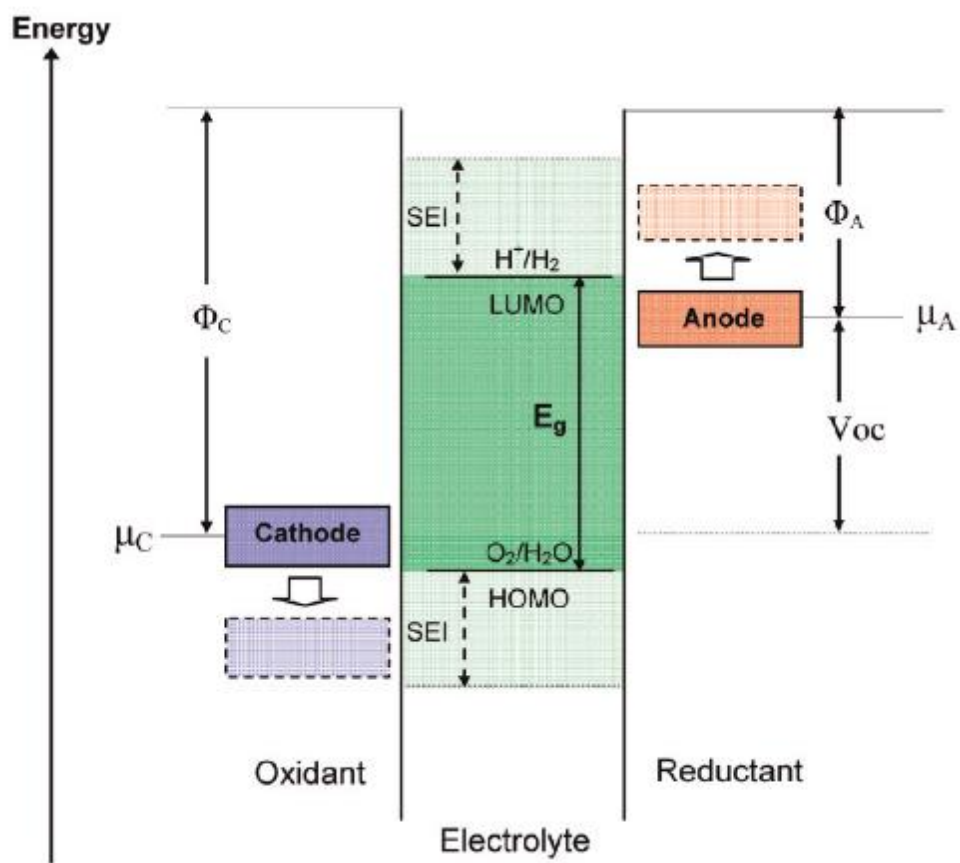


Figure 1.2 Schematic open-circuit energy diagram of lithium cell [2].

1-2. Ceramic solid electrolytes

Recently, solid electrolytes have been applied to broad fields such as smart sensors, microbatteries for some small devices, solid oxide fuel cells, and solid-state batteries for electrical vehicles [1]. Among the fields, the electrolytes for large scale electric devices have been intensively studied due to its attractive advantages for safety of lithium secondary batteries such as its electrochemical and thermal stability [2, 3]. The solid electrolytes are widely divided into ceramics and polymers. In the case of polymer electrolytes, they have good flexibility and also can be flexible batteries and devices. However, the poor mechanical properties and low ionic conductivity offset these electrolytes from practical applications [4-6]. Compared with the polymer electrolytes, ceramic solid electrolytes have been studied actively due to their good safety including strong mechanical strength and good ionic conductivity. There are many kinds of the electrolytes such as lithium hydrides, perovskites, lithium nitrides, LISICON-like (lithium superionic conductor), NASICON-like (sodium superionic conductor), argyrodites, and garnet [1]. As the powerful advantages, one of the ceramic electrolytes, lithium phosphorus oxynitride (LIPION), was applied to lithium secondary batteries as the ceramic electrolyte for high temperature electric vehicle respectively [7].

1-2-1. Properties of ceramic solid-state electrolytes

The ceramic solid electrolytes meet followed requirements before they can be commercialized.

- 1) Strong mechanical strength
- 2) Chemical stability from thermal decomposition [8] and flammable [9]
- 3) High ionic conductivity due to high lithium transference number (-1) compared to aprotic electrolytes (0.2-0.5) [12]
- 4) Stable electrochemical stability window [10]
- 5) Good compatibility with lithium metal batteries due to its Li dendrite suppression properties [11]
- 6) Eco-friendly comparing with organic carbonate base electrolytes

Almost the ceramics satisfy mechanical strength, chemical stability, nonflammable, Li dendrite suppression, and eco-friendly. Especially, the enhanced stability and safety of solid ceramic electrolyte provides new design of current solid-state battery cell simply and easily. Also, the solid electrolytes have high lithium transference number ($\sigma_{Li}/\sigma_{total}$) reducing the effects of concentration polarization from precipitations of the dissolved salt at the anode and depletion at the cathode [12] as the electrolyte is only worked by Li^+ migration compare with the liquid electrolytes including aprotic and lithium salt ions. As the results, lithium secondary battery lifetime and safety are increased [1]. The electrochemical stability window of many ceramic electrolytes is also known stable and wide. Almost the oxide electrolytes showed stable cathodic stability at the voltage window of cathode (5-9V versus Li^+/Li) and not induce self-decomposition during charge-discharge operation unlike the liquid organic electrolytes

[12]. Consequently, the solid electrolytes can suppress repetition of SEI formation and Li^+ consumption, and finally increase life time of lithium secondary batteries.

1-2-2. Li^+ diffusion mechanism of ceramic solid electrolytes

Ceramic solid-state electrolytes are composed with not only mobile ions such as Li^+ but also nonmetal ligands forming polyhedral (4, 6, 8, and 12-fold coordination) and centered metals, which build the skeleton of the crystal structures. The polyhedra is regularly ordered by sharing such as corner or edge sharing and forms the Li^+ tunnel called bottleneck with interstitial between large anions and vacancy from not perfect crystallinity of solid materials due to thermodynamical stabilization [12-15]. The lithium ions are diffused by migration through the bottleneck in the crystal structures, while the liquid electrolytes involve moving solvated lithium ions in the solvent medium (Figure 1.3) [12]. The migration is divided into Schottky and Frenkel migration. The schematic representation is in Figure 1.4 [1]. In the case of Schottky migration, the lithium ions migrate to the vacancy sites randomly. On the contrary, Frenkel migration is operated when lithium ions are diffused to direct interstitial between anions and exchange interstitial site [1]. Compare with the activation energy of the migration, Frenkel migration mechanism requires lower activation energy than Shockey migration.

As the results, the Li^+ conductivity is depended on size and number of bottleneck [16], interstitial, and vacancy sites [17] which reliance on the lattice parameters of unit

cell in the structures with Li^+ concentration. Also, the parameters are changed mobile ion valency and size [1, 18]. For example, the repulsion between same charge ions is increased with increasing ion size and form larger bottleneck size and interstitial. In the case of the ion valency effect, ionic conductivity decreases with increasing valency because the electrostatic interaction between mobile ion and opposite charge ions is increased and decrease the ion diffusion.

Because of simple diffusion mechanism of solid crystal structures, the ionic conductivity of solid electrolytes can be assumed that the diffusion is occurred by only ion migration not electron as followed equation (1.6) with Nernst-Einstein equation (1.5).

$$D = D_0 e^{-E_a/k_B T} \quad (1.5)$$

$$\mu = \frac{D}{k_B T} \quad (1.6)$$

where D is lithium diffusion coefficients, E_a is the activation energy of lithium diffusion, k_B is Boltzmann constant, T is Kelvin temperature, and μ is Li^+ absolute mobility. Therefore, the equation can be expressed as

$$\sigma = \frac{\sigma_0}{T} e^{-E_a/k_B T} \quad (1.7)$$

where σ is ionic conductivity. As the equation is not consider the effect of Li^+ concentration, ionic conductivity is in inverse proportion to the activation energy E_a . Consequently, the ionic conductivity depend on lithium concentration, ion size, and ion valency.

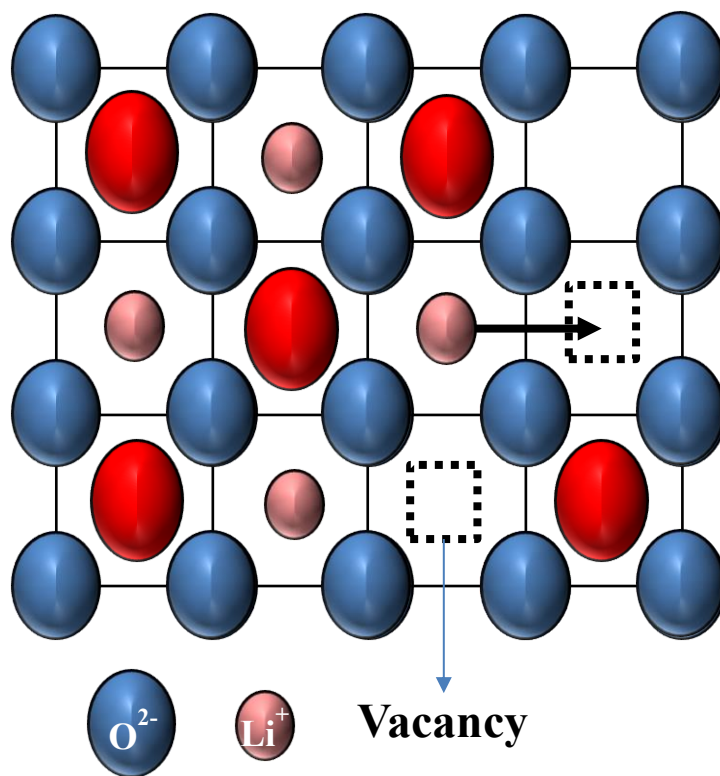


Figure 1.3 Schematic illustration of lithium diffusion mechanism of solid electrolyte.

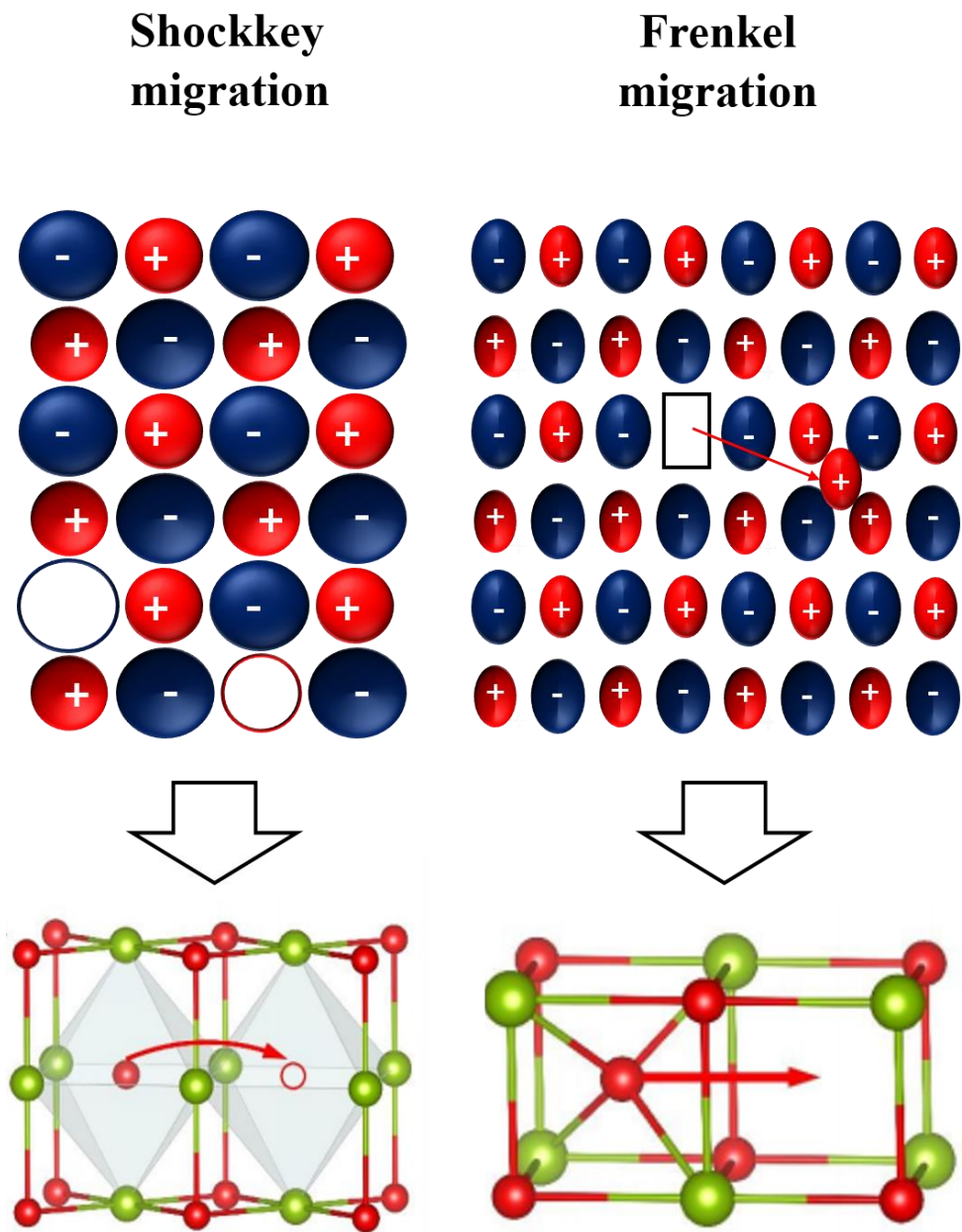


Figure 1.4 Schematic illustration of lithium diffusion mechanism of by Schottky migration and Frenkel migration [1].

1-2-3. Representative ceramic solid electrolyte

1-2-3-1. NASICON

NASICON-like structures are generally known as a rhombohedral unit cell and $R\bar{3}c$ with a few monoclinic and orthorhombic phases [19]. Representatively, $L_{1+6x}M_{4+2-x}M'_{3+x}(PO_4)_3$ phosphates (L = Li or Na and M = Ti, Ge, Sn, Hf, or Zr and M' = Cr, Al, Ga, Sc, Y, In, or La) are composed with MO_6 octahedra connected by corner sharing with PO_4 tetrahedral to form 3D interconnected channels and two types of interstitial positions where mobile cations are distributed in Figure 1.5 [20]. The M1 sites, which are 6-fold coordination, located between two MO_6 octahedral while M2 sites that are 8-fold coordinated and located between two columns of MO_6 octahedra [21]. The lithium ions diffuse from one site to another through bottlenecks.

NASICON-like materials $LiA_2^{IV}(PO_4)_3$ showed ionic conductivity 10^{-5} Scm^{-1} at room temperature in 2009 [22]. To solve size mismatch between Li^+ and TiO_6 octahedra, a few materials have been developed and exhibited improved ionic conductivity such as the $Li_{1.3}Al_{0.3}Ti_{1.7}(PO_4)_3$ (10^{-3} Scm^{-1}) [23]. Also, the materials have high electrochemical oxidative voltage window (-6V versus Li^+/Li) [24] as well as stability from air and moisture. However, the NASICON electrolytes containing Ti are unstable with Li metal at low potentials.

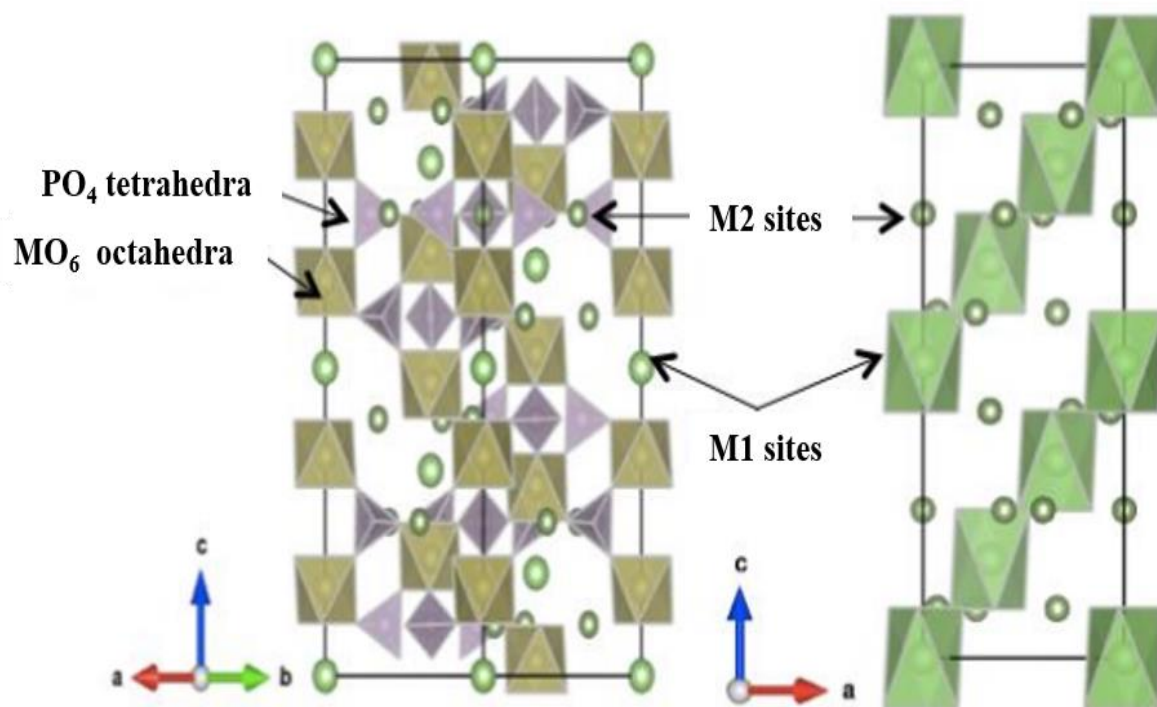


Figure 1.5 Structural schematic of NASION-like [20].

1-2-3-2. Perovskite

Perovskite materials having chemical formula ABO_3 is well known as the representative cubic phase with space group $Pm\bar{3}m$. Among the structural materials, lithium-lanthanum-titanates, $Li_3La_{(2/3)-x} \boxed{d}_{(1/3)-2x}TiO_3$ (LLTO, $0 < x < 0.16$), is representative material due to this high ionic conductivity at room temperature (10^{-3} Scm^{-1}) [1]. The crystal structure of LLTO is in Figure 1.6 [22]. The A site cations, which were Li^+ and La^{3+} in the cubic α -phase, were randomly distributed, while the A sites of the ordered β -LLTO had a doubled perovskite structure, with an alternating arrangement of La^+ rich and Li vacancy rich layers along the c axis [25]. Not only high ionic conductivity, the materials have many advantages such as stability in air and moisture, wide stability temperature window (to 1600K), good electrochemical stability ($>8V$). However, the materials have not been applied to commercial solid battery system because of its unsuitable for use with lithium and graphite negative electrodes [1, 4], high temperature sintering for synthesis, lower ionic conductivity than that of single crystal due to blocking grain boundaries [26, 27].

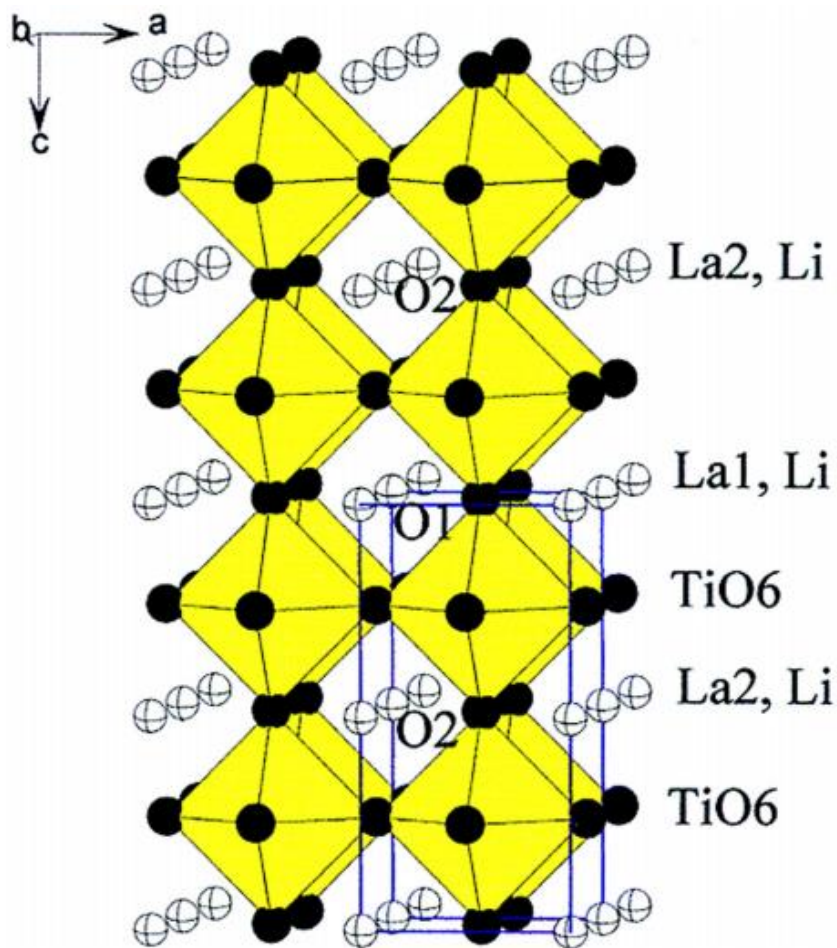


Figure 1.6 Structural schematic of perovskite (LLTO) [22].

1-2-3-3. Garnet

The garnets exhibit a general chemical formula of $A_3B_2(XO_4)_3$ (A = Ca, Mg, Y, La or rare earth; B = Al, Fe, Ga, Ge, Mn, Ni or X = Si, Ge, Al) where A, B and C are eight, six and four oxygen coordinated cation sites, which crystalize in a face centered cubic structure with the space group $Ia\bar{3}d$ (Figure 1.7) [28]. Because the garnet electrolytes high Li^+ concentration 5-7 Li atoms per formula unit and can accommodate excess Li^+ at octahedral sites than that of number of lithium at the tetrahedral sites [28], the ionic conductivity of the electrolytes can be controlled by increasing Li concentration. For example, $Li_5La_3M_2O_{12}$ has low ionic conductivity of 10^{-6} Scm^{-1} at room temperature. However, the low conductivity can be improved when La and M sites are substituted with cations of higher or lower oxidation state than La^{3+} and M^{5+} with controlling the content of substitution elements such as $Li_{6.6}La_3Zr_{1.6}Sb_{0.4}O_{12}$ ($7.7 \times 10^{-4} \text{ Scm}^{-1}$) and $Li_{6.2}La_3Zr_{1.2}Sb_{0.8}O_{12}$ ($4.5 \times 10^{-4} \text{ Scm}^{-1}$) [29, 30]. Also, the ionic conductivity of the garnet electrolytes can be improved by controlling shape control. For example, the particle shape of $Li_7La_3Zr_2O_{12}$ was changed by contents of substitution element (Ga), and can be more dense pellets with same pressure [31]. As the results, the interface resistance by grain boundary was reduced. Although garnet electrolytes have high lithium concentration and ionic conductivity, the materials could not be commercialized because of their unstable reactivity with cathode materials at the positive voltage window [32].

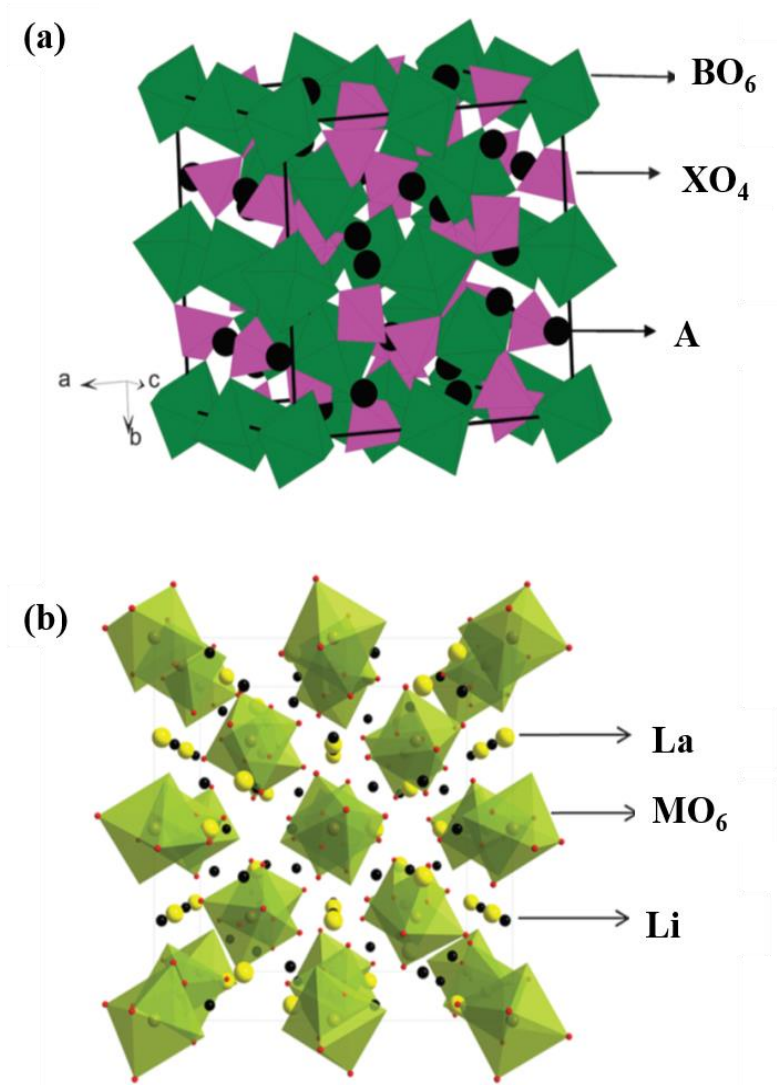


Figure 1.7 Structural schematic of (a) garnet and (b) garnet-related $\text{Li}_5\text{La}_3\text{M}_2\text{O}_{12}$. [28].

1-2-3-4. LISICON

The crystal structure of LISICON-like compounds is related to the γ - Li_3PO_4 structure with orthorhombic unit cell and $pnma$ space group, where all cations are tetrahedrally coordinated in Figure 1.8 [1, 33]. The oxide LISICON-like materials such as $\text{Li}_{14}\text{ZnGe}_4\text{O}_{16}$ showed low ionic conductivity ($\sim 10^{-7} \text{ Scm}^{-1}$) at room temperature by trapping of the mobile Li^+ ions by the immobile sublattice at lower temperatures via the formation of defect complexes [22]. Recently, the thio-LISICON changed O^{2-} to S^{2-} have been studied for high lithium ion conductivity by 3 orders of magnitude at room temperature [1]. Many thio materials such as $\text{Li}_{10}\text{MP}_2\text{S}_{12}$ (M=Si, Ge, and Sn), $\text{Li}_{11}\text{Si}_2\text{PS}_{12}$ showed high ionic conductivity [34-36]. Especially, $\text{Li}_{10}\text{GeP}_2\text{S}_{12}$ showed the highest lithium ion conductivity ($\sim 10^{-2} \text{ Scm}^{-1}$) at 27°C [34] among current ceramic electrolytes (Fig. 9) [1]. As the radius of S^{2-} is higher than O^{2-} , this substitution can significantly enlarge the size of Li^+ transport bottlenecks. Also, S^{2-} has better polarization capability than O^{2-} . Consequently, the interaction between skeleton and Li^+ ions is weaker and make the mobility of Li^+ [37]. The thio-LISICON materials also have favorable advantage, which is reduction of grain boundary resistance by simple cold-press of electrolytes powders because of its good ductility compare with hard oxide materials [22].

The thio-LISICON materials such as $\text{Li}_{3.25}\text{Ge}_{0.25}\text{P}_{0.75}\text{S}_4$ and $\text{Li}_{10}\text{GeP}_2\text{S}_{12}$ were known that the materials have theoretical wide electrochemical stability window from 0V to 4V versus Li/Li^+ [38]. However, many results have been explained that the sulfide materials have narrow electrochemical window and react with cathode and anode [22, 36, 39, 40]. Because of the larger size and smaller electronegativity of S^{2-} than O^{2-} , the

chemical interaction in the crystals structure of thio materials is week. The results of calculated equilibrium decomposition energies are listed in Table 1.1 [40]. As the results, the materials composed with S^{2-} anion have similar stability of less than 25meV per atom and show unstable characteristic than oxide materials. The results coincide with bandgaps calculation. O substituted LMPO materials have a larger bandgap than the LMPS materials [40]. Actually, almost thio materials react and are decomposed with cathode materials and anode materials including Li metal [40, 41]. In addition, the materials are difficult to synthesis at general atmosphere because they are very sensitive to air and moisture.

Table 1.1 Phase equilibria and decomposition energies for $\text{Li}_{10\pm 1}\text{MP}_2\text{X}_{12}$ [40]

Cation (M)	Anion (X)	Phase equilibria at $\text{Li}_{10\pm 1}\text{MP}_2\text{X}_{12}$ composition	E_{decomp} (meV per atom)
Si	O	$\text{Li}_4\text{SiO}_4 + 2\text{Li}_3\text{PO}_4$	92
Ge	O	$\text{Li}_4\text{GeO}_4 + 2\text{Li}_3\text{PO}_4$	96
Sn	O	$0.33\text{Li}_8\text{SnO}_6 + 0.67\text{Li}_2\text{SnO}_3 + 2\text{Li}_3\text{PO}_4$	97
Si	S	$\text{Li}_4\text{SiS}_4 + 2\text{Li}_3\text{PS}_4$	19
Ge	S	$\text{Li}_4\text{GeS}_4 + 2\text{Li}_3\text{PS}_4$	25
Sn	S	$\text{Li}_4\text{SnS}_4 + 2\text{Li}_3\text{PS}_4$	25

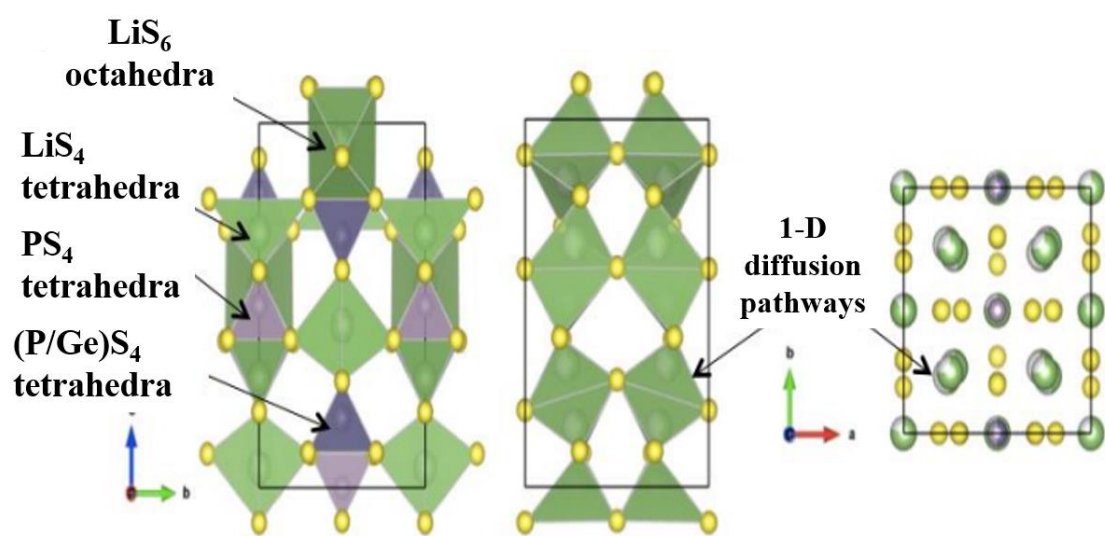


Figure 1.8 Structural schematic of LISICON like. [1].

1-2-4. Requirements for commercialized solid electrolyte in Li secondary batteries.

Although many super ionic conductors have been developed, the materials must be improved about somethings to be applied to all solid secondary batteries. First, the grain boundary inducing large interface resistance must be reduced. The resistance is major factor to make the electrolytes applied to commercial batteries and occur grain boundary resistance being reason of inaccurate measurement for ionic conductivity (Figure 1.9) [41]. Especially, the oxide electrolytes such as perovskite, NAISON, and garnet are difficult to contact with electrodes [41-43]. The brittle and toughness characteristics of the materials require high pressure and temperature to remove the grain boundary. The resistance can be reduced by controlling particle size and shape via substitution with an element and varies synthesis such as sol-gel route [42]. However, this method can not applied to large scale processing because of increasing electrolyte area requiring higher pressure. In order to formation of the interfaces with the large contact areas for better ionic conduction path, many studied have been reported such as using cathode materials coated with oxide electrolytes such as LiNbO_3 and $\text{Li}_4\text{Ti}_5\text{O}_{12}$, pulsed lager deposition (PLD) to prepare favorable interfaces between the electrodes and the solid electrolyte, and liquid-phase method [43].

Second, the side reaction between solid electrolyte and electrodes must be solved for the life of lithium secondary batteries. Unlike liquid organic electrolytes, the solid electrolytes are not decomposed by themselves but react with cathode or anode at working voltage and form the solid electrolyte interface (SEI) inducing another resistance. Unfortunately, the SEI usually unstable, then repeat formation and

decomposition during charge and discharge. Figure 1.10 shows calculated electrochemical stability ranges of various solid electrolyte materials grouped by anion, with corresponding binary for comparison [44]. As the results of the graph, materials with strongly bound polyanions such as the phosphates have much wider stability windows than sulfide materials. The results mean the tendency of increasing anodic stability with increasing electronegativity related with bond strength and explain that the sulfide electrolytes are unstable and may react with both cathode and anode.

In the results, thio-LISICON like materials such as $\text{Li}_{10}\text{GeP}_2\text{S}_{12}$ and Li_4SnS_4 exhibit high reaction energies with various cathode materials in comparison with phosphates materials. To protect the solid electrolytes from the side reaction, the sulfide electrolytes can be used with stable oxide coated cathode and anode materials. Respectively, LiAlO_2 and LiNbO_3 have been used as the protecting materials.

In summary, the ceramic electrolytes such as LGPS materials have been showed high ionic conductivity but must increase but also contact with electrode for reducing interface resistance and electrochemical stability with electrodes to applied to all solid battery system.

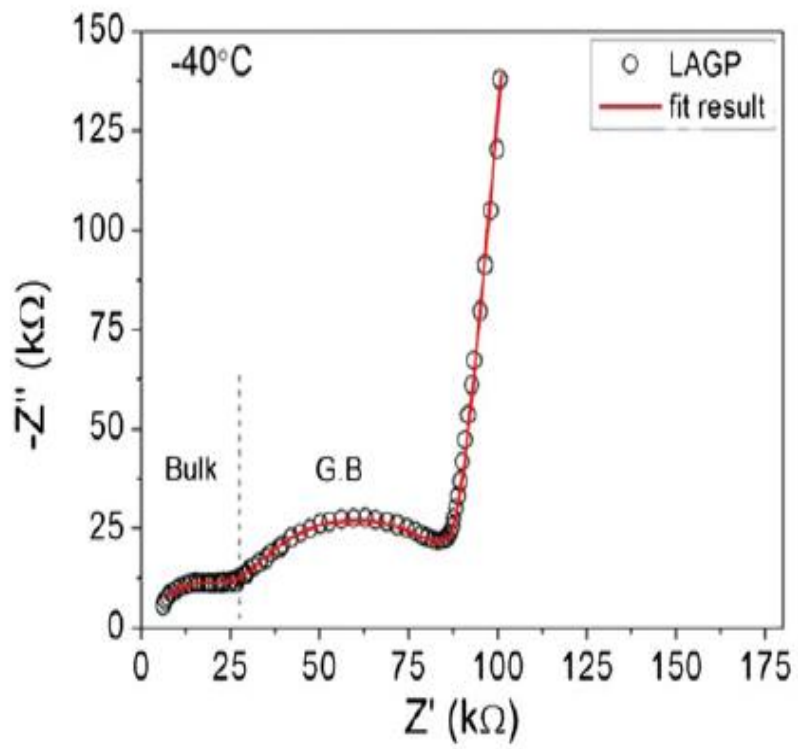


Figure 1.9 Nyquist plot of LAGP with fit result [41].

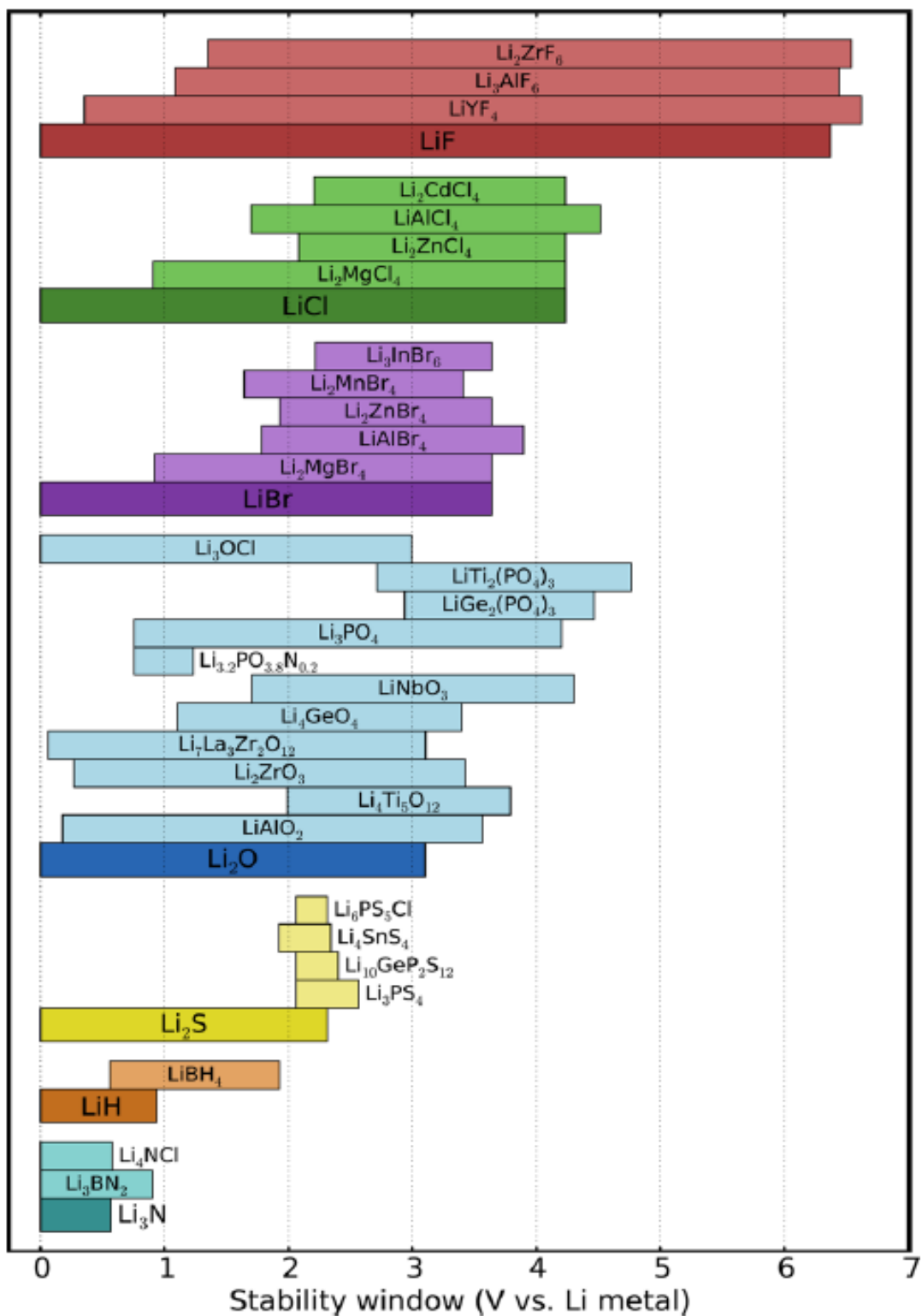


Figure 1.10 Calculated electrochemical stability window of solid electrolytes [44].

1-3. Lithium rich antiperovskite

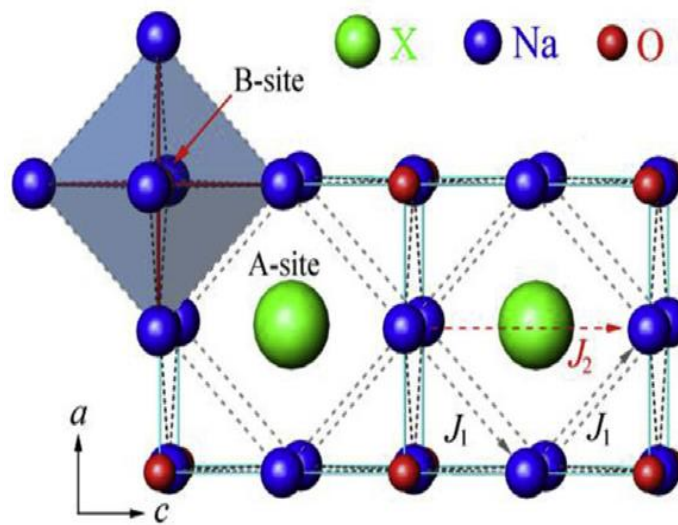
An antiperovskite material with the formula M_3AX (M, transitional metal; A, metal or semiconducting element and X, interstitial light element) have been developed and applied to a few fields. Various beneficial properties including magnetovolume effects [45], magnetostriction [46], magnetocaloric effects [47], magnetoresistance [48], and superconductivity [49, 50] have been obtained in antiperovskites. Recently, A_3BO type ($A = M^{+1}$ alkali metal, $B = X^{-1}$ anion, and oxygen) such as Na_3OX and Li_3OX materials have been received attention as the super ionic solid electrolytes [51]. This class of solid electrolytes exhibit Li conductivities on the order of 1 mScm^{-1} , which a maximum conductivity of 1.94 mScm^{-1} achieved for a solid solution mixture of Li_3OCl and Li_3OBr [51, 52]. Because of the simple cubic-like structure and benefit properties, the materials have been applied to various studies. Among the characteristics of the antiperovskites, the best of benefits is low melting temperature [52]. As the high dense pellet can be prepared and reduce the grain boundary using the low melting point, the materials are considered as the promising solid electrolyte. In this section, we introduce the antiperovskite materials for lithium super ionic conductors for lithium secondary batteries and explain our experimental purpose.

1-3-1. Introduction of lithium rich antiperovskite

1-3-1-1. Crystal structure and lithium diffusion mechanism

The Li_3OX antiperovskite materials were developed by replacing the electronegative anion element in the traditional perovskite system by the electropositive lithium metal,

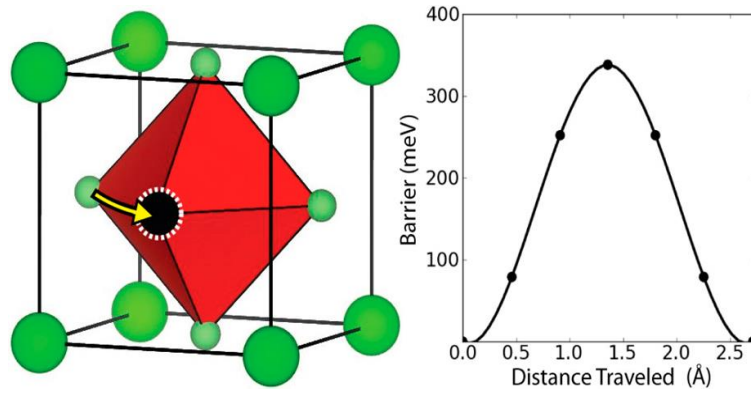
and continue the electronic inversion to $X^-O^{2-}Li^{+1}_3$, where monovalent anion (halogen), O^{2-} , and Li^+ . Figure 1.11 shows the crystal structure of antiperovskite Li_3OX ($X=Cl, Br$) with cubic symmetry and space group $pm3m$ [52]. OLi_6 octahedra share their corners with each other to form a three-dimensional framework (B-site) and the halogen anions occupy the 12-coordinated dodecahedral center A-site. Unlike usual solid electrolyte having substantial disorder and high vacancy concentration due to incomplete filling of particular crystallographic sites and thermodynamic effect [51, 52], the lithium rich antiperovskite materials consist of highly ordered Li sublattices. Therefore, Li migration is mediated by defects including Li vacancy (Schottky style) and interstitials (Frenkel style) [51]. Because the main migration is separated with two factors, the activation energy for Li^+ migration is also different by the migration mechanism. The results of the calculated energy are that the Li migration into a vacancy is 340 meV and the migration of an interstitial is 145 meV in Li_3OCl crystal. As the results, the Li migration in Li_3OX crystal prefer the Frenkel migration than Schottky style. Figure 1.12 [51] shows lithium migration illustration by Frenkel migration. When a Li atom from an octahedron moves to an interstitial site leaving behind vacancy, the excess Li prefers to form a dumbbell configuration with a Li of an octahedron. The center of the dumbbell resides at the octahedron corner of the displaced Li ion. The stable orientations of the Li dumbbell are parallel to the cubic axes of the perovskite crystal [51].



- Cubic type ($pm\bar{3}m$)
- B site \rightarrow Li_6O (Oxygen in O_h)
- A site \rightarrow halogen site (dodecahedral site)

Figure 1.11 Schematic illustration of structure for lithium rich antiperovskites [52].

1. Schottky migration: vacancy \rightarrow vacancy (Li ion pathway)



2. Frenkel migration: interstitial \rightarrow interstitial

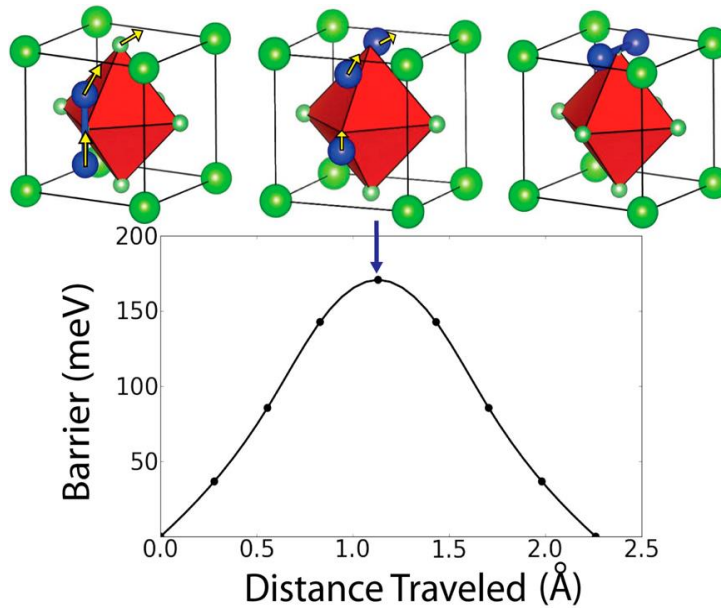


Figure 1.12 Schematic illustration of lithium diffusion mechanism in the structure of lithium rich antiperovskites [51].

1-3-1-2. Strategy for increasing lithium ion conductivity of antiperovskite

Because pseudocubic structure of antiperovskite has high crystallinity and low number of vacancy compare with other solid crystal, the materials have been usually synthesized by controlling cooling rate to produce incomplete crystal structure [51-53]. Unlike the manufacturing method, there are fundamental concepts by controlling antiperovskite crystal structures. The concepts are followed method [53].

- 1) Chemical substitution larger halogen anion X^- at the dodecahedral site via Frenkel style
- 2) Chemical substitution divalent M^{2+} instead of Li^+ (alkali earth metal such as Mg^{2+} and Ca^{2+}) at the Li_6O octahedral center via Schottky style
- 3) Synthesis using deplete LiA ($A = \text{halogen}$) to effectively introduce empty dodecahedral A-sites and Li vacancy at the octahedral
- 4) Complex the substitution anion X^- and divalent M^{2+}

Figure 1.13 [53] shows the crystal structures of the antiperovskite depending on the concept. In the case of concept 3), the Li_3OX structure is changed to $Li_{3-x}OX_{1-x}$ by deficient content of Li and halogen inducing change the charge balance, and local structure. As the results, the ionic conductivity of the distorted crystal is improved. The concept 2) is similar with concept 3). When the divalent M^{2+} element at the octahedral center in Li_3OX crystal is substituted, the structure is distorted to $Li_{3-x}M_{2/x}OX$ to fix different charge balance. The distorted structure has more vacancies at the Li site in the antiperovskite lattice and can accept more Li concentration. Because this concept increases the number of vacancy, which is main factor for Schottky migration, the

method is called to Schottky route.

In the case of concept 1), the antiperovskite materials have improved lithium conductivity by other routes. For example of Li_3OCl , alternate Cl and Br anions with diverse ionic radius in the dodecahedral A-sites within the three-dimensional lattice will provide much free space for the Li^+ ions to jump in and pass through, via Frenkel route [6]. When the large Br is substituted in Cl site, the repulsion between the anions such as halogen and oxygen is increased. As the results, the size of interstitial formed between the anions is also increase by increasing the number of Br. The large anion substitution also increases the cubic antiperovskite tolerance factor for Li_3OX [53, 54]:

$$t = (r_A - r_X) / (\sqrt{2}(r_B - r_X)) \quad (1.8)$$

where $r_A - r_X$ and $r_B - r_X$ are the equilibrium bond lengths. As the Br substitution, the tolerance factor increases. A higher tolerance factor indicates that the antiperovskite approaches a less distorted pseudocubic phase. The effect means stable phase and reduces the melting and phase transition temperatures in the antiperovskite.

Consequently, the structures of dense cubic Li_3OX can be changed by Frenkel and Schottky route to improve lithium conductivity of the anti-pervoskites. In the case of Schottky route, the method increases the ionic conductivity by form additional the number of vacancies and is separated to substitution M^+ ions and synthesis by using lack of Li and halogen content. Frenkel route by substitution larger anion at halogen site is applied to improved ionic conductivity by increasing size of interstitial.

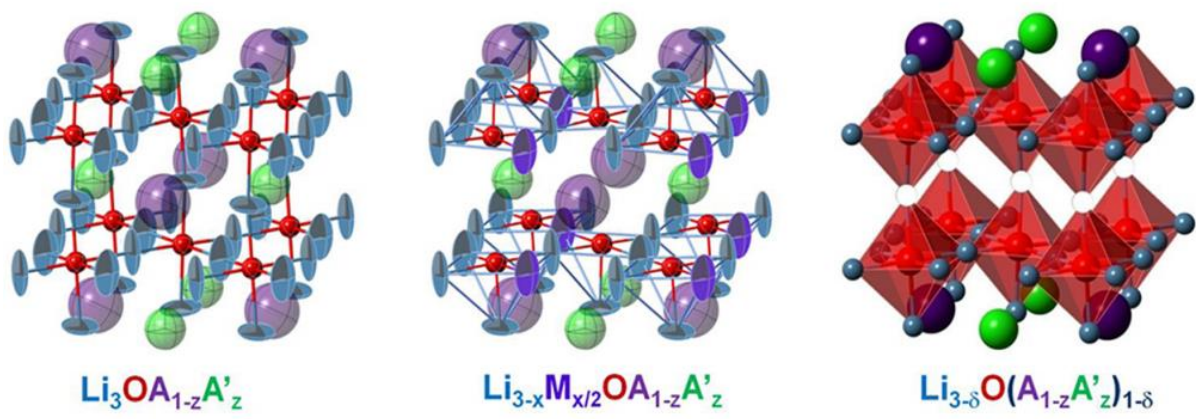


Figure 1.13 Schematic illustration of structural model about doped Li_3OX materials [53].

1-3-2. Anodic stability of lithium rich antiperovskites

One of the main physical properties for lithium rich antiperovskites is stable anodic stability [55]. Compare with sulfide materials, the theoretical voltage window of the antiperovskites is in at stable anodic voltages from 0V to 3V versus Li/Li⁺. The theoretical calculation explains that the antiperovskite materials are almost not reacts with an anode such as graphite, Li₄Ti₅O₁₂, and Li metal. Figure 1.14 exhibits example data of DC-cycling of Li₃OCl (direct current-cycling) [56]. DC-cycling is measurement for investigation of correct electrochemical stability versus Li metal. The measurement is conducted as contacting between Li and solid electrolyte using a symmetric cell of Li/electrolyte/Li by applying a constant direct-current (DC) with periodically changed polarity [56, 57]. Compare with unstable LGPS, Li₃OCl showed stable voltage profile. Except for initial cycling, the voltage changes, which means reactivity with Li almost not occurs during the cycling. This means that the electrolyte has good electrochemical stability. In the case of voltage change during initial cycle, Li₃OCl react with Li metal and form stable SEI via self-stabilizing feature such as Al₂O₃ formation on Al aluminum to protect the metals from oxidation. Because of this physical characteristic, lithium rich antiperovskites can be promising candidates for lithium metal batteries.

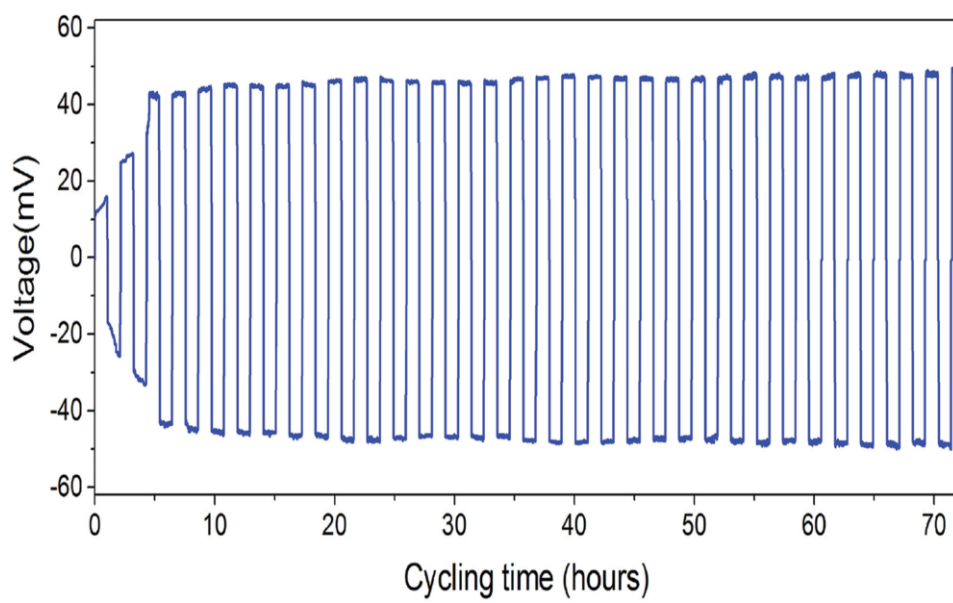


Figure 1.14 Example DC-cycling data of Li_3OCl [56].

1-3-3. Grain boundary control by melting method from antiperovskite materials

The second main characteristic of antiperovskites is low melting temperature. The melting point of the materials is listed in Table 1.2. Almost lithium rich antiperovskites show low melting point 280°C. The melting temperature is changed when the phase transition occurs by substitution such as $\text{Li}_3\text{OCl}_{0.5}\text{Br}_{0.5}$. Figure 1.15. (a) shows the differential scanning calorimetry (DSC) data of Li_3OCl and $\text{Li}_3\text{OCl}_{0.5}\text{Br}_{0.5}$ by Los Alamos group [53, 58, 59]. The melting point of Li_3OCl are 280°C while the point of $\text{Li}_3\text{OCl}_{0.5}\text{Br}_{0.5}$ is 270°C. When the larger Br ion is substituted on dodecahedral center A-site instead of Cl, the phase of Li_3OCl is changed to less distorted cubic structure and finally, the melting point decrease. The melting points are lower than other oxide materials such as perovskite and thio-LISICON materials. The low melting point are applied to reducing grain boundary like Figure 1.15. (b). Antiperovskite materials are well good at contact with the powder of active materials after the electrolytes are melt at low melting point and transfer to high viscosity ceramic liquid. Using this property, the dense electrolyte pellet can also be produced. There are several methods to make dense pellet such as pouring the molten antiperovskite on a flat plate to form a pancake sample [60, 61] and making the pellet after calcination for precursor mixed pellet. The reduced grain boundary by the dens pellet shows high ionic conductivity such as Li_3OCl and Li_3OBr (10^{-3} Scm^{-1}) [58, 59]. The solid membrane reducing grain boundary can also make the accurate comparison with both ionic conductivity and other electrochemical measurements. Therefore, the comfortable and simple melting method for antiperovskite need to applied to super ionic electrolyte.

Table 1.2 Ionic conductivity and chemical properties of lithium rich antiperovskites.

	Li₃OX	Li₃OX_{1-a}X_a	Li_{3-x}M_{x/2}X
Structure	Cubic	Cubic like	Cubic like
Ionic conductivity (S _{cm} ⁻¹)	10 ⁻⁷ -10 ⁻⁴	-10 ⁻³	-10 ⁻³
Thermal stability (°C)		-270	
Melting point (°C)		280	

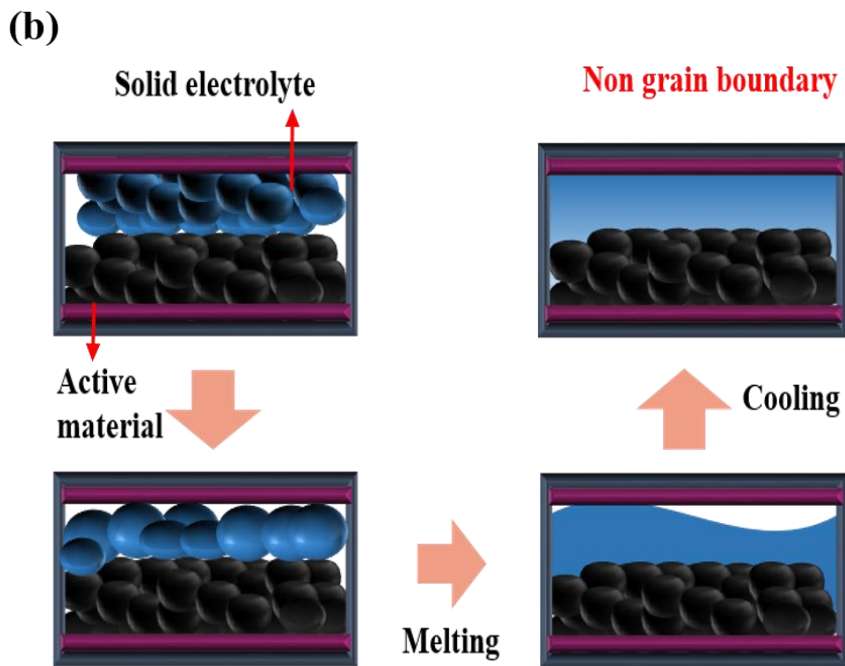
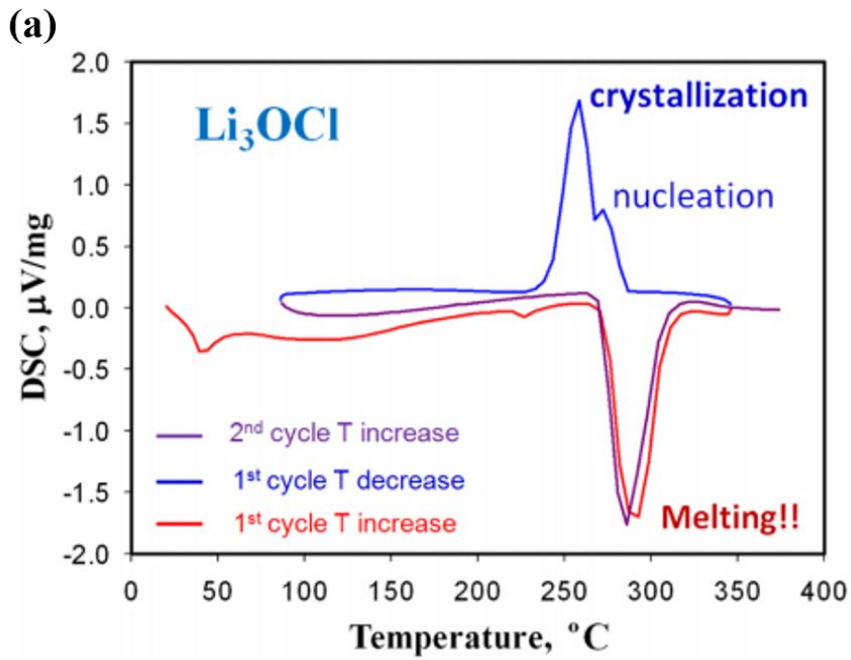


Figure 1.15 (a) Example DSC data of Li_3OCl [53] and (b) schematic illustration of melting method of antiperovskites.

1-3-4. Pseudo antiperovskite materials for simple synthesized solid electrolytes

Although many advantages of antiperovskites, the materials have also obstacles to applied to commercial secondary batterie such as moisture sensitive like thio-LISICION materials. The most thing among the problems is that the lithium rich antiperovskites difficult synthesis. For example, Li_3OX types are synthesized by using simple solid-state synthesis as followed equation.



The chemical reaction can be simple by using two precursor Li_2OH and Li_2O . Unfortunely, the Li_3OX materials do not predicted to be thermodynamically stable at low temperature. As the results of calculated phase diagram [51], Li_3OX phase will decompose into a two-phase mixture LiOH or Li_2O and LiX . The theoretical calculation of energy difference between the Li_3OCl and the starting materials is in Figure 1.16 [53]. The energy difference is quite small, and the formation energy of Li_3OCl is 5.01 KJ/mol, which is higher than that of the $\text{Li}_2\text{O} + \text{LiCl}$. These results are coincide with the synthesis requirements, which the synthesis need high pressure, high temperature, and long calcination time [54].

The synthesis condition of lithium rich antiperovskites is listed in Table 1.3. As the table, the Li_3OX types are known the difficult products. In the case of the synthesis of Li_3OX using LiOH , it requires very long calcination time (48-72h) to remove H_2O . Even though, the products are difficult to synthesis at one go. For example, the melting temperature of Li_3OX (280-320°C) is lower than those of precursors such as Li_2O

(1400°C) and LiCl (605°C), the formed products were melted and coated the surfaces of the particles of starting materials. As the results, a diffusion-limited condition is met as the Li₃OX product prevents reaction between Li₂O and LiX [60]. In order to completing products, the procedure including high energy ball-mill and calcination should be repeated 2-3 times.

Recently, Li₂OHX types materials (X=Cl and Br) called pseudo antiperovskite have been studied to supplement the Li₃OX materials. The Li₂OHX materials are composed with lithium, halogen, and hydroxide ion OH as the replacing one Li to one H. The pseudo antiperovskites have many advantages such as wide electrochemical stability (0-9V versus Li⁺/Li) [60], low melting temperature (300°C) [62]. Comparison with Li₃OX types, the best advantage of Li₂OHX is easy and simple synthesis. The products are usually produced by solid-state synthesis as followed the equation.



The synthesis for Li₂OHX is required only one grinding or ball-mill and calcination with low temperature (300-350°C) and short time (0.5h-4h). Because the Li₂OHX materials is stable at room temperature unlike Li₃OX type, the materials are easy to handling and synthesis. Also, the pseudo antiperovskites have the self-stabilizing characteristic similar to Li₃OX. Figure 1.17 [60] shows the results of cross-section SEM images and DC-cycling of Li₂OHCl/SEI/Li. As the results, the electrochemical stability versus Li is stable and the materials form stable SEI during cycling.

Although many good properties of Li₂OHX types, the materials show low ionic conductivity at room temperature. There are two factors about the ionic conductivity

compare with Li_3OX . First, the determined crystal structure of Li_2OHX by neutron diffraction is closer to orthorhombic than cubic phase [61]. The complicate phase may compose the complicate Li^+ diffusion tunnel. Second, when the Li^+ migrate to neighbor interstitial, the H^+ located Li^+ tunnel by fixed O-H-X hydrogen bond hinder the lithium diffusion by the coulombic repulsion and steric hindrance [61]. To improve the low lithium conductivity, John B. Goodenough *et al.* studied $\text{Li}_2(\text{OH})_{0.9}\text{F}_{0.1}$ [61]. The substitution of F on OH site not only decreases the concentration of H^+ ions, but also stabilized the more favorable cubic phase from orthorhombic phase. As the F substitution, the Li_2OHX type material exhibited that ionic conductivity improved.

Table 1.3 Synthesis conditions of lithium rich antiperovskites.

Product	Precursor	Reaction mechanism	Method	Condition	
				Temperature (°C)	Time (hr)
Li ₃ OX	LiOH	2LiOH+LiX → Li ₃ OX +H ₂ O		350	48-72
	LiX				
Li ₃ OX	Li ₂ O	Li ₂ O+LiX → Li ₃ OX	Solid state synthesis	450	12-16
	LiX				
Li ₂ OHX	LiOH	LiOH+LiX → Li ₂ OHX		350	0.5-1
	LiX				

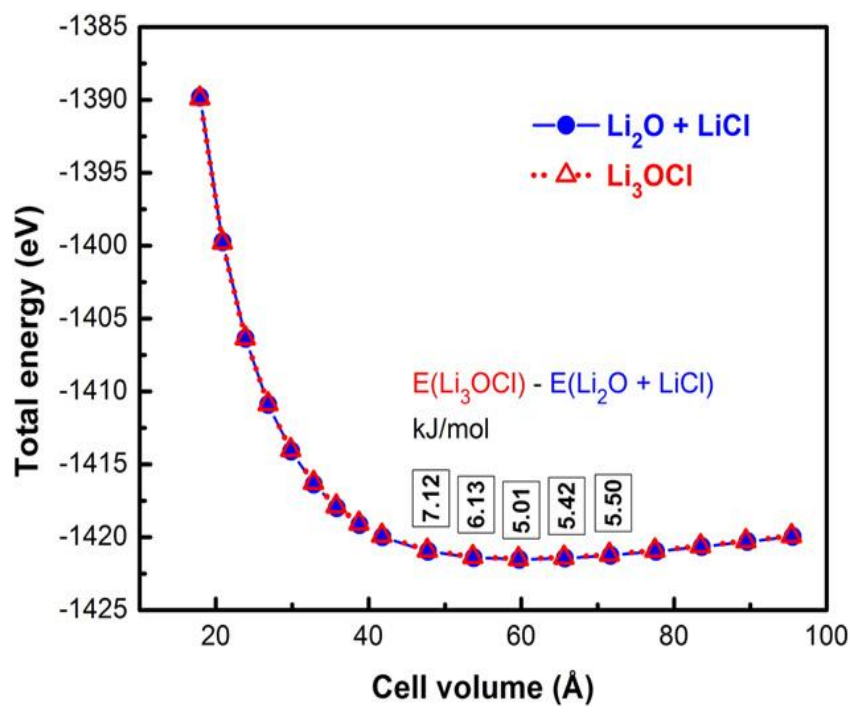


Figure 1.16 Energy difference between Li_3OCl and the starting materials ($\text{Li}_2\text{O} + \text{LiCl}$) as a function of cell volume [53].

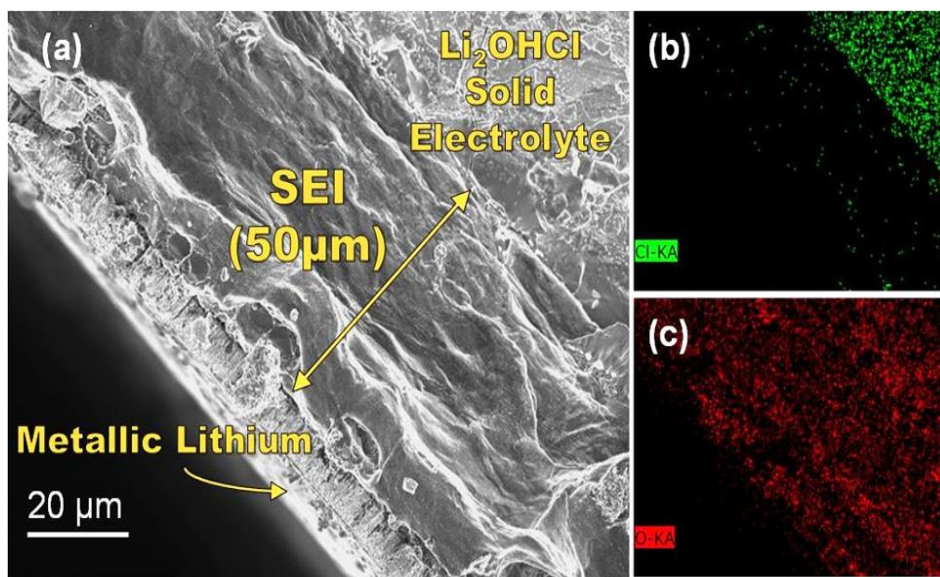


Figure 1.17 SEM images of Li/Li₂OHCl/Li cell after 160 charge/discharge cycles [60].

1.4 Purpose

Based on above previous studies, we investigated the possibility of Li_2OHCl , which is easy to synthesis as a solid electrolyte. In particular, to overcome the low ionic conductivity of the Li_2OHCl , we studied both phase transition of the Li_2OHCl by the halogen anion substitution such as the F substitution for OH site that was done in the previous research [61] and ionic conductivity increase mechanism by the size effects of the substituted species and substituted site (OH and Cl site). In addition, the mechanism of chemical and electrochemical stability enhancement of Li_2OHCl materials by substitution species and sites have analyzed.

Prior to experiments to improve ionic conductivity and electrochemical stability, the basic studies for physical properties and electrochemical experiments including synthesis of Li_2OHCl materials and the experiments for precise characterization such as XRD and FT-IR were preceded due to its high sensitivity from moisture. After the basic experiment, the substituted Li_2OHCl materials have been studied for increasing ionic conductivity and electrochemical stability. As the substitution species, fluorine and bromine, which is smaller and larger ionic size than chloride in Li_2OHCl , were choose. Each substitution species was substituted for Cl and OH in Li_2OHCl and produced $\text{Li}_2(\text{OH})_{0.9}\text{Cl}$ and $\text{Li}_2\text{OHCl}_{0.8}\text{X}_{0.2}$ ($\text{X}=\text{F}, \text{Br}$).

References

- [1] Bachman, J. C. *et al.* Inorganic solid-state electrolytes for lithium batteries: mechanisms and properties governing ion conduction. *Chemical reviews* **116**, 140-162 (2015).
- [2] Minh, N. Q. Ceramic fuel cells. *Journal of the American Ceramic Society* **76**, 563-588 (1993).
- [3] Tarascon, J.-M. & Armand, M. Issues and challenges facing rechargeable lithium batteries. *Nature* **414**, 359-367 (2001).
- [4] Stephan, A. M. & Nahm, K. Review on composite polymer electrolytes for lithium batteries. *Polymer* **47**, 5952-5964 (2006).
- [5] Niitani, T., Shimada, M., Kawamura, K. & Kanamura, K. Characteristics of new-type solid polymer electrolyte controlling nano-structure. *Journal of power sources* **146**, 386-390 (2005).
- [6] Song, J., Wang, Y. & Wan, C. C. Review of gel-type polymer electrolytes for lithium-ion batteries. *Journal of Power Sources* **77**, 183-197 (1999).
- [7] Bates, J. *et al.* Fabrication and characterization of amorphous lithium electrolyte thin films and rechargeable thin-film batteries. *Journal of power sources* **43**, 103-110 (1993).
- [8] Goodenough, J. B. & Kim, Y. Challenges for rechargeable Li batteries. *Chemistry of materials* **22**, 587-603 (2009).
- [9] Dyer, C. K., Moseley, P. T., Ogumi, Z., Rand, D. A. & Scrosati, B. *Encyclopedia of electrochemical power sources*. (Elsevier Science & Technology, 2009).
- [10] Jung, Y. C. *et al.* Ceramic separators based on Li⁺ conducting inorganic electrolyte for high-performance lithium-ion batteries with enhanced safety. *Journal of Power Sources* **293**, 675-683 (2015).
- [11] Garche, J. *et al.* *Encyclopedia of electrochemical power sources*. (Newnes, 2013).
- [12] Xu, K. Nonaqueous liquid electrolytes for lithium-based rechargeable batteries. *Chemical reviews* **104**, 4303-4418 (2004).
- [13] Martínez-Juárez, A., Pecharrromán, C., Iglesias, J. E. & Rojo, J. M. Relationship between Activation Energy and Bottleneck Size for Li⁺ Ion Conduction in NASICON Materials of Composition LiMM'(PO₄)₃; M, M' = Ge, Ti, Sn, Hf. *The*

- Journal of Physical Chemistry B* **102**, 372-375 (1998).
- [14] Rodger, A., Kuwano, J. & West, A. Li⁺ ion conducting γ solid solutions in the systems Li₄XO₄-Li₃YO₄: X= Si, Ge, Ti; Y= P, As, V; Li₄XO₄-LiZO₂: Z= Al, Ga, Cr and Li₄GeO₄-Li₂CaGeO₄. *Solid State Ionics* **15**, 185-198 (1985).
- [15] Buck, R. P. Transport properties of ionic conductors. *Sensors and Actuators* **1**, 137-196 (1981).
- [16] Goodenough, J. B. Oxide-ion electrolytes. *Annual review of materials research* **33**, 91-128 (2003).
- [17] Tärneberg, R. & Lund, A. Ion diffusion in the high-temperature phases Li₂SO₄, LiNaSO₄, LiAgSO₄ and Li₄Zn(SO₄)₃. *Solid State Ionics* **90**, 209-220 (1996).
- [18] Kummer, J. β -alumina electrolytes. *Progress in Solid State Chemistry* **7**, 141-175 (1972).
- [19] Aono, H., Sugimoto, E., Sadaoka, Y., Imanaka, N. & Adachi, G. y. The Electrical Properties of Ceramic Electrolytes for LiM_xTi_{2-x}(PO₄)_{3+y}Li₂O, M= Ge, Sn, Hf, and Zr Systems. *Journal of the Electrochemical Society* **140**, 1827-1833 (1993).
- [20] Ortiz, G. F., López, M. C., Lavela, P., Vidal-Abarca, C. & Tirado, J. L. Improved lithium-ion transport in NASICON-type lithium titanium phosphate by calcium and iron doping. *Solid State Ionics* **262**, 573-577 (2014).
- [21] Norhaniza, R., Subban, R. & Mohamed, N. Cr and V substituted LiSn₂P₃O₁₂ solid electrolyte materials. *Journal of Power Sources* **244**, 300-305 (2013).
- [22] Cao, C., Li, Z.-B., Wang, X.-L., Zhao, X.-B. & Han, W.-Q. Recent advances in inorganic solid electrolytes for lithium batteries. *Frontiers in Energy Research* **2**, 25 (2014).
- [23] Hartmann, P. *et al.* Degradation of NASICON-type materials in contact with lithium metal: Formation of mixed conducting interphases (MCI) on solid electrolytes. *The Journal of Physical Chemistry C* **117**, 21064-21074 (2013).
- [24] Knauth, P. Inorganic solid Li ion conductors: An overview. *Solid State Ionics* **180**, 911-916 (2009).
- [25] Hartmann, P. *et al.* Degradation of NASICON-type materials in contact with lithium metal: Formation of mixed conducting interphases (MCI) on solid electrolytes. *The Journal of Physical Chemistry C* **117**, 21064-21074 (2013).
- [26] Knauth, P. Inorganic solid Li ion conductors: An overview. *Solid State Ionics* **180**, 911-916 (2009).

- [27] Wenzel, S., Leichtweiss, T., Krüger, D., Sann, J. & Janek, J. Interphase formation on lithium solid electrolytes—an in situ approach to study interfacial reactions by photoelectron spectroscopy. *Solid State Ionics* **278**, 98-105 (2015).
- [28] Thangadurai, V., Narayanan, S. & Pinzaru, D. Garnet-type solid-state fast Li ion conductors for Li batteries: critical review. *Chemical Society Reviews* **43**, 4714-4727 (2014).
- [29] Cussen, E. J. Structure and ionic conductivity in lithium garnets. *Journal of Materials Chemistry* **20**, 5167-5173 (2010).
- [30] Ramakumar, S., Satyanarayana, L., Manorama, S. V. & Murugan, R. Structure and Li⁺ dynamics of Sb-doped Li₇La₃Zr₂O₁₂ fast lithium ion conductors. *Physical Chemistry Chemical Physics* **15**, 11327-11338 (2013).
- [31] El Shinawi, H. & Janek, J. Stabilization of cubic lithium-stuffed garnets of the type “Li₇La₃Zr₂O₁₂” by addition of gallium. *Journal of Power Sources* **225**, 13-19 (2013).
- [32] Kim, K. H. *et al.* Characterization of the interface between LiCoO₂ and Li₇La₃Zr₂O₁₂ in an all-solid-state rechargeable lithium battery. *Journal of Power Sources* **196**, 764-767 (2011).
- [33] West, A. Crystal chemistry of some tetrahedral oxides. *Zeitschrift für Kristallographie-Crystalline Materials* **141**, 422-436 (1975).
- [34] Bron, P. *et al.* Li₁₀SnP₂S₁₂: an affordable lithium superionic conductor. *Journal of the American Chemical Society* **135**, 15694-15697 (2013).
- [35] Kamaya, N. *et al.* A lithium superionic conductor. *Nature materials* **10**, 682 (2011).
- [36] Kuhn, A. *et al.* A new ultrafast superionic Li-conductor: ion dynamics in Li₁₁Si₂PS₁₂ and comparison with other tetragonal LGPS-type electrolytes. *Physical Chemistry Chemical Physics* **16**, 14669-14674 (2014).
- [37] Murayama, M. *et al.* Synthesis of new lithium ionic conductor thio-LISICON—lithium silicon sulfides system. *Journal of Solid State Chemistry* **168**, 140-148 (2002).
- [38] Kanno, R. & Murayama, M. Lithium Ionic Conductor Thio-LISICON: The Li₂S GeS₂P₂S₅ System. *Journal of The Electrochemical Society* **148**, A742-A746 (2001).
- [39] Rao, R. P. & Adams, S. Studies of lithium argyrodite solid electrolytes for all solid state batteries. *physica status solidi (a)* **208**, 1804-1807 (2011)
- [40] Mo, Y., Ong, S. P. & Ceder, G. First principles study of the Li₁₀GeP₂S₁₂ lithium

- super ionic conductor material. *Chemistry of Materials* **24**, 15-17 (2011).
- [41] Chung, H. & Kang, B. Increase in grain boundary ionic conductivity of $\text{Li}_{1.5}\text{Al}_{0.5}\text{Ge}_{1.5}(\text{PO}_4)_3$ by adding excess lithium. *Solid State Ionics* **263**, 125-130 (2014).
- [42] Bauerle, J. Study of solid electrolyte polarization by a complex admittance method. *Journal of Physics and Chemistry of Solids* **30**, 2657-2670 (1969).
- [43] Yubuchi, S. *et al.* Preparation of high lithium-ion conducting $\text{Li}_6\text{PS}_5\text{Cl}$ solid electrolyte from ethanol solution for all-solid-state lithium batteries. *Journal of Power Sources* **293**, 941-945 (2015).
- [44] Richards, W. D., Miara, L. J., Wang, Y., Kim, J. C. & Ceder, G. Interface stability in solid-state batteries. *Chemistry of Materials* **28**, 266-273 (2015).
- [45] Chi, E., Kim, W. & Hur, N. Nearly zero temperature coefficient of resistivity in antiperovskite compound CuNMn_3 . *Solid State Communications* **120**, 307-310 (2001).
- [46] Asano, K., Koyama, K. & Takenaka, K. Magnetostriction in Mn_3CuN . *Applied Physics Letters* **92**, 161909 (2008).
- [47] Tohei, T., Wada, H. & Kanomata, T. Negative magnetocaloric effect at the antiferromagnetic to ferromagnetic transition of Mn_3GaC . *Journal of Applied Physics* **94**, 1800-1802 (2003).
- [48] Kamishima, K. *et al.* Giant magnetoresistance in the intermetallic compound Mn_3GaC . *Physical Review B* **63**, 024426 (2000).
- [49] He, T. *et al.* HMA, MK Haas, JS Slusky, K. Inumara, et al. *Nature* **411**, 54 (2001).
- [50] Uehara, M., Uehara, A., Kozawa, K. & Kamishima, Y. New antiperovskite-type superconductor ZnNyNi_3 . *Journal of the Physical Society of Japan* **78**, 033702-033702 (2009).
- [51] Emly, A., Kioupakis, E. & Van der Ven, A. Phase stability and transport mechanisms in antiperovskite Li_3OCl and Li_3OBr superionic conductors. *Chemistry of Materials* **25**, 4663-4670 (2013).
- [52] Lu, Z. *et al.* Defect chemistry and lithium transport in Li_3OCl antiperovskite superionic conductors. *Physical Chemistry Chemical Physics* **17**, 32547-32555 (2015).
- [53] Zhao, Y. & Daemen, L. L. Superionic conductivity in lithium-rich antiperovskites.

- Journal of the American Chemical Society* **134**, 15042-15047 (2012).
- [54] Zhang, J. *et al.* High pressure-high temperature synthesis of lithium-rich $\text{Li}_3\text{O}(\text{Cl}, \text{Br})$ and $\text{Li}_{3-x}\text{Ca}_{x/2}\text{OCl}$ antiperovskite halides. *Inorganic Chemistry Communications* **48**, 140-143 (2014).
- [55] Li, S. *et al.* Reaction mechanism studies towards effective fabrication of lithium-rich antiperovskites Li_3OX ($\text{X} = \text{Cl}, \text{Br}$). *Solid State Ionics* **284**, 14-19 (2016).
- [56] Lü, X. *et al.* Antiperovskite Li_3OCl Superionic Conductor Films for Solid State Li Ion Batteries. *Advanced Science* **3** (2016).
- [57] Lü, X. *et al.* Li-rich antiperovskite Li_3OCl films with enhanced ionic conductivity. *Chemical Communications* **50**, 11520-11522 (2014).
- [58] Wang, Y. *et al.* Structural manipulation approaches towards enhanced sodium ionic conductivity in Na-rich antiperovskites. *Journal of Power Sources* **293**, 735-740 (2015).
- [59] Zhu, J. *et al.* Enhanced ionic conductivity with $\text{Li}_7\text{O}_2\text{Br}_3$ phase in Li_3OBr antiperovskite solid electrolyte. *Applied Physics Letters* **109**, 101904 (2016).
- [60] Hood, Z. D., Wang, H., Samuthira Pandian, A., Keum, J. K. & Liang, C. Li_2OHCl crystalline electrolyte for stable metallic lithium anodes. *Journal of the American Chemical Society* **138**, 1768-1771 (2016).
- [61] Li, Y. *et al.* Fluorine Doped Antiperovskite Electrolyte for All Solid State Lithium Ion Batteries. *Angewandte Chemie International Edition* **55**, 9965-9968 (2016).

Chapter 2. General experimental

2-1. Physical characterization

2-1-1. X-ray diffraction (XRD)

XRD is powerful technique that uses the diffraction of X-rays on powder or microcrystalline samples for the study of crystal structures and those of volume. It is based on constructive interference of monochromatic X-ray and a crystalline sample. The inorganic powders were usually used as the sample for the diffraction analysis. The samples were interacted with the incident X-ray beam as followed Bragg's Law equation (Figure 2.1).

$$n\lambda = 2d_{hkl}\sin\theta_{hkl} \quad (\text{Bragg equation}) \quad (n=1, 2, 3 \dots) \quad (2.1)$$

where λ is frequency of incident beam, d is d-spacing, θ is the diffraction angles when the samples interact with incident beam, hkl is miller index. This law related the wavelength of electromagnetic radiation to the diffraction angle and the lattice spacing in a crystalline powder. The difference of path length between reflections on neighboring planes is $d_{hkl}\sin\theta_{hkl}$. For example, the smaller the distance d-spacing, the larger the diffraction angle θ . When the wavelength λ increase, the diffraction angle θ increase. Because the difference of path length means the different interference between the diffraction wavelength, the angle is main scale for determining the crystals. From the equations, the d-spacing can be calculated by considering Miller indices and unit

cell parameter it was related 7 types of crystal system. Figure 2.2 is the table of the crystal system and d-spacing [1-3]. The crystals depend on three cell parameters (a, b, c) and three angles (α , β , γ). The crystals are different symmetries from the cubic crystal composed with three same parameter values and three 90 degrees angles to triclinic. According to the rotational symmetry, there are 14 different Bravais lattices in which similar points can be arranged in a three-dimensional space not 28 cases by French crystallographer August Bravais in 1848. The 14 Bravais lattices are combined with 32-point group symmetries and finally, give the 230 space groups. This powerful analysis can be applied to almost inorganic materials which have quite electronic density except for low periodic number such as Li due to its low electronic density.

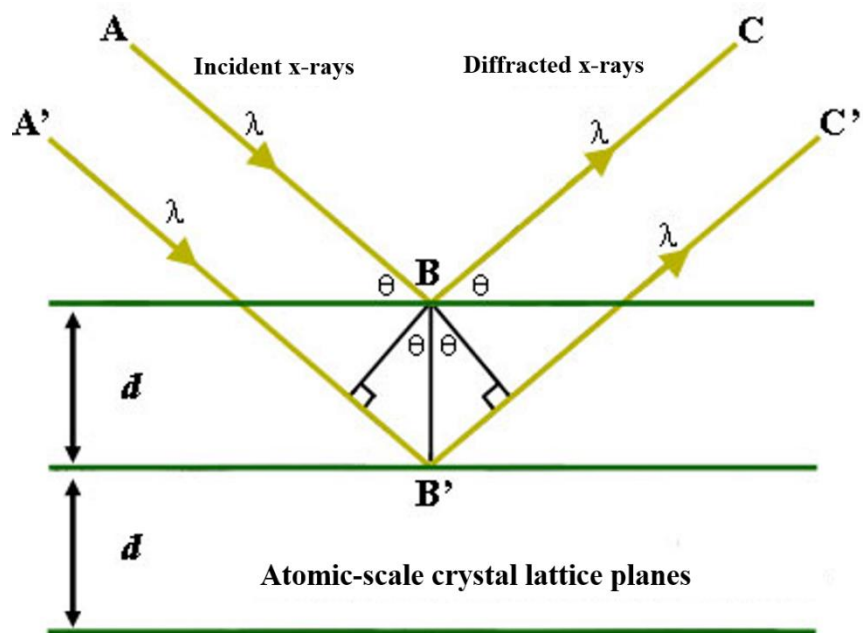


Figure 2.1 Bragg reflection on a set of atomic planes.

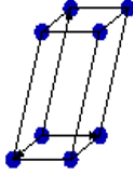
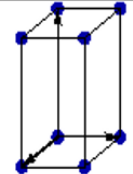
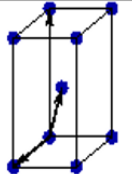
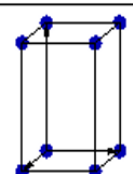
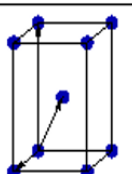
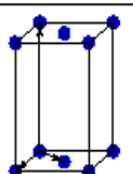
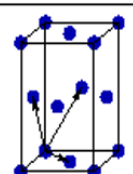
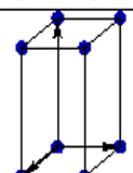
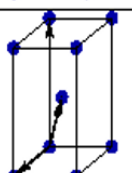
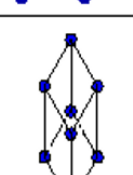
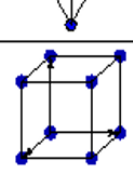
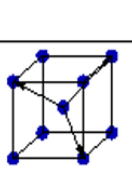
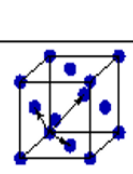
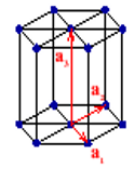
Bravais lattice	Parameters	Simple (P)	Volume centered (I)	Base centered (C)	Face centered (F)
Triclinic	$a_1 \neq a_2 \neq a_3$ $\alpha_{12} \neq \alpha_{23} \neq \alpha_{31}$				
Monoclinic	$a_1 \neq a_2 \neq a_3$ $\alpha_{23} = \alpha_{31} = 90^\circ$ $\alpha_{12} \neq 90^\circ$				
Orthorhombic	$a_1 \neq a_2 \neq a_3$ $\alpha_{12} = \alpha_{23} = \alpha_{31} = 90^\circ$				
Tetragonal	$a_1 = a_2 \neq a_3$ $\alpha_{12} = \alpha_{23} = \alpha_{31} = 90^\circ$				
Trigonal	$a_1 = a_2 = a_3$ $\alpha_{12} = \alpha_{23} = \alpha_{31} < 120^\circ$				
Cubic	$a_1 = a_2 = a_3$ $\alpha_{12} = \alpha_{23} = \alpha_{31} = 90^\circ$				
Hexagonal	$a_1 = a_2 \neq a_3$ $\alpha_{12} = 120^\circ$ $\alpha_{23} = \alpha_{31} = 90^\circ$				

Figure 2.2 Table of seven crystal system and 14 Bravais lattice [1-3].

2-1-2. Fourier transform-infrared spectroscopy (FT-IR)

FT-IR is a technique, which is used to analysis an infrared spectrum of absorption or emission of a solid, liquid, and gas state samples. When the IR radiation is passed through a sample, the sample absorb the radiation having specific energy. The resulting spectrum represents the molecular absorption and transmission, creating a molecular fingerprint of the sample [4]. This spectrum is related with the three vibrations motion (stretching and bending) between the bonds such as covalency in a material. Because of different vibration energy of the bonds and the materials, FT-IR analysis is useful to qualitative analysis of organic materials including polymers. In the case of inorganic materials, the detection of the bonds such as metal-metal is impossible due to the energy of bonds in different energy region from the infrared energy. However, the metal-oxide bonds can be searched by using the FT-IR. Therefore, the analysis is good at characterization of metal-oxide bonds.

2-1-3. Filed emission scanning electron microscopy (FE-SEM)

FE-SEM is Field Emission Scanning Electron Microscope which operates with a high-energy electron beam in a scan pattern instead of light source. These electrons are released by a field emission source in a field emission gun. These electron emitters can produce up to 1000x the emission of a tungsten filament with high vacuum atmosphere to prevent unnecessary interaction between gas molecular and the electron beam. After the electrons beam exit the electron gun, monochromatic beam using metal apertures and magnetic lenses. And Finally, the detectors of each type of electrons are placed in

the microscopes that collect signals to produce an image of the patterns [5]. The electrons from the primary beam spread out in the sample to form the interaction volume. The size of the interaction volume depends on the accelerating voltage value of the primary electron beam and atomic number of the sample. The interaction volume increase with a larger accelerating voltage, but smaller for samples with a higher atomic number. Secondary electrons are produced from the surface of the sample or topmost part of the interaction volume and X-rays are generated within the whole of the interaction volume [6, 7]. FE-SEM is used to visualized information of local area on the surface of chemicals. Also, the analysis can be combined with Energy dispersive X-ray spectroscopy (EDS) for good elemental analysis such as elemental composition near the surface of the samples with atomic number (Z) >3 . The combination can also visualize the element distribution in a sample by mapping which showing the concentration of one element over a selected area of images of sample.

2-1-4. Thermogravimetric analysis (TGA) and differential scanning calorimeter (DSC)

TGA analysis is representative thermal analysis for measurement of physical and chemical properties of materials as a function of temperature or as a function of time with mass loss of materials. The analysis is conducted by increasing temperature from the room temperature to high temperature (usually 600 or 900°C) with constant heating rate in normal air or N₂ atmosphere. As the one of the thermal analysis, TGA provide many information such as second-order phase transition, sublimation, absorption, desorption, and chemical stability. Specially, the chemical stability is main object of the

analysis by observing mass loss. From the information, the materials are analyzed about their reactivity and decomposition point. For example, the mass loss of a metal oxide material is observed when the material decomposed by O₂ vaporization from the material except for phase transition. Common application of TGA are materials characterization through analysis of characteristic decomposition of organic content in a sample, and determination of inorganic content in a sample, which may be useful for corroborating predicted material structures or simply used as a chemical analysis.

DSC is the thermal analysis technique that give thermal information of a material. The analysis is in which the difference in the amount of heat required to increase the temperature of a sample and reference is measured as a function of temperature. Generally, the temperature program for a DSC analysis is designed such that the sample holder temperature increases linearly as a function of time. A sample of known mass is heated or cooled and the changes in its heat capacity are tracked as changes in the heat flow. The working procedure of DSC is similar to TGA but give different information. Usually, DSC analysis is give the thermal properties such as melting point, glass transition temperature, and crystallization temperature. Compare with TGA, DSC allows the information by raising the heating and cooling again. Especially, the phase transition or number of crystalline phase of a material can be observed by DSC analysis. For example, if two or more melting points of a material are observed, the material consists of two or more phases rather than a single phase.

2-2. Electrochemical analysis

2-2-1. Cell assembly

All electrochemical measurements of the antiperovskite pellets were conducted by using CR-2032 coin cell because the coin cell is good at protecting the solid electrolyte from moisture. The configuration of the cell is composed with SUS/Li/solid electrolyte/Li/SUS layers with thickness 0.30mm (Li-foil), 0.50mm (SUS), and 0.40mm (antiperovskite pellet) for DC-cycling test. To analysis Li^+ conductivity of the electrolytes, the main composition of the cell is SUS/In/solid electrolyte/In/SUS with thickness 0.05mm (In-foil), 0.9mm (antiperovskite pellet), 1.0 and 0.5 mm (SUS).

2-2-2. Cyclic voltammetry

Cyclic voltammetry is typical technique that the current flow can be measured by controlling the potential of the working electrode. This method is a principle of observing the change of current while applying voltage at a constant scan rate (mV/s). This electrochemical analysis provides many information such as the oxidation and reduction mechanism of a material, reversibility from the voltage gap of oxidation and reduction, and reactivity from area of current x voltage [8-10]. The measurement can also calculate the diffusion coefficient of lithium ions diffused into an active material through a current change that varies with the scan rate [11, 12].

When the cyclic voltammetry applied to solid electrolyte, its purpose is to evaluate the electrochemical stability of solid electrolyte [13, 14]. The configuration of the cell for the cyclic voltammetry is mainly composed by symmetric Li/electrolyte/SUS or

Li/electrolyte/Cu (reference/working/counter electrodes) [13]. The stability of the solid electrolyte is evaluated by comparing the current change while the voltage is being scanned at a constant rate. To accurate comparison for the electrical conductivity of solid electrolytes by cyclic voltammetry, Hebb-Wagner polarization technique have been developed [14]. As the technique, the electronic conductivity can be calculated as followed equation.

$$\sigma_e = \frac{\partial I}{\partial V} \frac{d}{A} \quad (2.2)$$

where I is the electrical current, V is the applied voltage, A is the surface area of a solid electrolyte, d is the thickness of the electrolyte, and σ_e is electronic conductivity. The measurement method using the symmetric cell is performed by gradually increasing the polarization from a low voltage as in a typical cyclic voltammetry. When the current value in the voltage range of the steady state condition close to the stable equilibrium state from the generated polarization is expressed as a function of the voltage, it is obtained as the polarization curve. The slope at this time is defined as the derivative value and the electric conductivity is calculated.

2-2-3. Direct current cycling (DC-cycling)

DC-cycling measurement is one of the galvanostatic measurement such as galvanostatic charge-discharge and galvanostatic intermittent titration technique. The simple electrochemical analysis is conducted by applying the constant current to a cell during charge and discharge with time cut off condition. Recently, this measurement has been used to evaluate the electrochemical stability of solid electrolyte materials

(versus Li metal Li/Electrolyte/Li) [15]. Compare with cyclic voltammetry, DC-cycling is good for comparing electrochemical reactivity as well as resistance of solid electrolytes. The example of DC-cycling is in Figure 1.14 [56]. When the solid electrolyte reacts with the lithium metal, the voltage of the cell changes in an increasing direction. The reason of increasing voltage is the resistance by SEI formation. As followed the simple ohm's law ($V=IR$), the voltage increases by some resistance factor when the constant current (mA/cm^2) is applied. Because other conditions are same, the resistance is considered by SEI formation between solid electrolyte and Li metal like Li/SEI/SE. Conversely, when the voltage is maintained at a constant value, the solid electrolyte material is considered stable with Li metal. The electrolyte may not react with Li metal or form the SEI with very slow rate. In other cases, the solid electrolyte reacts with Li metal at initial cycles and formed stable SEI. Therefore, the voltage changes not occur after the first few cycles. This analysis is simple but give many information about electrochemical stability of a material.

2-2-4. Electrochemical impedance spectroscopy (EIS)

EIS is a powerful technique to measure the electrical impedance resistance of an electrode or whole cell system. The impedance of an electrochemical system is defined as the resistance when an AC voltage or current is applied over a range of frequencies. The current-voltage relationship of the impedance can be expressed as followed equation.

$$Z(\omega) = \frac{V(t)}{I(t)} = \frac{V_m \sin(\omega t)}{I_m \sin(\omega t - \theta)} = Z \exp(j\theta) \quad (2.3)$$

where $v(t)$ and $I(t)$ are AC voltage and current, $Z(\omega)$ is impedance, ω is frequency ($\omega=2\pi f$). The equation is derived by Euler's rule as below:

$$Z(\omega) = Z_{re} + iZ_{im} \quad (2.4)$$

where Z_{re} and Z_{im} are the real and imaginary parts of the impedance in Nyquist plot which is one of the methods for expressing impedance like Figure 2.3. From the obtained result, an equivalent circuit is deduced and is proved by the fitting procedure. The equivalent circuit gives the resistance component. For example, the real impedance value on x-axis from the O to initial value is mass transfer resistance considered as electrolyte resistance, the real value of the diameter of semicircle is charge transfer resistance related with a surface area of an electrode, and the Warburg region which is the tail is Warburg impedance related with lithium diffusion coefficient of an active material. In the case of the solid electrolyte, the way to interpret the equivalent circuit is different. Fig 8 shows a suitable example for equivalent circuit of solid electrolyte. The real value from 0 to first semicircle means bulk resistance by a crystal structure and the insufficient contact between the particles of an active material and a solid electrolyte material. The second semicircle is the resistance by the grain boundary meaning a crack of solid electrolyte pellet. These factors are main resistance by solid electrolytes. The ionic conductivity of the solid electrolyte is calculated by below equation.

$$\sigma = \frac{l}{RA} = S\text{cm}^{-1} \quad (2.5)$$

where l is thickness of a solid electrolyte pellet, R is the resistance, and A is the area of the pellet.

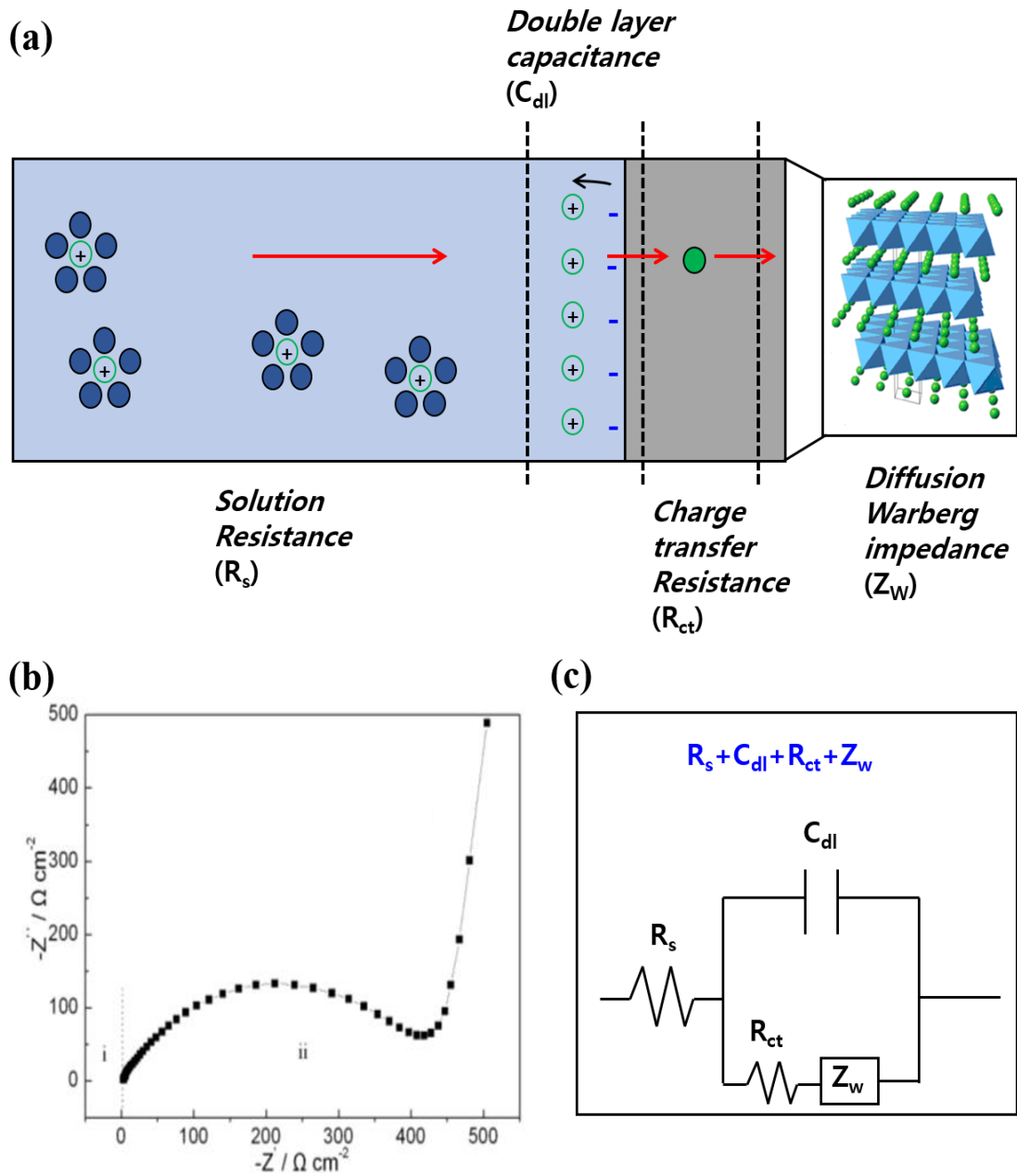


Figure 2.3 (a) The Li^+ diffusion mechanism of lithium ion batteries, (b) Nyquist plot of an electrode, and (c) equivalent circuit from the Nyquist plot.

References

- [1] Pope, C. G. X-ray diffraction and the Bragg equation. *J. Chem. Educ* **74**, 129 (1997).
- [2] Ladd, M. X-ray reflection and the Bragg equation. *Physics Education* **7**, 368 (1972).
- [3] Hammond, C. & Hammond, C. *Basics of crystallography and diffraction*. Vol. 214 (Oxford, 2001).
- [4] https://en.wikipedia.org/wiki/Infrared_spectroscopy
- [5] Sheng, L. H. *Nanostructured Phosphate-based Electrode Materials for Lithium Batteries*, 124-125 (2012).
- [6] Goldstein, J. *et al. Scanning electron microscopy and X-ray microanalysis: a text for biologists, materials scientists, and geologists*. (Springer Science & Business Media, 2012).
- [7] <https://www.ammrf.org.au/>
- [8] Gosser, D. K. *Cyclic voltammetry: simulation and analysis of reaction mechanisms*. Vol. 43 (VCH New York, 1993).
- [9] Kounaves, S. P. 709-726 (Prentice Hall, Upper Saddle River, NJ, USA, 1997).
- [10] Sheng, L. H. *Nanostructured Phosphate-based Electrode Materials for Lithium Batteries*, 121 (2012).
- [11] Tang, S., Lai, M. & Lu, L. Li-ion diffusion in highly (003) oriented LiCoO₂ thin film cathode prepared by pulsed laser deposition. *Journal of Alloys and Compounds* **449**, 300-303 (2008).
- [12] Wen, C. J., Boukamp, B., Huggins, R. & Weppner, W. Thermodynamic and mass transport properties of "LiAl". *Journal of The Electrochemical Society* **126**, 2258-2266 (1979).
- [13] Neudecker, B. & Weppner, W. Li₉SiAlO₈: a lithium ion electrolyte for voltages above 5.4 V. *Journal of the electrochemical society* **143**, 2198-2203 (1996).
- [14] M. H. Hebb, *J. Chem. Phys.*, **20**, 185 (1952).
- [15] Hood, Z. D., Wang, H., Samuthira Pandian, A., Keum, J. K. & Liang, C. Li₂OHCl crystalline electrolyte for stable metallic lithium anodes. *Journal of the American Chemical Society* **138**, 1768-1771 (2016).

Chapter 3. Study of electrochemical stability and ionic conductivity for Li_2OHCl

3-1. Introduction

Li_2OHX type materials ($\text{X}=\text{Cl}$ and Br) have the advantages such as higher electrochemical stability [1, 2] and easier synthesis than Li_3OX types. The material has a low melting point that can be applied to the melting method to reduce grain boundary. However, the material showed low ionic conductivity. The low ionic conductivity was improved, but the method did not show excellent effect that the ionic conductivity was increased by one order at high temperature [1]. To improve the low Li^+ conductivity, $\text{Li}_2(\text{OH})_{0.9}\text{F}_{0.1}$ was studied [2]. Replacing of F on OH site decreases the concentration of H^+ ions and stabilized the cubic phase from orthorhombic phase. As the results, the conductivity was improved 2 orders at 25°C [2].

Base on the above study, we have tried to study F and Br doped Li_2OHCl to improve the ionic conductivity and electrochemical stability. However, the basic experiments for Li_2OHCl were conducted to establish the criteria such as electrochemical measurements for Li_2OHCl electrolyte before the main study. Due to the air sensitivity of Li_2OHCl , all experimental including characterizations was conducted in Ar or N_2 -filled atmosphere. XRD and FT-IR was conducted to analysis the crystal structure, OH bond in the material, and air-sensitivity. For measure thermal stability and melting temperature of the material, TGA and DSC were performed. Cyclic voltammetry and DC-cycling were used to study the electrochemical stability of the electrolyte. To analysis the Li^+

conductivity of the Li_2OHCl pellets by processing cold-press, the EIS measurement was used.

3-2. Experimental

3-2-1. Synthesis of Li_2OHCl

Figure 3.1 shows the procedure of Li_2OHCl synthesis. All synthesis procedures were conducted in Ar atmosphere or sealed container due to the sensitivity of the antiperovskite materials. Li_2OHCl electrolyte which is pristine material was synthesized with LiOH (98.0% \geq , Sigma-Aldrich) and LiCl (99.0% \geq , Sigma-Aldrich) as starting materials. The materials were stored and weighted with molar ratio in an argon atmosphere glove box. After all reagents were grinded on a pestle bowl, the samples were placed in a jar with sealed to a parafilm and Teflon film and taken out as a glove box. The materials in the jar were mixed by using wet ball-mill with a mixture of hexane as a solvent, 1mm and 10 mm ZrO_2 balls at 450 rpm for a few hours. After ball-mill, the materials are then put back into the glove box in the jar, the mixture are dried to evaporate the remain solvent. The dried mixture was placed in an Al-crucible. Then, the crucible was sealed with Heat-resistant Kapton tape on the crucible sides and taken out the glove box and then, heated to 300°C (5°C/min) for 4hours and naturally cooled. The samples were then become in a hardened form and were round to a fine powder with a pestle and ball milling again using a mixture of hexane, 1mm and 5 mm balls at 400rpm for a few hours and finally, the Li_2OHCl powders were dried in the glove box for 12 hours.

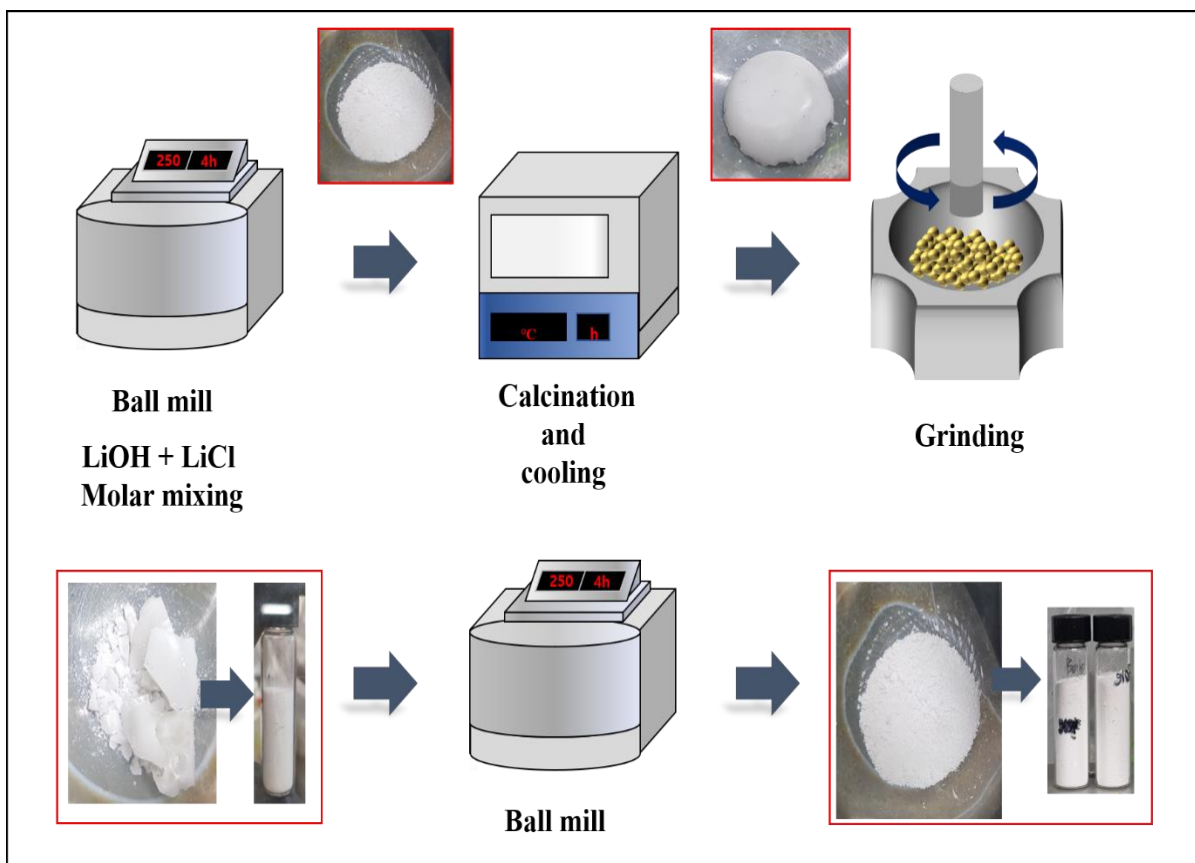


Figure 3.1 Schematic illustration for synthesis procedure of Li_2OHCl .

3-2-2. Characterization

The patterns of Li_2OHCl crystal phase were carried out with high resolution powder X-ray diffraction (HRPD) using a synchrotron in Pohang accelerator laboratory (PAL). The multiple detector systems of HRPD have 7 analyzer Ge (111) crystals and 7 scintillation detectors [3] providing good quality structure factor data by reducing peak overlaps. The method showing high resolution was implemented to ensure distinction from some peak noise caused by sealing the sample with Kapton tape to protect Li_2OHCl powders from moisture. All sampling including the powders and pellets for the XRD analysis including sealing was conducted in a Ar-filled glove box. Also, All XRD analysis were conducted in two theta range $10^\circ - 130^\circ$ with step size of 0.02° .

FT-IR were conducted to fine the oxygen-other elements bond vibration of Li_2OHCl including OH peak in a wavelength range $500\text{-}4000\text{ cm}^{-1}$ by IR AFFINITY-1S of Shimadzu. The KBr powders and Li_2OHCl powders were mixed and became the pellet by pressing at a pressure of 250ba in the glove box. After the pellet fixed on the sample holder is taken out of the glove box, the IR measurement was performed for 10 seconds to minimize exposure from moisture.

To analysis the surface images of the Li_2OHCl pellets and distribution of the elements (O, Cl) in Li_2OHCl , FE-SEM and energy dispersive spectroscopy (EDS) were performed with an accelerating voltage of 10 Kv by TESCAN. To prevent exposure to moisture, the Li_2OHCl pellets were made in the glove box and then, coated by Pt sputtering. TGA and DSC were conducted by Q600 of TA for investigation on thermal stability, melting point, and crystal phase of Li_2OHCl . The measurements were recorded

by the 0.25mg Li_2OHCl at with heating rate of $5^\circ\text{C}/\text{min}$ in a range of room temperature 25°C to 600°C . The samples were stored in the glove box and measured in N_2 atmosphere as the carrier gas during the tests.

3-2-3. Cell assembly

All electrochemical measurements of Li_2OCl electrolyte were performed by using CR-2032 coin cell. According to the explanation in chapter 2-2-1 and Figure 3.2, the composition of the coin cell is divided into three cases which is cyclic voltammetry, DC-cycling, and electrochemical impedance spectroscopy (EIS). The Li_2OHCl pellets for the measurements were prepared by pressing at a 270ba for a few minutes using 0.12g (cyclic voltammetry, DC-cycling) and 0.20g for (EIS).

The procedures of the cell assembly for each measurement are described in Figure 3.2. In the case of cyclic voltammetry, the Li_2OHCl pellet was first made as described above and then, squeezed again with one lithium foil and one SUS plate (spacer) on opposite side of the pellet at a 40ba. The cell assembly for DC-cycling was also conducted by almost same procedure of the case of cyclic voltammetry except for using two lithium foil and two SUS plate on the both side of the pellet. For EIS analysis, the assembly also proceeds in a similar method to the other two cases except for using In-foil or SUS pellet as a current collector. The method is the normal cold pressing at the pressure 270ba for a few minutes and pressed again with two In-foils and two SUS plates.

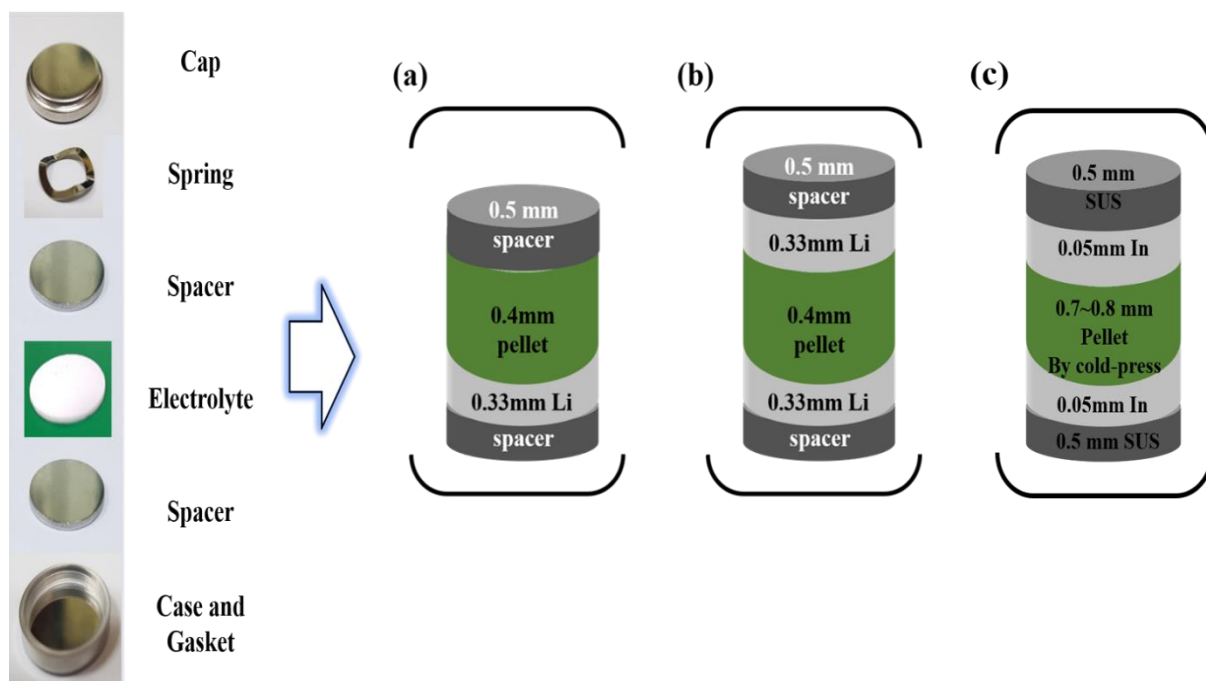


Figure 3.2 (a) Configurations of the symmetric cells for cyclic voltammetry, (b) DC-cycling, and (c) EIS measurements.

3-2-4. Electrochemical analysis

To analysis electrochemical stability and the voltage area of the reaction of SEI formation between Li_2OHCl and Li metal, cyclic voltammetry was conducted in the coin cell with a lithium foil as a reference electrode and a counter electrode of SUS plate at scan rate 0.5mV/s in a voltage range -1V to 6V and room temperature. DC-cycling measurements were performed by using the symmetric cell of Li/ Li_2OHCl /Li by applying a constant direct current 1.0 mA/cm² for 72 hours (30min per half a cycle) to study the self-stabilization of Li_2OHCl at room temperature and 140°C. The Li^+ conductivities of the pellet by cold press were evaluated by EIS analysis. The measurements were carried out on a SP-300 (Neo-science) instrument (100mV perturbation voltage and between 1MHz and 10mHz) as a function of temperature from 25°C to 145°C.

3-3. Results and discussion

3-3-1. characterization

Figure 3.3 (a) shows the XRD patterns of Li_2OHCl . Compare with the main peaks position and intensities of the results, the patterns which means orthorhombic phase were coincide with the results in reference [4]. The lattice pattern was observed at both side of the main peak centered at 32° and the peaks centered at 46° and 58°, and it was confirmed that the lattice pattern was closer to the orthorhombic phase than the cubic phase as compared with Li_3OCl [5]. The peaks are related to bonds change such as O-H-Cl bonds as 1Li is replaced by 1H (Li_3OCl to Li_2OHCl). As the results, the Li

vacancies are ordered to make each oxide ion coordinated by 4Li^+ and 2H^+ cations than 6Li^+ of Li_3OCl [2] and form the changed phases. Figure 3.3 (b) shows the XRD results of the Li_2OHCl when the powders of Li_2OHCl exposed at each hour (30s, 2min, 5min, 10min, and 30min). Compare with the XRD patterns of unexposed and 30 second exposed sample, the peaks position and intensity didn't changed. This result confirms that the sample not reacted with the molecules on atmosphere such as H_2O , which means no changes in properties or crystal structure until 30 seconds. After exposure 2 min, the XRD patterns of Li_2OHCl began to change, and completely transformed to complex patterns after 30 min. Although the exact reaction mechanism has not been studied, the results explained that Li_2OHCl decomposed to other binary materials such as LiOH .

To observe the OH bonds in Li_2OHCl from bond vibration, FT-IR measurement was conducted. The result of the measurement is in Figure 3.4 (a) and shows significant absorptions in the region of $3200\text{-}3600\text{ cm}^{-1}$, belonging to the OH stretch [6]. Compared to the IR results of Li_3OCl , it is clearly that the peaks are OH vibration. The peaks on 800 , 1450 , and 1700 cm^{-1} are considered as the peaks of the bonds such as O-Li-O and O-H-Cl in Li_2OHCl . Figure 3.4 (b) is the FT-IR results of the Li_2OHCl when the Li_2OHCl pellets exposed at each hour (30s, 2min, 5min 10 min, and 30min). compare with the IR results of unexposed and 30 second exposed sample, the IR spectrum didn't changed. This result confirms that the bonds composing Li_2OHCl and their strength were not changed, which means no changes in properties or crystal structure until 30 seconds. After exposure 2 min, the IR spectrum of Li_2OHCl changed, and completely broadened and hardly observed after 30 min. These results are consistent with the XRD results in Figure 3.3 (b) and explain that Li_2OHCl decomposed to other materials.

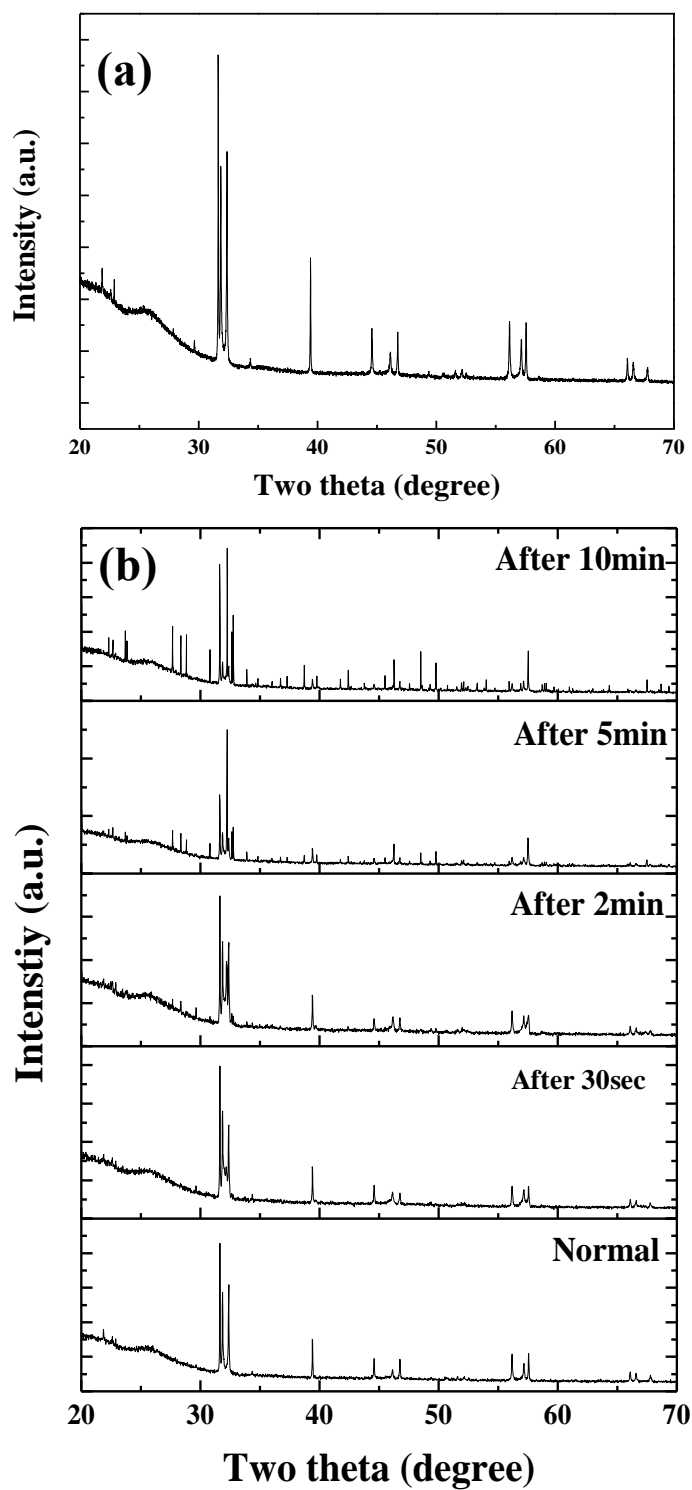


Figure 3.3 (a) XRD patterns of Li_2OHCl and (b) the Li_2OHCl samples exposed to air depend on time.

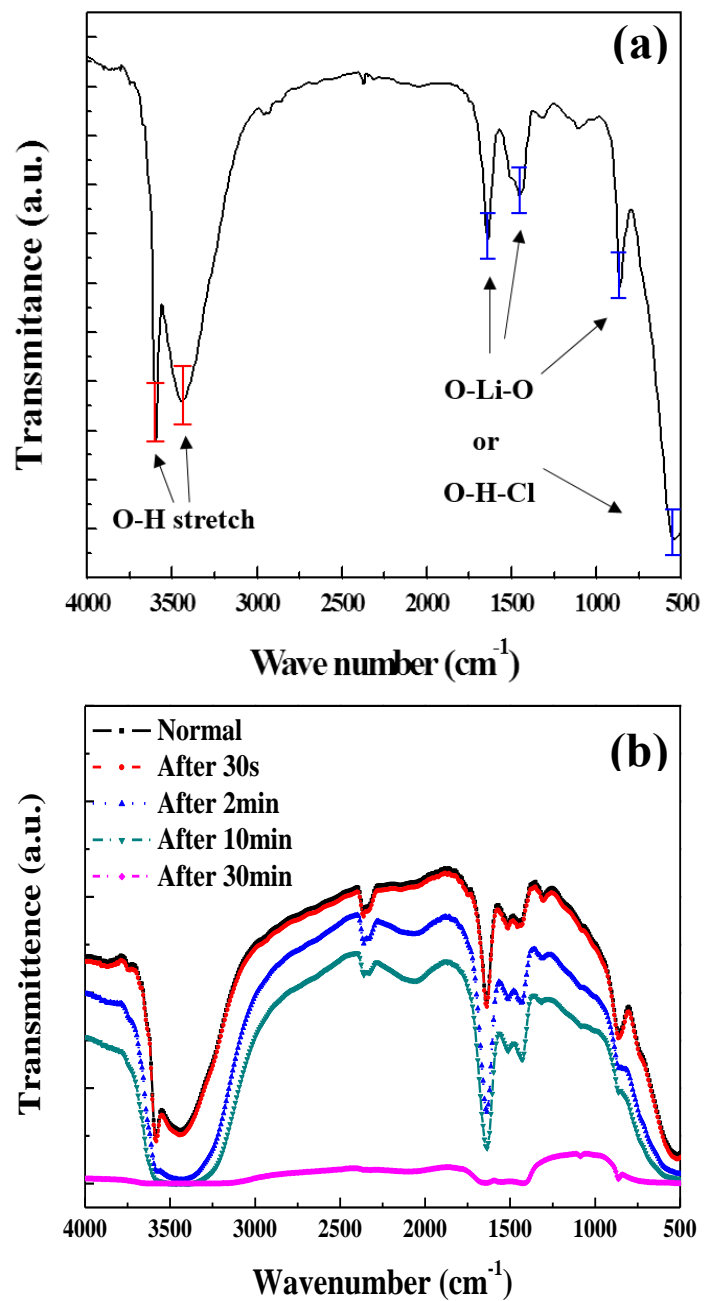
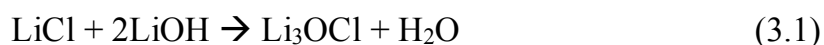


Figure 3.4 (a) FT-IR spectra of Li₂OHCl and (b) the Li₂OHCl samples exposed to air depend on time.

To clarify the melting point, phase purity, and thermal stability of Li₂OHCl, thermal measurements were used. The results of the thermal analysis in Figure 3.5 (a) TGA and (b) DSC of the Li₂OHCl in the temperature range 25 to 600°C. Li₂OHCl caused the mass loss event to occur at a 500-600°C. The loss amounts (wt%) by thermal decomposition were calculated to be 11.38 wt%. The mass loss is probably due to H₂ gas release by decomposition of Li₂OHCl at high temperature. This interpretation can be inferred from the synthesis conditions of Li₃OCl produced using LiOH and LiCl. The H₂ gas is released upon heating for a long time by the following mechanism [7, 8].



The DSC result in Figure 3.6 (b) shows the melting point 299°C of Li₂OHCl. The melting temperature agrees some with the result of previous study [6]. Only one exothermic peak appeared during the DSC measurement and explains that Li₂OHCl is composed with perfectly single phase. As the results of XRD, the single phase is orthorhombic structure.

To analysis of the surface images of the Li₂OHCl pellet and distribution of the elements O and Cl in Li₂OHCl, FE-SEM and EDS-mapping were performed. Figure 3.6 is (a) the SEM image of the Li₂OHCl pellet, (b) mapping image of overall elements, (c) oxygen, (d) chloride, and (e) the results of EDS analysis. The weight percentages of oxygen and chlorine are almost same (48.52:51.48) and agree with the composition of Li₂OHCl. The reason why the atomic percentage is different from the composition is probably because Li and H are not included. The mapping images in Figure (d) and (e) shows the distribution of oxygen and chloride. When the degree of dispersion of two elements is compared, it is confirmed that the two elements are well dispersed on overall surface of the pellet.

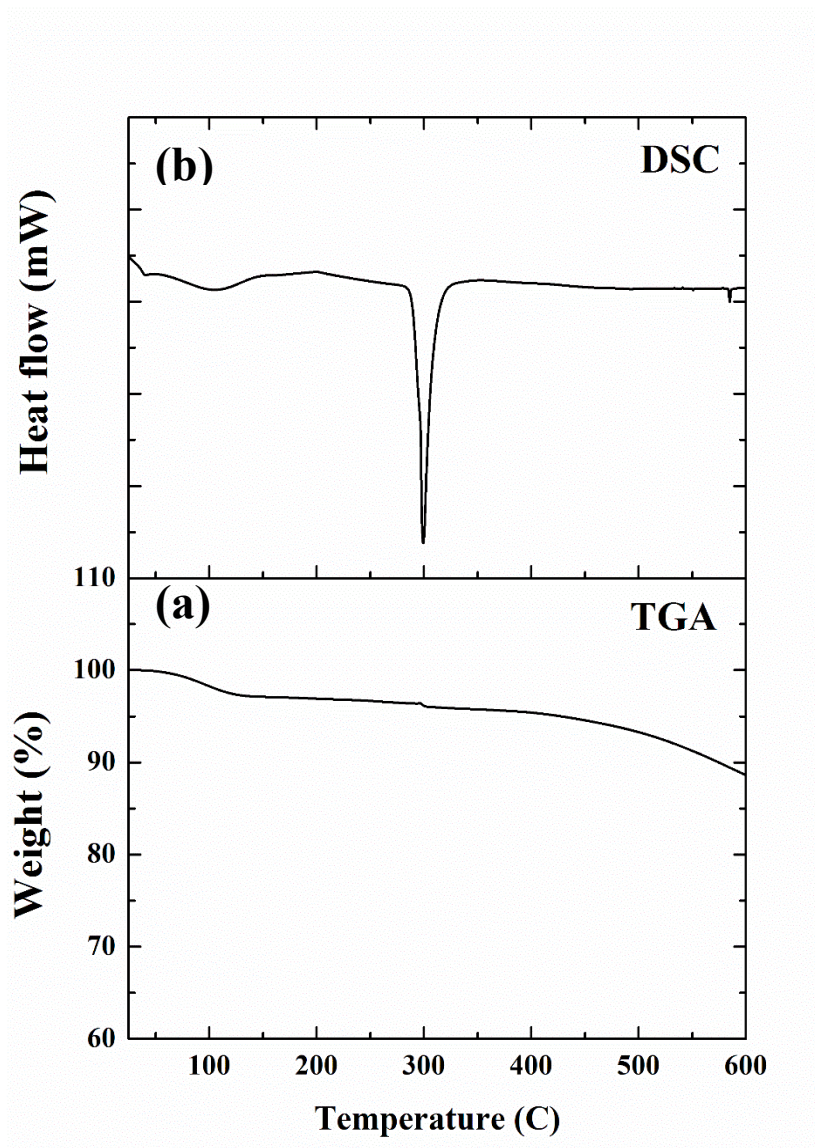


Figure 3.5 (a) TGA and (b) DSC data of Li_2OHCl from 25°C to 600 °C with heating rate 5°C/min in N_2 atmosphere.

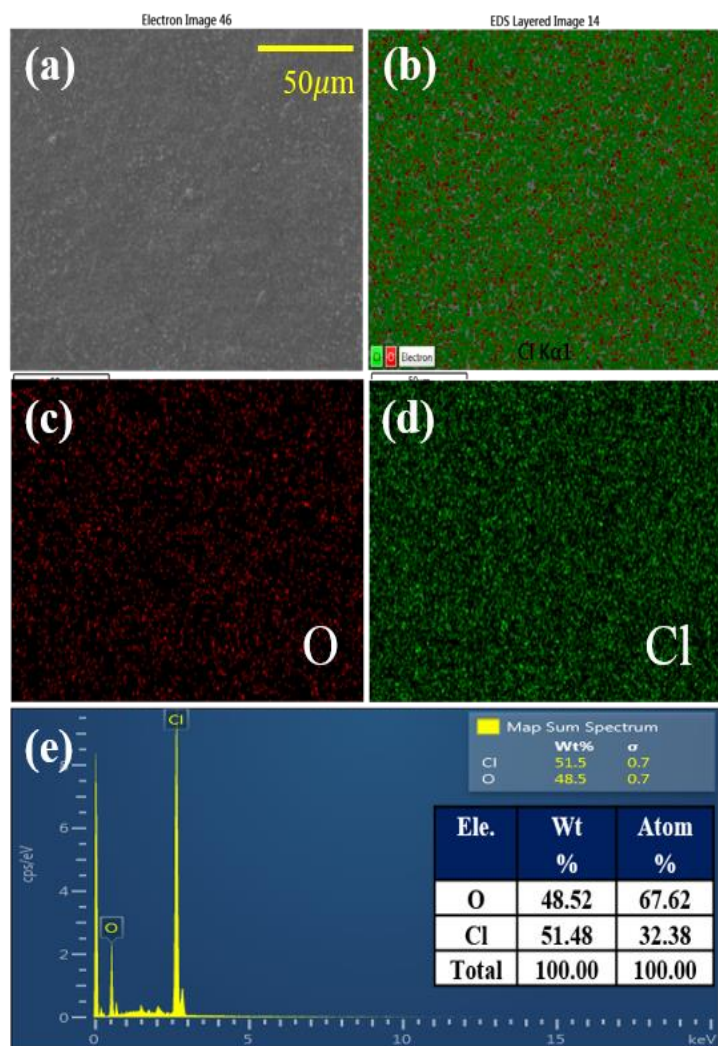


Figure 3.6 (a) SEM images of Li_2OHCl pellet, (b) mapping image for overall elements in Li_2OHCl pellet, (c) oxygen, (d) chloride, and (e) result from EDS analysis of the pellet.

3-3-2. Electrochemical analysis

Figure 3.7 (a) shows the result of cyclic voltammetry for the symmetric cell Li/Li₂OHCl/SUS at a scan rate 0.5 mV/s in a voltage range -1V to 6V. Li₂OHCl pellets show twin peaks at -0.05V to 1.5V voltage range. The peak is a Li₂OHCl reduction reaction and means the oxidation reaction of Li metal. Depending on the theoretical SEI formation mechanism, LiCl or Li₂O may be formed in this reaction range. According to SEM and EDS analysis, this reaction is mostly due to Li₂O formation, and the reason why the peak shape is twin is that it can be other lithium metal oxide such as Li₂O₂. A small current peak appears near 5V and is considered to be an oxidation peak due to LiCl formation by EDS results.

Hebb-Wagner polarization curves obtained from the cell Li/Li₂OHCl/SUS in Figure 3.7 (b). This polarization curve was plotted as a function of the current value generated at in the steady state range 1.70V to 2.25V where the oxidation reaction of Li was completed. From the slope of the linear function, which means the derivative $\frac{\partial I}{\partial V}$ of this graph, the electrical conductivity was calculated to be $1.05 \times 10^{-9} \text{ Scm}^{-1}$ according to the equation $\sigma_e = \frac{\partial I}{\partial V} \frac{d}{A}$ ($\frac{\partial I}{\partial V} = 1.36 \times 10^{-7}$, $A = 8.038 \text{ cm}^2$, $d = 0.062 \text{ cm}$) [9, 10]. This low electronic conductivity explain that Li₂OHCl is have good electrochemical stability.

To analysis the electrochemical stability and reactivity with Li metal of Li₂OHCl, DC-cycling measurements were conducted by using the symmetric cell of Li/Li₂OHCl/Li by applying a constant direct current 1.0 mA/cm² for 72 hours. Figure 3.8 exhibit (a) the cycling data at 25°C and (b) 140°C. When the measurement was

conducted at 25°C, the voltage of the cell almost not changed, which means that Li_2OHCl was almost not reacted with Li metal. This result explain that the Li_2OCHl is stable and reacts with Li metal very slowly. On the other hand, the result in Figure 3.8 (b) shows that the voltage increases gradually during the first few cycles and then remains unchanged. This result demonstrate that Li_2OHCl react with Li metal at initial few cycles for self-stabilizing. Although the voltage increases again after 55 cycles, the rate of the increase was slow. From these results, the increasing resistance of the cell by the SEI formation occurs distinctly at initial a few cycles and then hardly changes, which means that the SEI formation was formed at initial cycles and then, remained stable state.

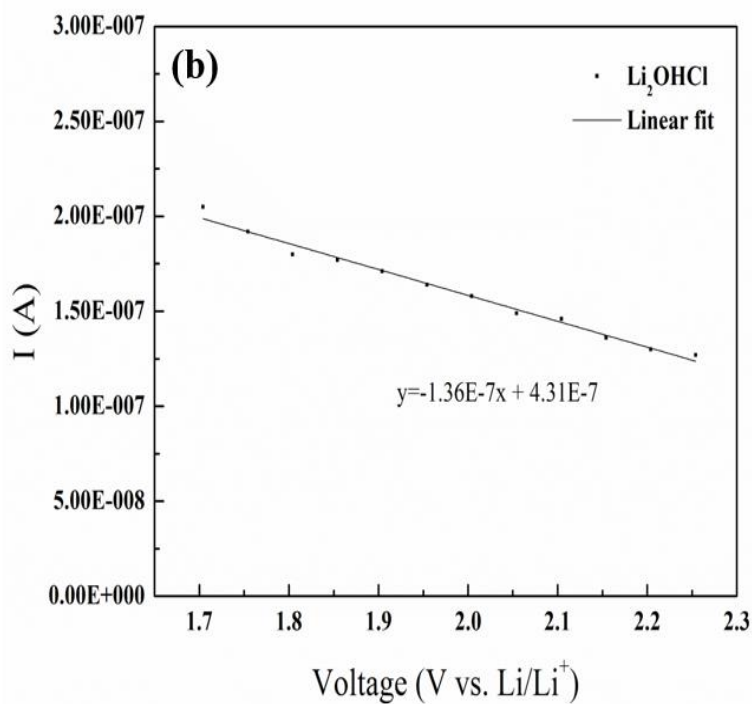
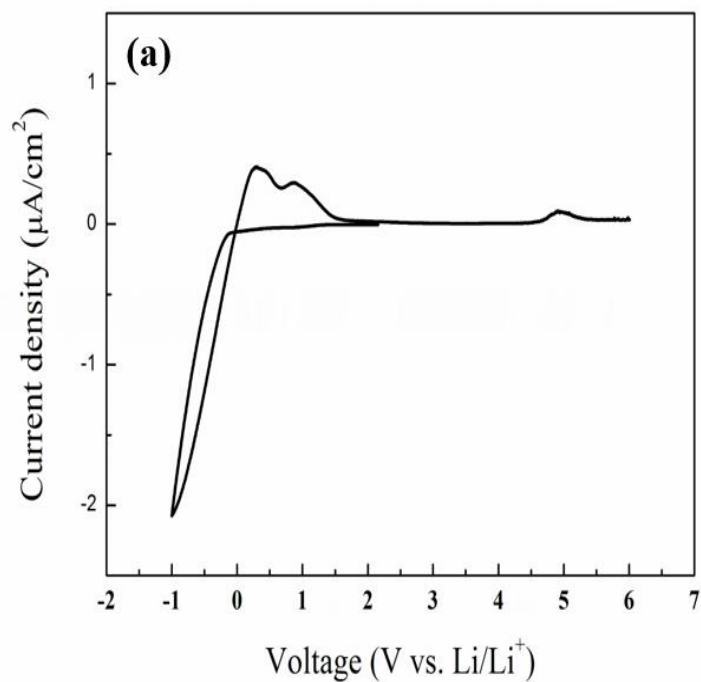


Figure 3.7 (a) Cyclic voltammetry for Li_2OHCl at scan rate 0.5 mV/s from -1V to 6V and (b) the Hebb-Wagner polarization curves obtained from the cell $\text{Li}/\text{Li}_2\text{OHCl}/\text{SUS}$

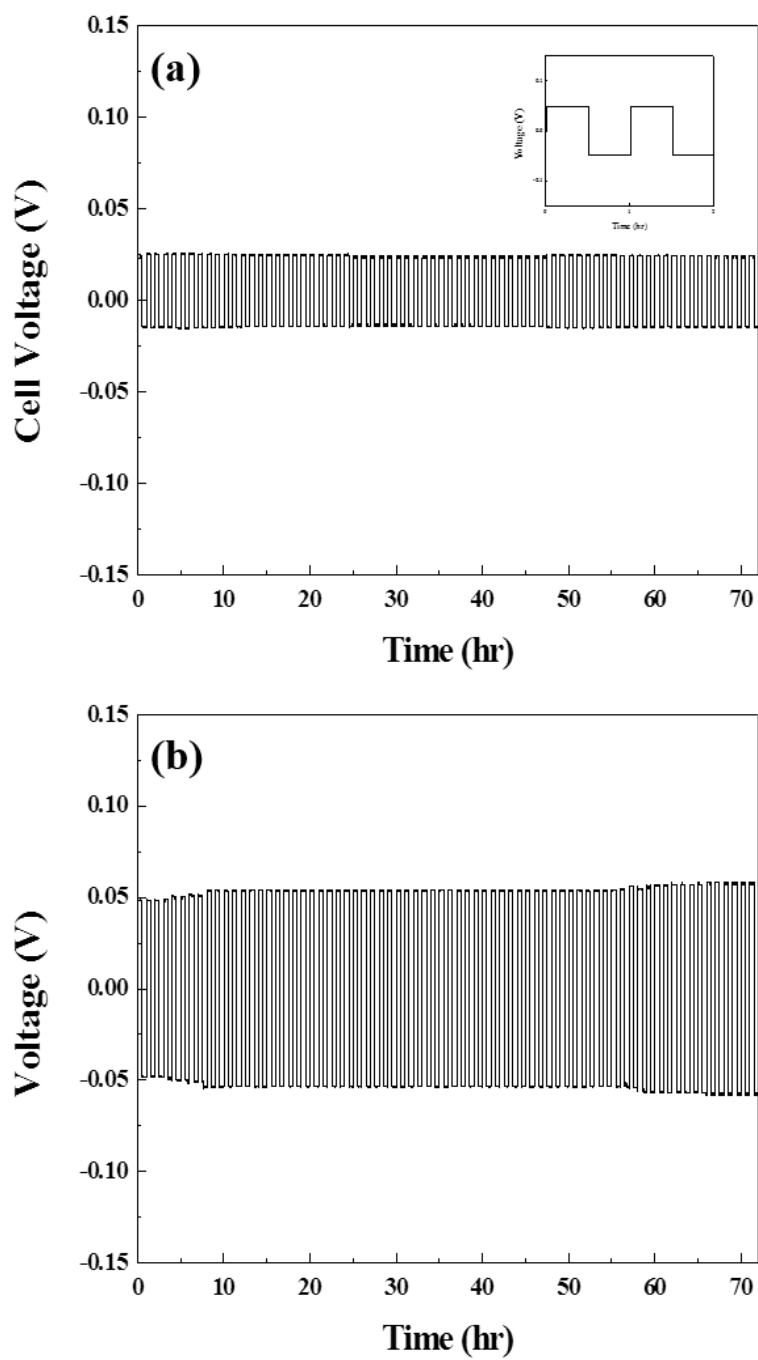


Figure 3.8 Results of DC-cycling tests of the symmetric cell Li/Li₂OHCl/Li with applied current density 1mA/cm² at (a) 25°C and (b) 140°C for 72hr.

To analyze the SEI film formed after DC-cycling, the test cells were released and the film was observed with naked eyes and SEM. Figure 3.9 shows (a) Li₂OHCl/SEI/Li layers in the cell after DC-cycling at 25°C, (b) the layers after DC-cycling at 140°C, (c) the SEM image of the surface of Li₂OHCl pellet (white layer in Figure 3.9 (b)), (d) the SEM images of the morphology of the SEI layer (black layer in Figure 3.9 (b)), (e)-(h) of the SEM and mapping images of the surface in the red box (Figure 3.9 (b)). Compare with the Li₂OHCl/SEI/Li layers after DC-cycling in Figure 3.10 (a) and (b), the SEI layer was clearly found in the cells conducted at 140°C as the black layer and the result coincide with the DC-cycling tests. As the result of SEM images of the surface difference between SEI layer and Li₂OHCl pellet, the SEI layers are composed with some materials showing uniform spherical particles. The materials can be inferred as followed the reaction mechanism [1].



As the reaction mechanism, the materials may be Li₂O or LiCl. From the results of SEM and mapping images in Figure 3.9 (e)-(h), the materials almost are Li₂O than LiCl because the SEI layer consist of oxygen compared with the Li₂OHCl pellet composed with oxygen and chloride. Figure 3.11 is the results of (a) EDS analysis on the SEI surface. As the results, almost element is oxygen than chloride (weight percentages 98.84:1.16=O:Cl). These results coincide with Figure 3.8 and demonstrate that the SEI occur by oxygen related bond dissociation in Li₂OHCl. This result demonstrates that the twin peak of the cyclic voltammetry of the Figure and the current peak occurring near 5V are due to lithium oxide and LiCl due to lithium oxidation, respectively.

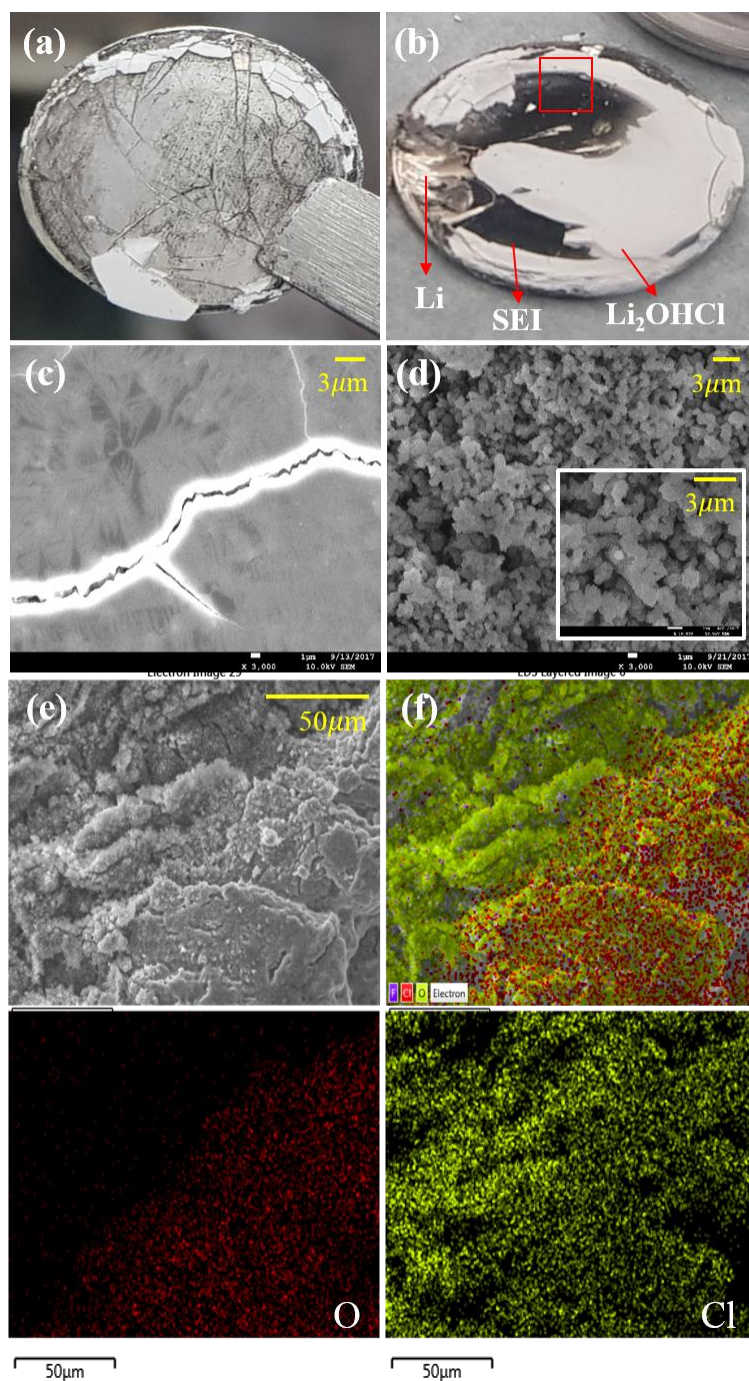


Figure 3.9 (a) Disassembled symmetric cells Li/Li₂OHCl/Li after DC-cycling tests at 25°C and (b) 140°C, (c) SEM images of Li₂OHCl pellet, (d) SEM images of the surface of SEI layer, (e) SEM images of the surface in the red box, and (f) mapping images of the red box.

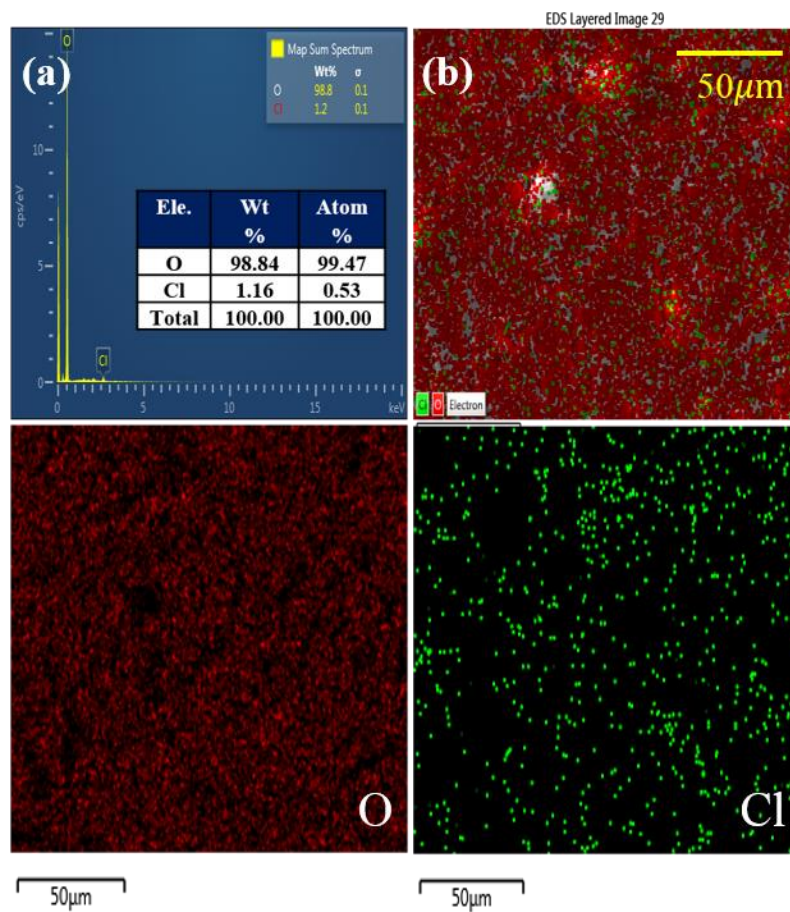


Figure 3.10 (a) Results of EDS analysis for the SEI layer and (b) mapping images.

Figure 3.11 (a) is a schema for the composition of resistance of a solid electrolyte. Unlike liquid electrolytes, solid electrolytes have two major types of resistance. One of the resistances is called bulk resistance and is caused by the summation of the activation energy for lithium migration by the solid crystalline structure and the poor two-dimensional interface contact between the electrolyte pellet and an electrode. The other is grain boundary resistance, caused by a three-dimensional complex Li^+ diffusion path due to the cracks that occur because the pellets are not completely dense. Figure 3.11 (b) shows a Nyquist plot of the Li_2OHCl pellet by EIS measurements at room temperature. The Nyquist plots for the electrolyte at different temperatures are in Figure 3.11 (c). All impedance plots in this study were fit by the equivalent circuit shown in the inset of Figure 3.11 (b). By the circuit and Figure 3.11 (a), the plots are expressed by bulk resistance (R_b), grain boundary resistance ($R_{G.B}$), and the low frequency part of the electrode capacitance (CPE_{EI}). These typical Nyquist plots clearly explain that almost pure Li^+ conductive characteristic of the present antiperovskite materials [1, 2, 11]. When the calculated Li^+ conductivity of the electrolytes, the grain boundary resistance can be considered as a factor to influence on pure ionic conductivity. However, the semicircles in the plots were observed in almost single circles. It means that the grain boundary resistance of the crystalline electrolytes does not contribute much to the total resistance as compared to the bulk resistance. Therefore, the Li^+ conductivities of the electrolytes were calculated by using the total resistance which is the diameter of the semicircles. The calculated Li^+ conductivity of Li_2OHCl pellet is $9.20 \times 10^{-6} \text{ Scm}^{-1}$. When comparing the value with that of previous studies, the conductivity calculated was slightly higher but is similar to the values of previous. The conductivity of this study is almost two times larger than

that of previous but the same order value with that of the study. Figure 3.11 (c) show the Nyquist plots with increasing temperature 25°C to 145°C. As a result, the plot exhibited both decreasing total resistances of the pellet and increasing Li⁺ conductivity. The Li⁺ conductivity at 145°C is 1.86 x 10⁻⁴ Scm⁻¹. From the Li⁺ conductivities by the Nyquist plot, the activation energy for Li⁺ migration can be calculated. The energy is obtained by the followed equation.

$$\sigma T = A \exp\left(-\frac{E_a}{kT}\right) \quad (3.3)$$

where E_a is the activation energy, k is the Boltzmann constant, and A_o is the intercept of the $\log(\sigma T)$ versus $1/T$ plot. The E_a is derived from the slopes of the Arrhenius plot. Figure 3.11 (d) shows the temperature dependency of the Li⁺ conductivity of Li₂OHCl pellet. The plot was well fitted by linear function and showed the linear slop meaning $-E_a/k$ as the equation 3.3. From the slop and equation, the activation energy was calculated as 0.59 eV.

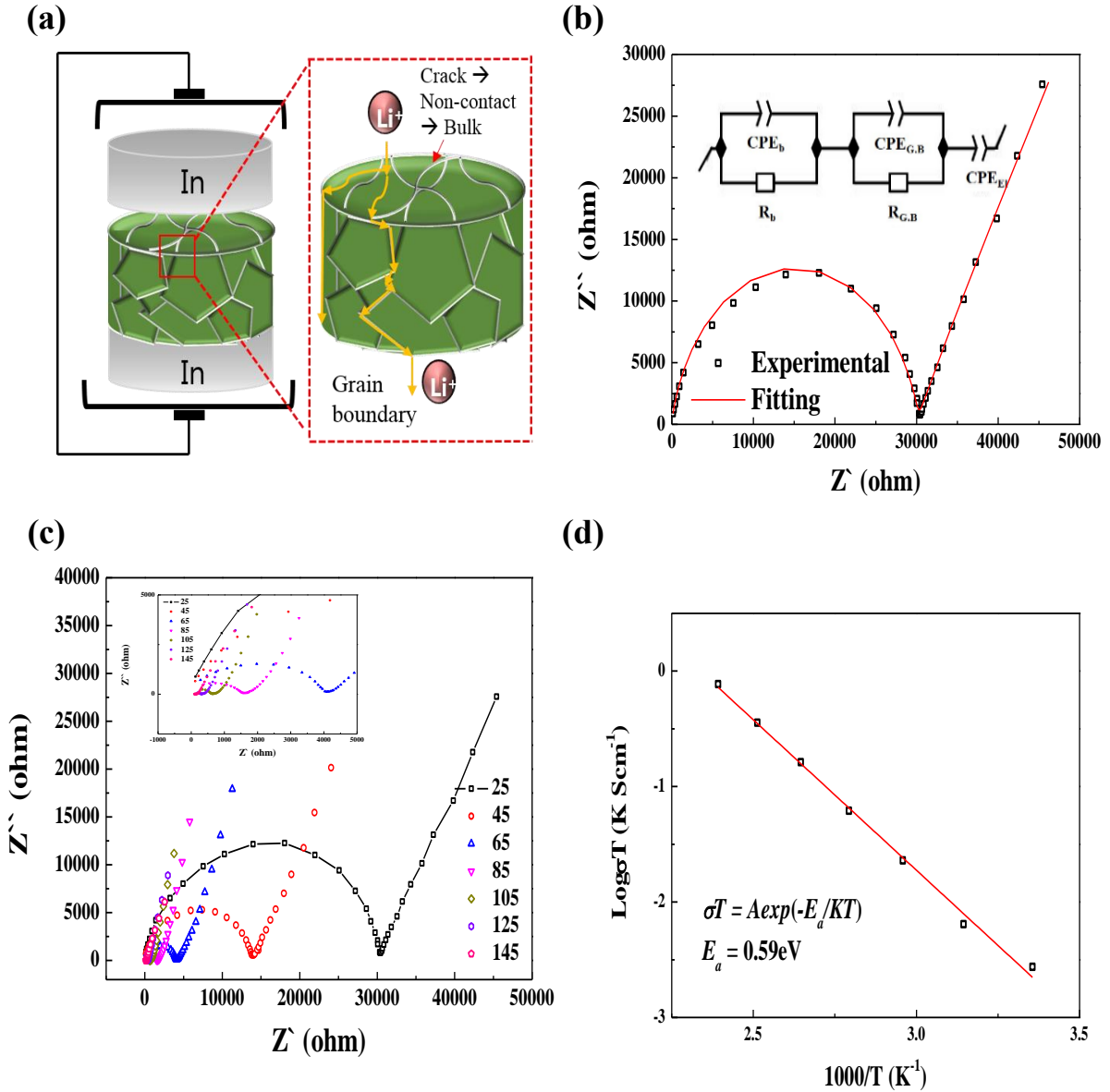


Figure 3.11 (a) schema for composition of resistance of solid electrolyte, (b) Nyquist plot from EIS data of $\text{Li}_2\text{OHC1}$ at 25°C, (c) the plot with increasing temperature 25°C to 145°C, and (d) Arrhenius plot of the total conductivity of the antiperovskite materials with In foil as electrodes; the activation energy E_a is derived by linear fitting of $\text{log} \sigma T$ versus $1/T$.

3-4. Conclusion

Li_2OHCl which is pseudo antiperovskite was synthesized by using solid-state method in the Ar-atmosphere due to its air sensitivity. XRD and DSC analysis confirmed that the antiperovskite material was composed of an orthorhombic single phase rather than a cubic phase. TGA thermal analysis showed that mass loss of 11.38% occurred in the temperature range from 25°C to 600°C. FT-IR analysis exhibited that the absorption peaks of the bonds including O-H composing the Li_2OHCl material were observed. From the cyclic voltammetry, a current peak determined by the oxidation reaction of lithium was observed in the voltage range of -0.05V to 1.5V and a small current peak considered to be due to the LiCl formation reaction at around 5V. The electrical conductivity of Li_2OHCl from the Hebb-Wagner polarization curve was calculated to be $1.05 \times 10^{-9} \text{ Scm}^{-1}$. As the result of DC-cycling, the voltage of the Li_2OHCl cell remained very stable at 25°C and the voltage increased during the first few cycles at 140°C. From the analysis of SEM and EDS components, it was confirmed that one SEI layer was formed between the lithium and solid electrolyte layer, and was confirmed that most of the layer was composed of lithium oxide such as Li_2O , not LiCl. From the EIS measurement, the Li^+ conductivity of Li_2OHCl pellet was $9.20 \times 10^{-6} \text{ Scm}^{-1}$. The conductivity increased by temperature dependency from 25°C to 145°C. By the dependency, the activation energy for Li^+ migration was calculated as 0.59 eV. Consequently, the Li_2OHCl electrolyte which has orthorhombic phase showed the self-stabilizing from the DC-cycling tests, low electrical conductivity, and good electrochemical stability versus Li^+ and proved to be compatible with lithium metal although the electrolyte showed low Li^+ conductivity.

References

- [1] Hood, Z. D., Wang, H., Samuthira Pandian, A., Keum, J. K. & Liang, C. Li_2OHCl crystalline electrolyte for stable metallic lithium anodes. *Journal of the American Chemical Society* **138**, 1768-1771 (2016).
- [2] Li, Y. *et al.* Fluorine Doped Antiperovskite Electrolyte for All-Solid-State Lithium Ion Batteries. *Angewandte Chemie International Edition* **55**, 9965-9968 (2016).
- [3] J.A. Kaduk, *Acta Crystallographica Section A : Foundations of Crastallography.* **50**, 259 (1994).
- [4] Eilbracht, C., Kockelmann, W., Hohlwein, D. & Jacobs, H. Orientational disorder in perovskite like structures of $\text{Li}_2\text{X}(\text{OD})(\text{X}=\text{Cl}, \text{Br})$ and $\text{LiBr}\cdot\text{D}_2\text{O}$. *Physica B: Condensed Matter* **234**, 48-50 (1997).
- [5] Zhao, Y. & Daemen, L. L. Superionic conductivity in lithium-rich antiperovskites. *Journal of the American Chemical Society* **134**, 15042-15047 (2012).
- [6] Li, S. *et al.* Reaction mechanism studies towards effective fabrication of lithium-rich antiperovskites Li_3OX ($\text{X}=\text{Cl}, \text{Br}$). *Solid State Ionics* **284**, 14-19 (2016).
- [7] Emly, A., Kioupakis, E. & Van der Ven, A. Phase stability and transport mechanisms in antiperovskite Li_3OCl and Li_3OBr superionic conductors. *Chemistry of Materials* **25**, 4663-4670 (2013).
- [8] Zhang, J. *et al.* High pressure-high temperature synthesis of lithium-rich Li_3O (Cl, Br) and $\text{Li}_{3-x}\text{Ca}_{x/2}\text{OCl}$ antiperovskite halides. *Inorganic Chemistry Communications* **48**, 140-143 (2014).
- [9] Neudecker, B. J., Weppner, W., $\text{Li}_9\text{SiAlO}_8$: A lithium ion Electrolyte for Voltages above 5.4V. *Journal of the Electrochemistry Society.* **143**, 2198-2203.
- [10] M. H. Hebb, *J. Chem. Phys.*, **20**, 185 (1952).
- [11] Zhu, J. *et al.* Enhanced ionic conductivity with $\text{Li}_7\text{O}_2\text{Br}_3$ phase in Li_3OBr antiperovskite solid electrolyte. *Applied physics letters* **109**, 101904 (2016).

Chapter 4. Study of ionic conductivity and electrochemical stability for $\text{Li}_2(\text{OH})_{0.9}\text{X}_{0.1}\text{Cl}$ and $\text{Li}_2\text{OHCl}_{0.8}\text{X}_{0.2}$ ($\text{X}=\text{F}, \text{Br}$)

4-1. Introduction

For improving low ionic conductivity of Li_2OHCl , John B. Goodenough *et al.* have investigated $\text{Li}_2(\text{OH})_{1-x}\text{F}_x\text{Cl}$, which is F doped antiperovskite material for OH [1]. Because fluorine has smaller ionic size than Cl, the substitution of F at OH site of Li_2OHCl not only reduces the concentration of H^+ hindering Li^+ diffusion by coulombic repulsion, but also form larger size of the cavity composed with Cl-O-Cl triangle cavity hole. As the results, the Li^+ conductivity of F doped $\text{Li}_2\text{OH}_{1-x}\text{F}_x\text{Cl}$ was improved. As the theoretical principle of ionic crystal structure, this explain is different with halogen doped Li_3OCl [2-5]. In the case of substitution with Br for Cl of Li_3OCl , Br doped $\text{Li}_3\text{OCl}_{1-x}\text{Br}_x$ showed higher Li^+ conductivity due to Br having larger size than Cl induce coulombic repulsion between anions and made larger cavity size and interstitial by Frenkel migration [4, 5, 7].

Based on above studies, we have investigated X doped $\text{Li}_2(\text{OH})_{0.9}\text{X}_{0.1}\text{Cl}$ and $\text{Li}_2\text{OHCl}_{0.8}\text{X}_{0.2}$ ($\text{X}=\text{F}$ and Br) to study the improved ionic conductivity mechanism as well as the electrochemical stability by the substitution with F and Br each having the smaller and larger ionic size than Cl.

4-2. Experimental

4-2-1. Synthesis of $\text{Li}_2(\text{OH})_{0.9}\text{X}_{0.1}\text{Cl}$ and $\text{Li}_2\text{OHCl}_{0.8}\text{X}_{0.2}$

The antiperovskite materials were synthesized with LiOH (98.0% \geq , Sigma-Aldrich) and LiCl (99.0% \geq , Sigma-Aldrich), and LiF (99% \leq , Sigma-Aldrich) or LiBr (99% \leq , Sigma-Aldrich) with molar ratio as the chemical formula of $\text{Li}_2(\text{OH})_{0.9}\text{X}_{0.1}\text{Cl}$ and $\text{Li}_2\text{OHCl}_{0.8}\text{X}_{0.2}$ in Ar-atmosphere glove box. After the reagents were grinded on a pestle bowl, the samples were placed in a jar and taken out as a glove box. The material in the jar were mixed by using wet ball-mill. After ball-mill, the materials in the jar are put back into the glove box, the mixture are dried. The dried mixture was placed in an Al-crucible. The crucible was sealed with a Kapton tape and taken out the glove box and then, heated to 300°C for 4 hours (F doped materials) and 350°C for 30min (Br doped materials) and naturally cooled. The samples were round to a fine powder with ball milling again and finally, the powders of the materials were dried in the glove box. All other additional conditions are the same as Li_2OHCl synthesis.

4-2-2. Characterization

All sampling and procedures including sealing from air for characterization were performed in the same condition as characterization of Li_2OHCl . The patterns of Li_2OHCl crystal phase were carried out with high resolution powder diffraction (HRPD) using a synchrotron in Pohang accelerator laboratory (PAL). All sampling including sealing was conducted in a Ar-filled glove box. The XRD analysis were performed in two theta range 20° - 70° with step size of 0.02°/sec. To analyze the concentration

changes of OH depending on the substitution site, FT-IR was used in a wavelength range 500-4000 cm^{-1} by IR AFFINITY-1S Shimadzu. The distribution of the elements in the antiperovskites were measured by FE-SEM and EDS (TESCAN) with an accelerating voltage of 10 kV. TGA and DSC were conducted by (Q600, TA) for investigation on thermal stability, melting point, and crystal phase of the materials. The measurements were recorded at heating rate in a range of 25°C to 600°C with heating rate 5°C/min.

4-2-3. Cell assembly

All electrochemical measurements for the antiperovskite materials were performed by using CR-2032 coin cell. The approximate cell assembly and conditions are the same as described in 2-2-3. For the tests, all pellets were prepared by pressing at a 270ba for a 3min using 0.12g (cyclic voltammetry, DC-cycling) and 0.20g (EIS). For the EIS analysis, the pellets were produced by the melting method in Figure 3.5.

4-2-4. Electrochemical analysis

To compare the electrochemical stability of the samples, cyclic voltammetry was conducted in the coin cell at scan rate 0.5 mV/s in a voltage range -1V to 6V. DC-cycling measurements were performed by applying a constant direct current 1.0 mA/cm^2 for 72 hours (30min per half a cycle) to study the self-stabilization of the electrolytes at room temperature and 140°C. The ionic conductivities of the pellets by melting method were evaluated by EIS analysis. The measurements were carried out on a SP-300 (Neoscience) instrument (100mV perturbation voltage between 1MHz and 10mHz) as a function of temperature from 25°C to 145°C.

4-3. Results and discussion

4-3-1. Characterization

Figure 4.1 and 4.2 are XRD patterns of the antiperovskite materials of (a) Li_2OHCl , (b) $\text{Li}_2(\text{OH})_{0.9}\text{F}_{0.1}\text{Cl}$, (c) $\text{Li}_2\text{OHCl}_{0.8}\text{F}_{0.2}$, (d) $\text{Li}_2(\text{OH})_{0.9}\text{Br}_{0.1}\text{Cl}$, and (e) $\text{Li}_2\text{OHCl}_{0.8}\text{Br}_{0.2}$ and magnified reflections around $2\theta = 32^\circ$ respectively. A line in the graphs refers to the peaks position at $2\theta = 32^\circ, 38^\circ, 46^\circ,$ and 58° in the orthorhombic Li_2OHCl . When comparing the XRD patterns based on the blue line, the peaks at both side of the peaks on $32^\circ, 46^\circ,$ and 58° disappeared according to the substitution of F and Br in Li_2OHCl . The results explain that the phase transition from orthorhombic phase to cubic phase by the substitution. As the anions of different sizes were displaced, the new bonds were in the crystal structure. For example, the O-Li-Br and O-H-Br bonds can be formed from existing bonds such as O-Li-O and O-H-Cl in Li_2OHCl as Br is substituted for each OH and Cl site. The new bonds and a volume of the crystal structures were changed, which caused a phase transition. This result can be explained that the tolerance factor increased when replacing other anions having F and Br having same electronic charge with the existing anions OH and Cl according to the previous description and studies [4]. The factor increased by F substitution for OH and then, increasing the factor makes the orthorhombic to cubic phase as followed equation [1]. The higher tolerance factors indicated that the antiperovskite structure approaches a less distorted pseudo cubic phase and promotes the displacive structural phase transition controlled by phonon softening [4]. Since the cubic structure is not perfect, the XRD patterns of the doped materials exhibited extra peaks. These are due to small tetragonal or orthorhombic distortions from the ideal cubic structure [5].

Compare with the peaks position of the Br and F doped materials, the peaks of the F substituted materials were almost the same with respect to the blue line, while the peaks those of the Br substituted materials were shifted to the left completely. As the Bragg equation $n\lambda = 2d_{hkl}\sin\theta_{hkl}$, the smaller 2θ value, the greater d-spacing of the lattice plane, and finally the unit cell volume increases. This result shows the structural difference of F substitution and Br substitution materials. As the large Br is substituted for Cl and OH, the volume of the structure is definitely increased. The increase in the repulsion between the anions would expand the volume and induce structural transition.

To analyze the concentration changes of OH depending on the substitution site, FT-IR was used. The result of the measurement is in Figure 4.3 of (a) Li_2OHCl , (b) $\text{Li}_2(\text{OH})_{0.9}\text{F}_{0.1}\text{Cl}$, (c) $\text{Li}_2\text{OHCl}_{0.8}\text{F}_{0.2}$, (d) $\text{Li}_2(\text{OH})_{0.9}\text{Br}_{0.1}\text{Cl}$, and (e) $\text{Li}_2\text{OHCl}_{0.8}\text{Br}_{0.2}$. The absorption peaks in the region of $3200\text{-}3600\text{ cm}^{-1}$ which are OH stretch observed in all the IR results. Compared with the peaks of the antiperovskites, the IR spectrums of Li_2OHCl , $\text{Li}_2\text{OHCl}_{0.8}\text{F}_{0.2}$, $\text{Li}_2\text{OHCl}_{0.8}\text{Br}_{0.2}$ were similar broadening and separation between two peaks on 3450cm^{-1} and 3600cm^{-1} while the peaks of $\text{Li}_2(\text{OH})_{0.9}\text{F}_{0.1}\text{Cl}$ and $\text{Li}_2(\text{OH})_{0.9}\text{Br}_{0.1}\text{Cl}$ showed the more broadening and less-separated shapes. Considering the composition of the materials, this result is believed to be due to the concentration change of OH in the antiperovskites. It can be considered that the halogens are located in the site of OH and Cl and occurs the structural change respectively. IR spectrum of F and Br substituted materials showed not only the existing absorption peaks on 800 , 1450 , and 1700 cm^{-1} but also new absorption peak on 1292 cm^{-1} which not is not founded in the IR result of Li_2OHCl . Compared to the XRD results, the peaks are considered by new bond vibration such as O-Li-Br and O-Li-F.

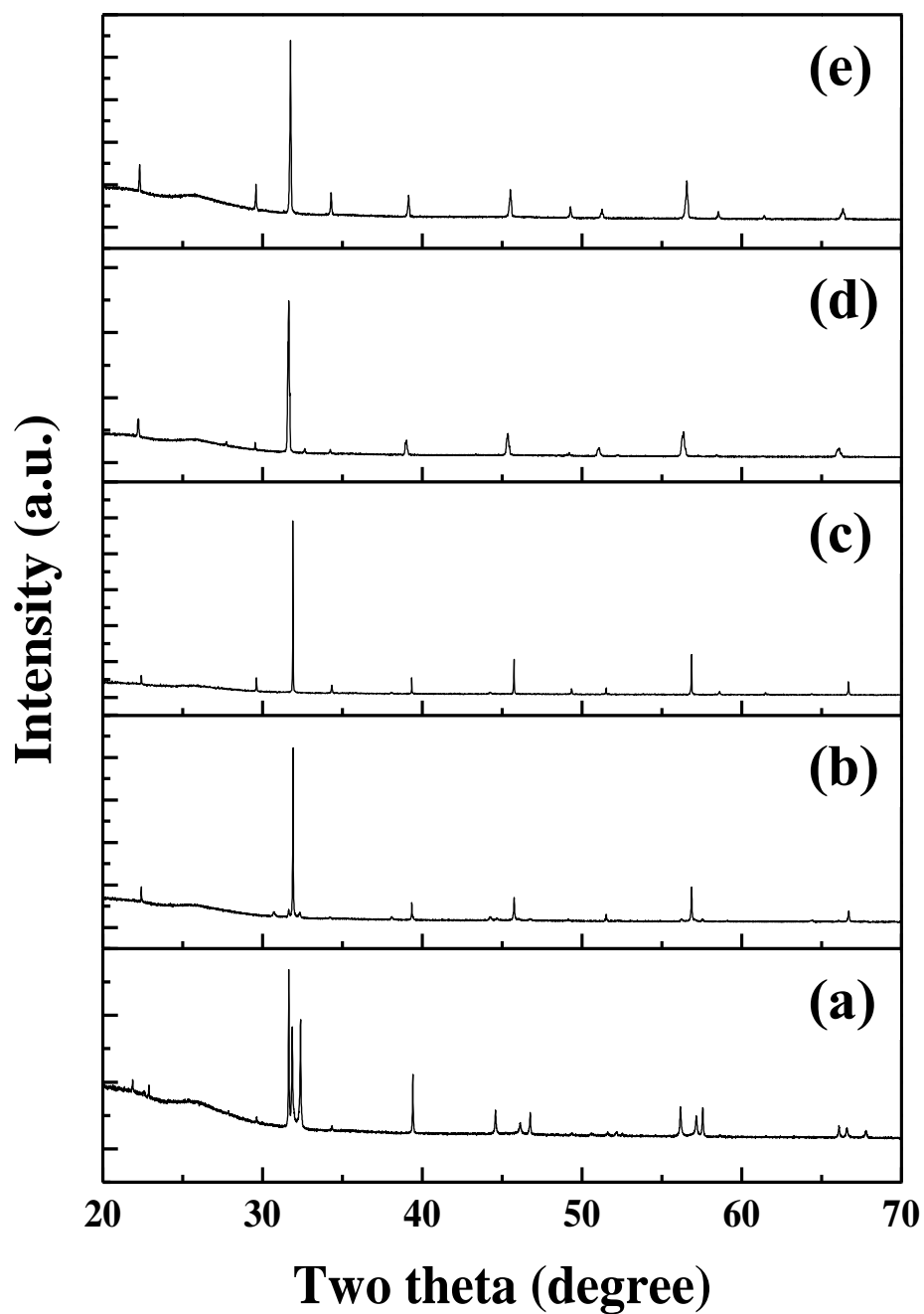


Figure 4.1 XRD patterns of the antiperovskite materials of (a) Li_2OHCl , (b) $\text{Li}_2(\text{OH})_{0.9}\text{F}_{0.1}\text{Cl}$, (c) $\text{Li}_2\text{OHCl}_{0.8}\text{F}_{0.2}$, (d) $\text{Li}_2(\text{OH})_{0.9}\text{Br}_{0.1}\text{Cl}$, and (e) $\text{Li}_2\text{OHCl}_{0.8}\text{Br}_{0.2}$.

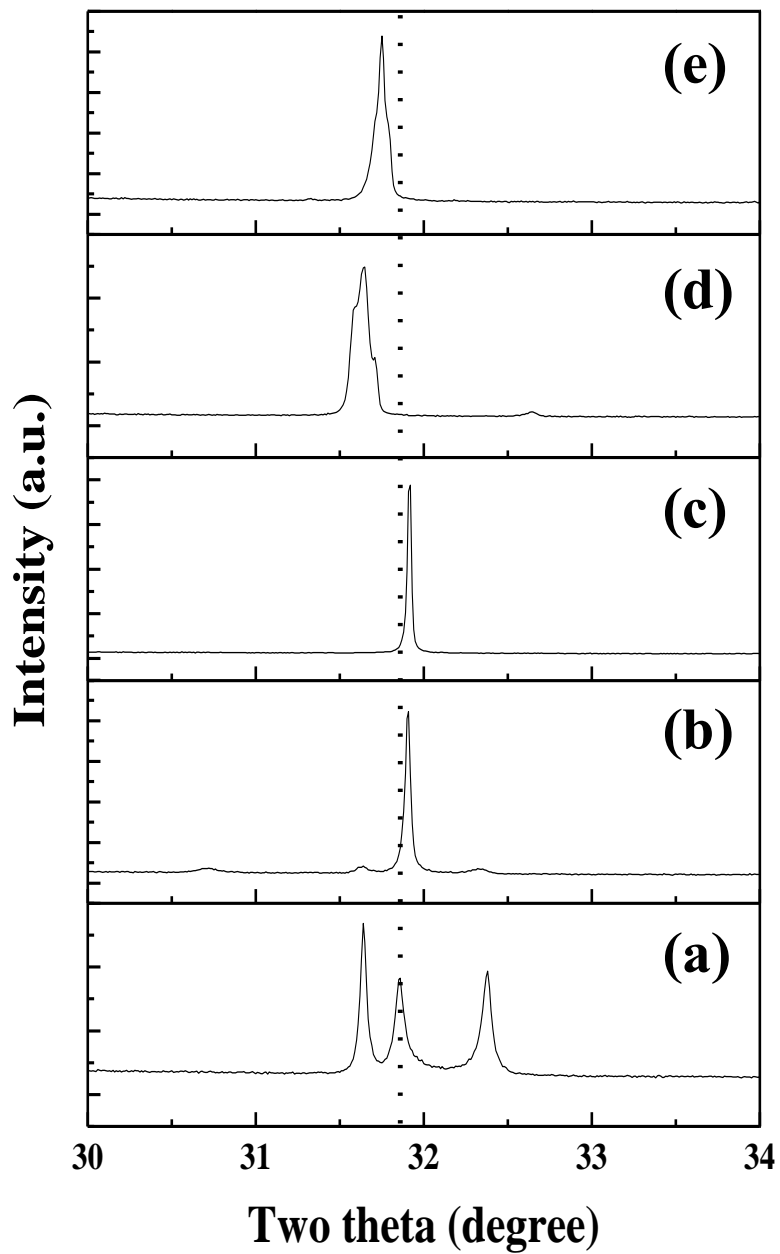


Figure 4.2 Magnified reflections magnified reflections around $2\theta = 32^\circ$ in the XRD patterns of (a) Li_2OHCl , (b) $\text{Li}_2(\text{OH})_{0.9}\text{F}_{0.1}\text{Cl}$, (c) $\text{Li}_2\text{OHCl}_{0.8}\text{F}_{0.2}$, (d) $\text{Li}_2(\text{OH})_{0.9}\text{Br}_{0.1}\text{Cl}$, and (e) $\text{Li}_2\text{OHCl}_{0.8}\text{Br}_{0.2}$.

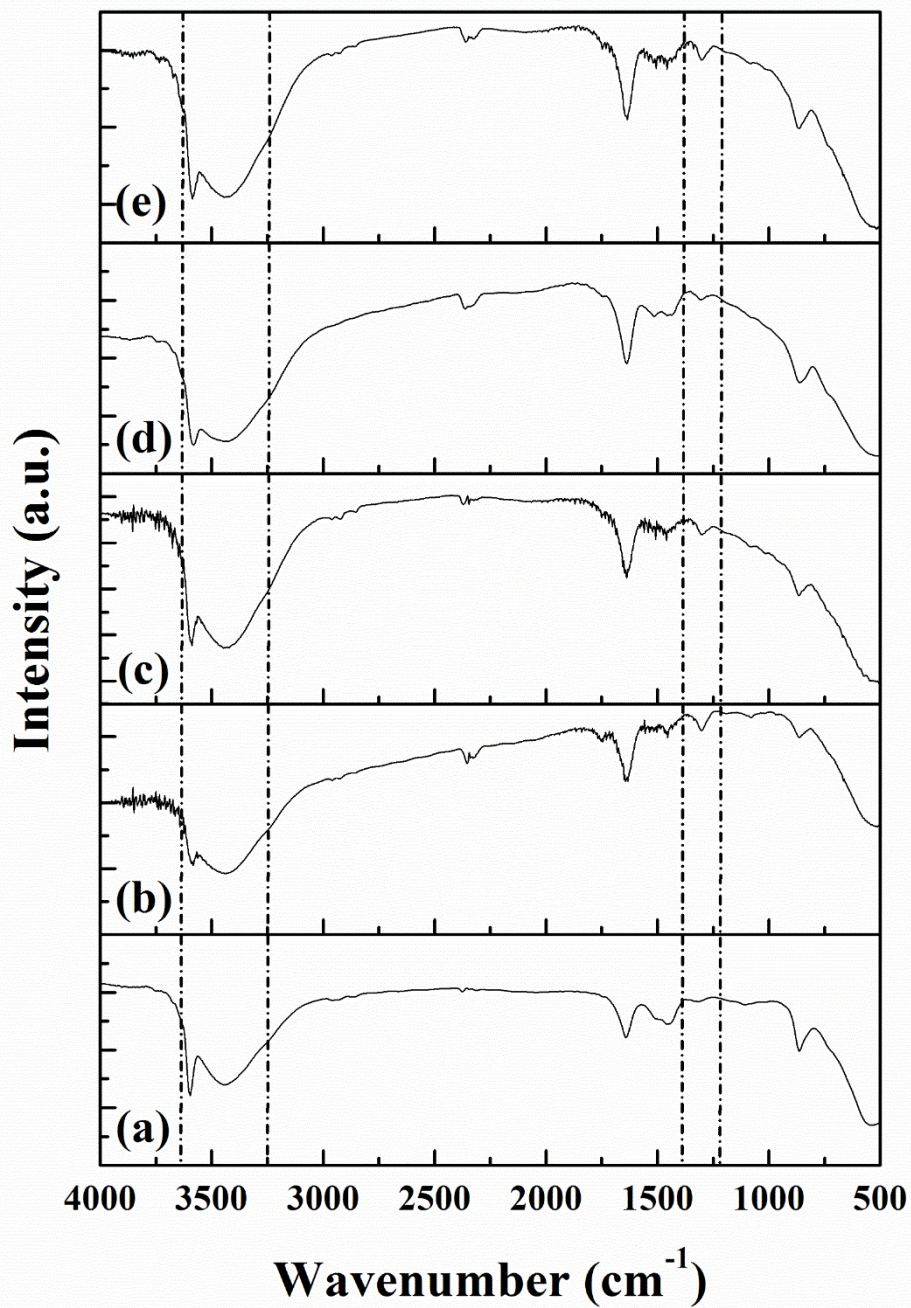


Figure 4.3 FT-IR spectra of the antiperovskites of (a) Li_2OHCl , (b) $\text{Li}_2(\text{OH})_{0.9}\text{F}_{0.1}\text{Cl}$, (c) $\text{Li}_2\text{OHCl}_{0.8}\text{F}_{0.2}$, (d) $\text{Li}_2(\text{OH})_{0.9}\text{Br}_{0.1}\text{Cl}$, and (e) $\text{Li}_2\text{OHCl}_{0.8}\text{Br}_{0.2}$.

Figure 4.4 shows the results of (a) TGA and (b) DSC of the antiperovskites (A: Li_2OHCl , B: $\text{Li}_2(\text{OH})_{0.9}\text{F}_{0.1}\text{Cl}$, C: $\text{Li}_2\text{OHCl}_{0.8}\text{F}_{0.2}$, D: $\text{Li}_2(\text{OH})_{0.9}\text{Br}_{0.1}\text{Cl}$, and E: $\text{Li}_2\text{OHCl}_{0.8}\text{Br}_{0.2}$). Table 4.1 shows summarized the melting point and mass loss of the antiperovskites from TGA and DSC. Compare with degree of mass loss, thermal stability was analyzed in the order of $\text{Li}_2(\text{OH})_{0.9}\text{F}_{0.1}\text{Cl} > \text{Li}_2\text{OHCl}_{0.8}\text{F}_{0.2} > \text{Li}_2(\text{OH})_{0.9}\text{Br}_{0.1}\text{Cl} > \text{Li}_2\text{OHCl}_{0.8}\text{Br}_{0.2} > \text{Li}_2\text{OHCl}$. These results explained that the chemical stability of the substituted materials was clearly improved than that of Li_2OHCl . From the results of XRD and FT-IR, it is considered that the phase transition from orthorhombic to stable cubic phase improved the structural and chemical stabilities by the tolerance factor. In the case of the substituted halogen species, the F doped materials exhibited lower mass loss than that of Br doped electrolytes. According to the results of XRD and FT-IR measurements, it is that the strength of the new bond is different. As the atomic number of the halogen group increases on the periodic table, the atomic size becomes smaller and the orbital overlap with the cation becomes stronger. The stronger bond strength in the solid electrolytes, the greater chemical stability. Table 4.2 [8] shows theoretically calculated bond dissociation energies (BDE). The BDE of H-F and Li-F is bigger than that of Br, which means that the bond is stronger.

Comparing the thermal stability with substitution sites, the F and Br substituted materials at the OH sites showed a smaller mass loss than those doped with Cl. The reason is due to the structure of Li_2OHCl . In the case of Li_2OHCl with an ideal cubic structure, it consists mainly of O-Li-O bonds and O-H-Cl bonds. When the F and Br sites are replaced with OH, O-Li-F or O-Li-Br bonds are increased. In contrast, when

the halogens are replaced with Cl sites, O-H-F or O-H-Br bonds are increased. This description is consistent with the TGA results and the BDE size in Table 4.2.

As a result of the melting points of antiperovskites in Figure 4.4 and Table 4.1, the melting points of the substituted materials were lower than those of Li_2OHCl . This result is eutectic effect due to displacive phase transition, which reduces the melting point and phase transition temperature of antiperovskites [4]. Unlike Li_2OHCl , the melting points of the pseudo-cubic phase was very small at 263°C, 266°C, 245°C, and 250°C in the DSC results of the substituted materials. These weak endothermic peaks are associated with extra Bragg peaks, which signify orthorhombic or tetragonal distortions of the XRD results. The remaining phases are considered to be some phase that has not changed in the cubic phase transition process by F and Br substitution, or a retransition from the cubic structure to those phases depending on the cooling rate [9]. When comparing the melting points including the remaining phases, the Br substituted materials showed a lower melting point than those with F substituted. The reason may be the structural volume difference due to the substitution of Br which is larger than OH and Cl, contrary to F substitution.

The dispersion and approximate content of the elements constituting the antiperovskites were analyzed by SEM and EDS measurements. Figure 4.5 shows the results of SEM and EDS mapping measurements of (a) $\text{Li}_2(\text{OH})_{0.9}\text{F}_{0.1}\text{Cl}$ and (b) $\text{Li}_2\text{OHCl}_{0.8}\text{F}_{0.2}$ (A: SEM images of the pellets of F doped materials, B: EDS results, C: overall mapping image, D: oxygen, E: chlorine, and F: fluorine). Both materials showed that the three elements were well dispersed throughout. When comparing the weight

percentage of the F substituted materials with the mapping images including F, it can be seen that the F weight percentage of $\text{Li}_2\text{OHCl}_{0.8}\text{F}_{0.2}$ is twice that of $\text{Li}_2(\text{OH})_{0.9}\text{F}_{0.1}\text{Cl}$. The reason that the atomic percentage does not agree with the composition is considered to be that the content of H in Li and OH is not included as in the EDS results of Li_2OHCl .

Br substituted materials also show differences in EDS and mapping image results according to Br content in Figure 4.6 (a) $\text{Li}_2(\text{OH})_{0.9}\text{Br}_{0.1}\text{Cl}$ and (b) $\text{Li}_2\text{OHCl}_{0.8}\text{Br}_{0.2}$ (A: SEM images of the pellets of F doped materials, B: EDS results, C: overall mapping image, D: oxygen, E: chlorine, and F: bromine). The weight percentage of Br in $\text{Li}_2\text{OHCl}_{0.8}\text{Br}_{0.2}$ is about 2 times larger than that of $\text{Li}_2(\text{OH})_{0.9}\text{Br}_{0.1}\text{Cl}$, and the difference in degree of dispersion can be confirmed through the mapping image.

Table 4.1 Melting points and calculated mass loss of the antiperovskite materials.

Sample	Melting point from DSC (°C)	Weight at 25°C (g)	Weight at 600°C (g)	Mass loss (%)
Li ₂ OHCl	299°C	10.9689	9.7206	11.38
Li ₂ (OH) _{0.9} F _{0.1} Cl	292°C	13.3318	12.5836	5.62
Li ₂ OHF _{0.2} Cl _{0.8}	291°C	12.0242	11.2306	6.60
Li ₂ (OH) _{0.9} Br _{0.1} Cl	276°C	11.8360	11.0276	6.83
Li ₂ OHBr _{0.2} Cl _{0.8}	287°C	12.0786	11.1099	8.02

Table 4.2 Bond dissociation energies of the binary bonding related with F and Br substituted antiperovskite materials.

Sample	A-B	<i>D</i>^o₂₉₈/KJ mol⁻¹
Li ₂ (OH) _{0.9} F _{0.1} Cl	Li-F	577
Li ₂ OHF _{0.2} Cl _{0.8}	H-F	570
Li ₂ (OH) _{0.9} Br _{0.1} Cl	Li-Br	418
Li ₂ OHBr _{0.2} Cl _{0.8}	H-Br	366

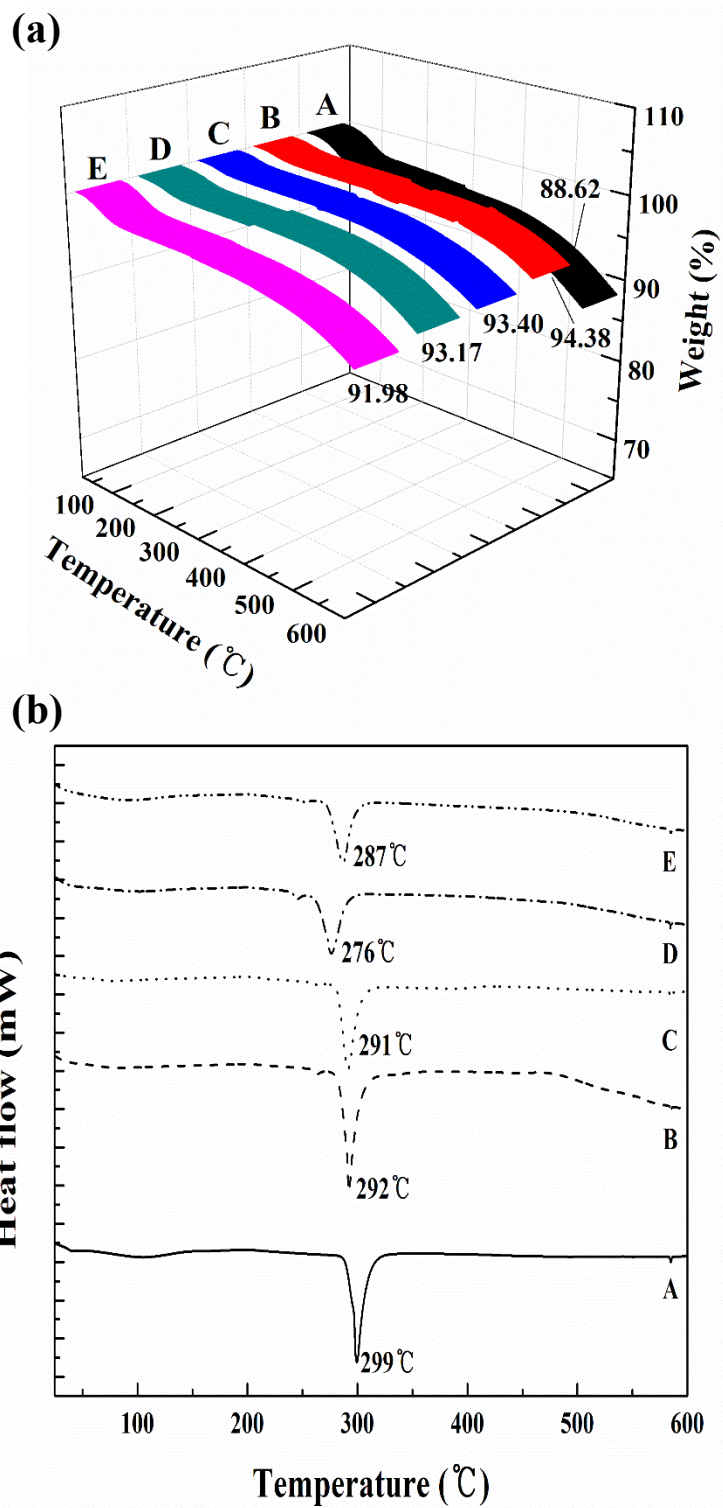


Figure 4.4 Results of (a) TGA and (b) DSC (A: Li_2OHCl , B: $\text{Li}_2(\text{OH})_{0.9}\text{F}_{0.1}\text{Cl}$, C: $\text{Li}_2\text{OHCl}_{0.8}\text{F}_{0.2}$, D: $\text{Li}_2(\text{OH})_{0.9}\text{Br}_{0.1}\text{Cl}$, and E: $\text{Li}_2\text{OHCl}_{0.8}\text{Br}_{0.2}$).

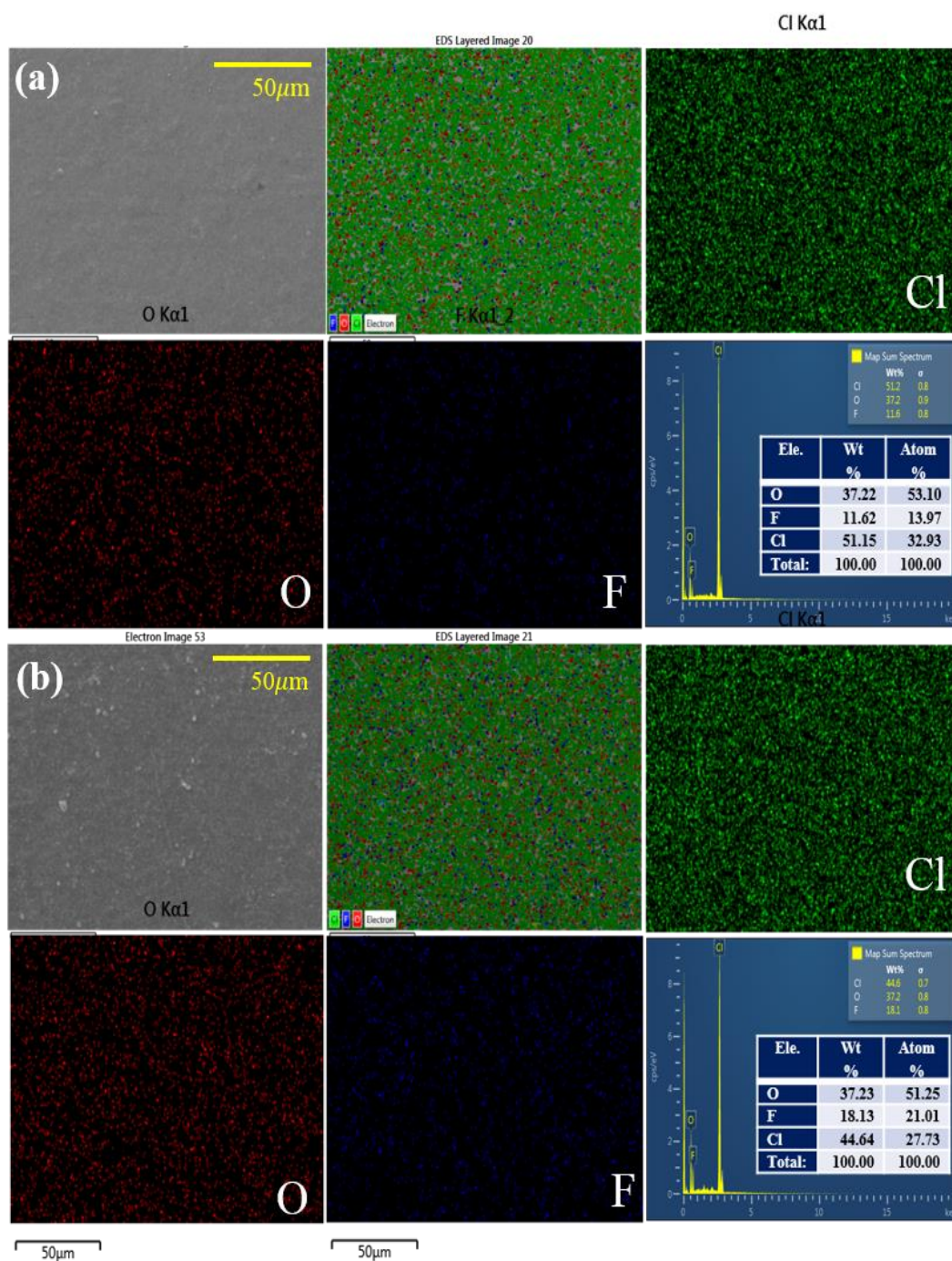


Figure 4.5 SEM image, mapping images, and EDS result of the (a) $\text{Li}_2(\text{OH})_{0.9}\text{F}_{0.1}\text{Cl}$ and (b) $\text{Li}_2\text{OHCl}_{0.8}\text{F}_{0.2}$ pellets.

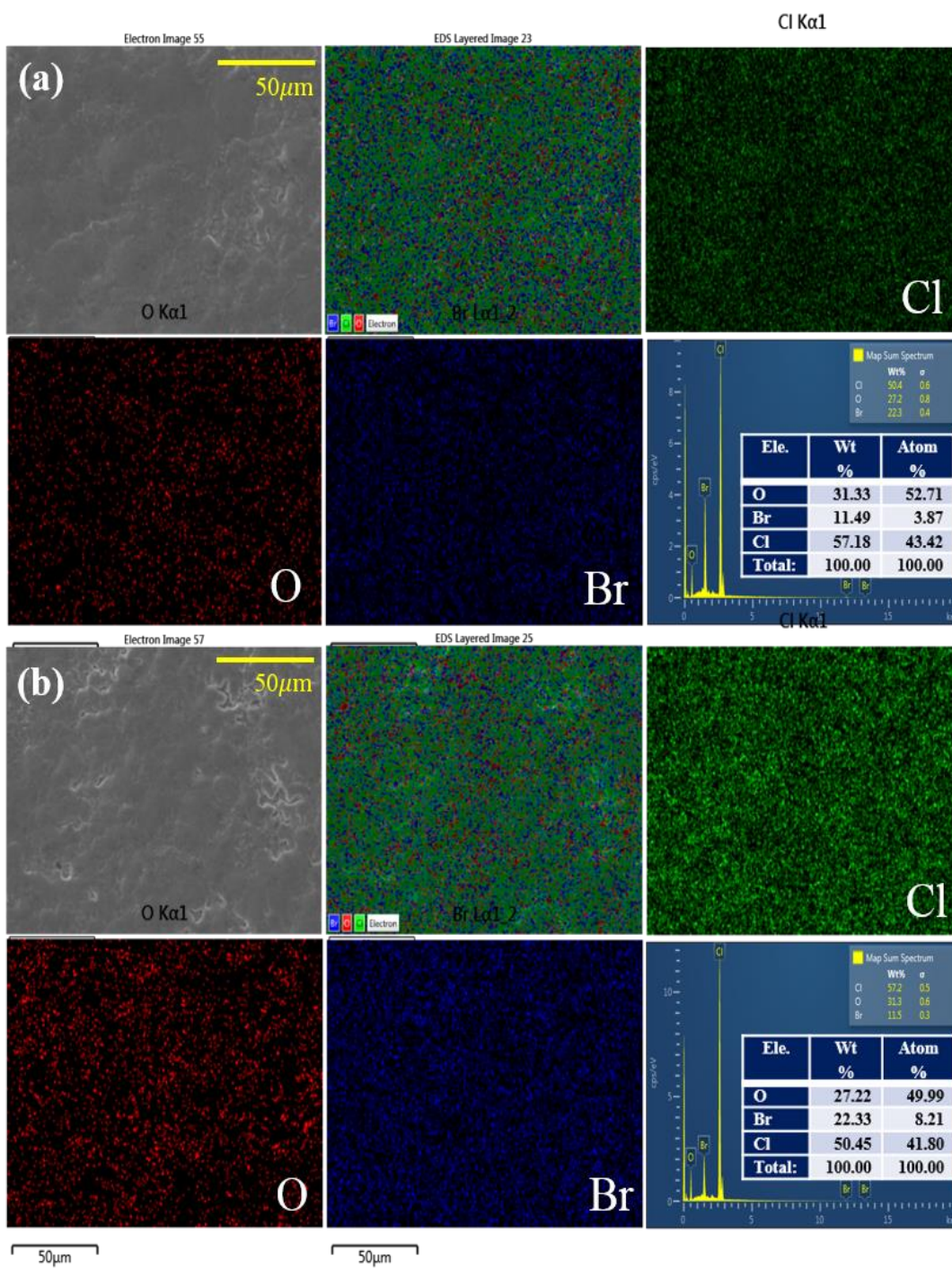


Figure 4.6 SEM image, mapping images, and EDS result of (a) the $\text{Li}_2(\text{OH})_{0.9}\text{Br}_{0.1}\text{Cl}$ and (b) $\text{Li}_2\text{OHBr}_{0.8}\text{F}_{0.2}$ pellets.

4-3-2. Electrochemical analysis

Figure 4.7 (a) exhibited the result of cyclic voltammetry for the symmetric cell Li/electrolytes/SUS at a scan rate 0.5 mV/s in a voltage range -1V to 6V (A: Li_2OHCl , B: $\text{Li}_2(\text{OH})_{0.9}\text{F}_{0.1}\text{Cl}$, C: $\text{Li}_2\text{OHCl}_{0.8}\text{F}_{0.2}$, D: $\text{Li}_2(\text{OH})_{0.9}\text{Br}_{0.1}\text{Cl}$, and E: $\text{Li}_2\text{OHCl}_{0.8}\text{Br}_{0.2}$). The inset in Figure 4.7 (a) is magnified reflections in the steady state condition 1.70V to 2.25V. All electrolytes showed the twin peaks, which are the oxidation reaction of Li metal and the SEI formation in the range of -0.05V to 1.5V. When comparing the current peaks in the reaction voltage range, the antiperovskites with F and Br substituted were lower than Li_2OHCl . The current intensity increases in the order of $\text{Li}_2\text{OHCl} > \text{Li}_2\text{OHCl}_{0.8}\text{Br}_{0.2} > \text{Li}_2(\text{OH})_{0.9}\text{Br}_{0.1}\text{Cl} > \text{Li}_2(\text{OH})_{0.9}\text{F}_{0.1}\text{Cl} > \text{Li}_2\text{OHCl}_{0.8}\text{F}_{0.2}$, which explains that the electrochemical stability of the substituted materials is more improved than that of Li_2OHCl .

Hebb-Wagner polarization curves obtained from the cell Li/ Li_2OHCl /SUS in Figure 4.7 (b). the polarization curve was plotted as a function of the current value generated in the steady state range 1.70V to 2.25V. From the slope of the linear function, which means the derivative $\frac{\partial I}{\partial V}$ of this graph, the electrical conductivities were calculated in Table 4.3. The calculated electrical conductivity increased in the order of $\text{Li}_2\text{OHCl} > \text{Li}_2\text{OHCl}_{0.8}\text{Br}_{0.2} > \text{Li}_2(\text{OH})_{0.9}\text{Br}_{0.1}\text{Cl} > \text{Li}_2(\text{OH})_{0.9}\text{F}_{0.1}\text{Cl} > \text{Li}_2\text{OHCl}_{0.8}\text{F}_{0.2}$, indicating that the substituted solid electrolytes have more electrochemical properties than Li_2OHCl . These results including the results of XRD, FT-IR, and TGA exhibited that the orthorhombic structure of Li_2OHCl is transformed into a stable cubic state and the transition improve the chemical stability and electrochemical stability of the solid

electrolyte when the anions in Li_2OHCl are replaced with anions of different size.

Comparing the electrochemical stability with F and Br substitution, F substituted materials showed lower electrical conductivity than Br substituted solid electrolytes. This result is consistent with the results of XRD, FT-IR and TGA, which means that the electrochemical stability as well as the chemical stability are superior to those of Br substituted materials in proportion to the binary bond strength (Li-F and H-F vs Li-Br and H-Br). In the case of the electrochemical stability comparison with the substitution site, $\text{Li}_2(\text{OH})_{0.9}\text{Br}_{0.1}\text{Cl}$ showed better electrochemical stability than $\text{Li}_2\text{OHCl}_{0.8}\text{Br}_{0.2}$, depending on the current intensity and the calculated electrical conductivity results. However, in the case of the F substituted material, $\text{Li}_2\text{OHCl}_{0.8}\text{F}_{0.2}$ had a lower electrical conductivity than $\text{Li}_2(\text{OH})_{0.9}\text{F}_{0.1}\text{Cl}$, but the difference was not significant.

Table. 4.3 List of the calculated electronic conductivities of the antiperovskites.

	$\partial I / \partial V$ (A/V)	A (cm ²)	d (cm)	σ_e (S/cm)
Li ₂ OHCl	1.36 x 10 ⁻⁷		0.062	1.05 x 10 ⁻⁹
Li ₂ (OH) _{0.9} F _{0.1} Cl	1.65 x 10 ⁻⁸	8.038	0.058	1.19 x 10 ⁻¹⁰
Li ₂ OHCl _{0.8} F _{0.2}	3.16 x 10 ⁻⁸		0.057	2.24 x 10 ⁻¹⁰
Li ₂ (OH) _{0.9} Br _{0.1} Cl	3.32 x 10 ⁻⁸		0.060	2.44 x 10 ⁻¹⁰
Li ₂ OHCl _{0.8} Br _{0.2}	2.96 x 10 ⁻⁸		0.062	2.36 x 10 ⁻¹⁰

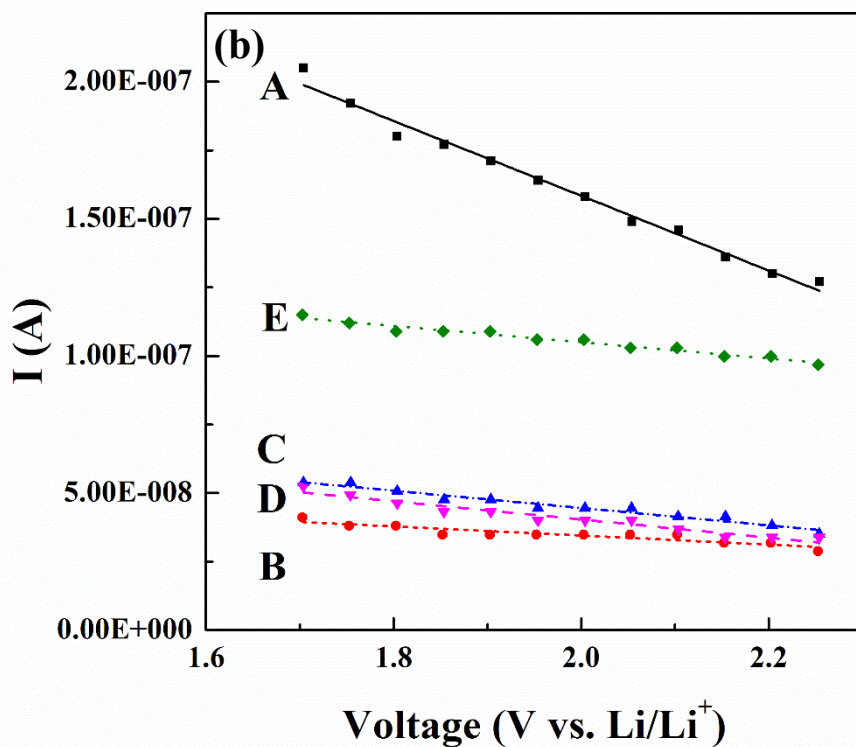
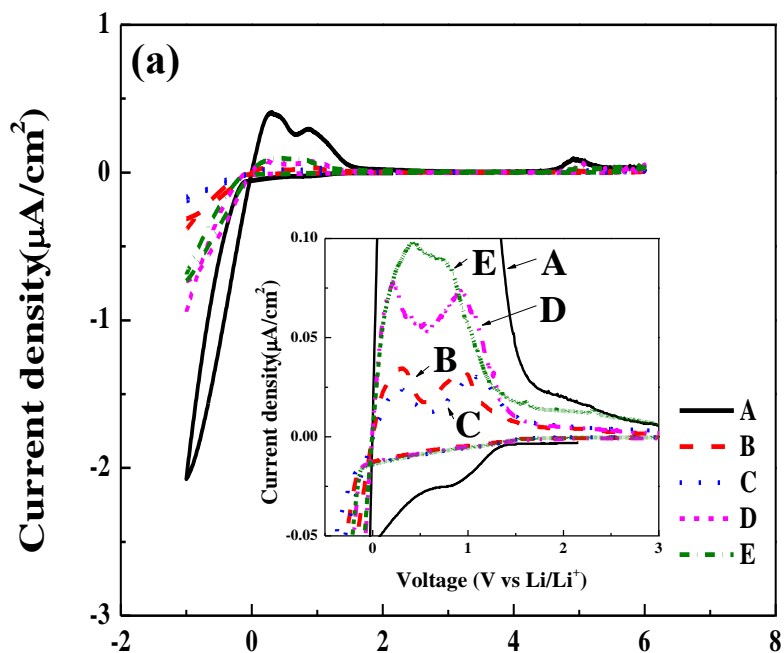


Figure 4.7 (a) Cyclic voltammetry for Li_2OHCl at a scan rate 0.5 mV/s from -1V to 6V and (b) the Hebb-Wagner polarization curves obtained from the cell $\text{Li}/\text{Li}_2\text{OHCl}/\text{SUS}$ (A: Li_2OHCl , B: $\text{Li}_2(\text{OH})_{0.9}\text{F}_{0.1}\text{Cl}$, C: $\text{Li}_2\text{OHCl}_{0.8}\text{F}_{0.2}$, D: $\text{Li}_2(\text{OH})_{0.9}\text{Br}_{0.1}\text{Cl}$, and E: $\text{Li}_2\text{OHCl}_{0.8}\text{Br}_{0.2}$).

To analysis the electrochemical stability and self-stabilizing of the substituted antiperovskites, DC-cycling measurements were performed by using the symmetric cell of Li/electrolytes/Li by applying a constant direct current 1.0 mA/cm^2 for 72 hours at 140°C (Figure 4.8). Although there is no significant difference in voltage variation, the F and Br doped antiperovskites exhibited stable voltage flow while Li_2OHCl pellet showed initial voltage increase. These results are due to the improved electrochemical stabilities of the substituted antiperovskites by the structural transition to the stable cubic phase as F and Br substitution proved by the results of XRD, FT-IR, TGA, and DSC. Comparison with F and Br substitution, the difference in voltage change is not clear, but for F substituted materials, it shows a more stable voltage flow than Br substituted materials. The difference in electrochemical stability depending on the size of the halide ion may be explained by the calculated band gap difference. In previous studies, the bandgaps of Li_3OCl and Li_3OBr were calculated to be 6.39 and 5.84 eV, respectively, which is proportional to the Li-Cl and Li-Br bond intensities. As a result, the F and Br substitution also means that the electrochemical stability is different due to the O-Li-F and O-Li-Br bond strength differences or O-H-F and O-H-Br bond strengths. Electrochemical stability by the substitution sites is difficult to compare because there is almost no change in the voltage of the antiperovskite electrolytes.

To analysis the composition of the SEI layer formed after the DC-cycling tests, SEM and EDS analysis were performed. From the results of SEM-EDS and mapping images in Figure 4.9 (a) $\text{Li}_2(\text{OH})_{0.9}\text{F}_{0.1}\text{Cl}$, (b) $\text{Li}_2\text{OHCl}_{0.8}\text{F}_{0.2}$, (c) $\text{Li}_2(\text{OH})_{0.9}\text{Br}_{0.1}\text{Cl}$, and (d) $\text{Li}_2\text{OHCl}_{0.8}\text{Br}_{0.2}$, it was confirmed that all SEI layers were mostly composed of Li_2O , while the materials such as LiCl, LiF, and LiBr were not observed. These results explain that the halogens in the antiperovskites were not react with Li-metal.

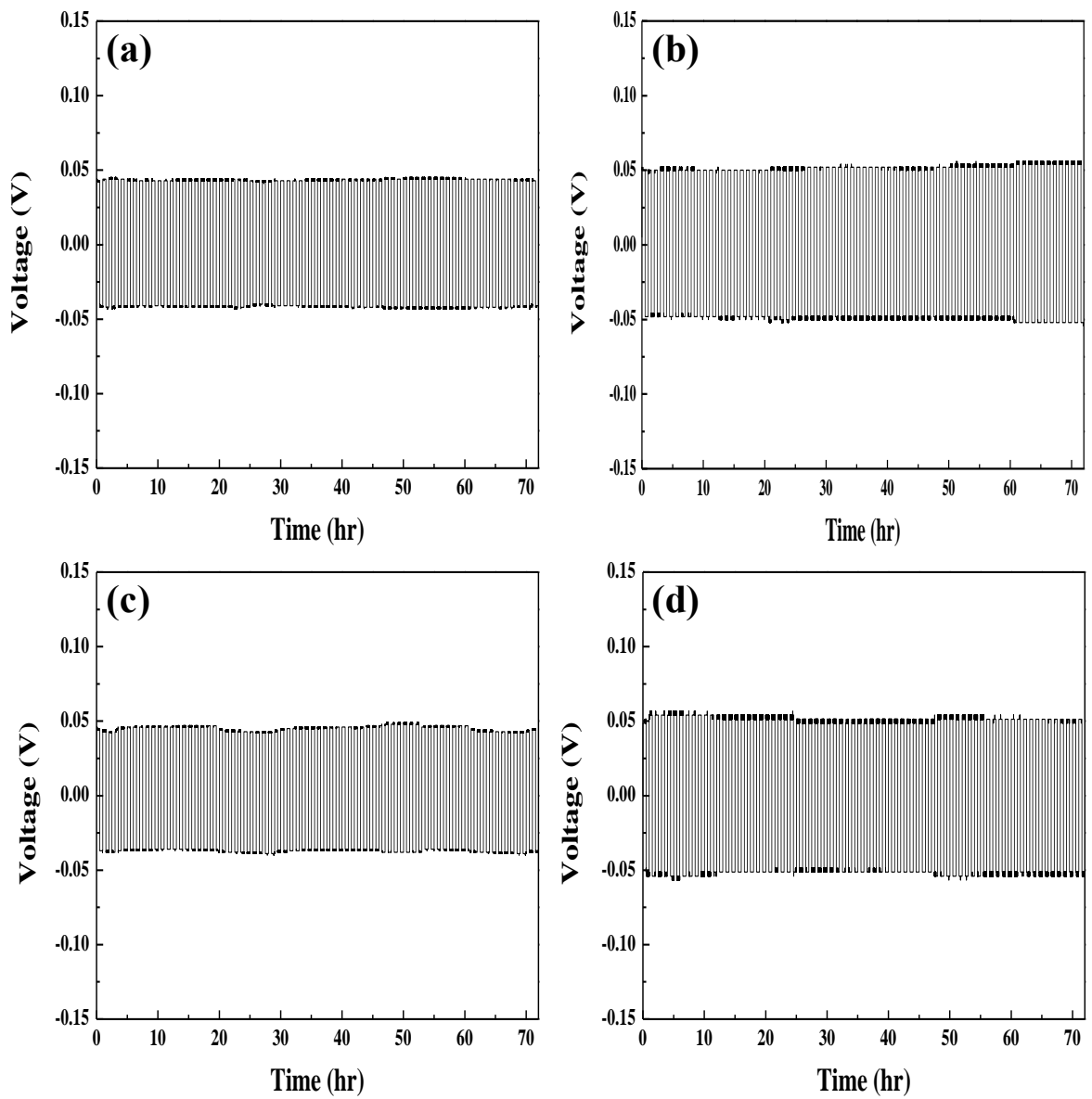


Figure 4.8 Results of DC-cycling tests for the symmetric cell Li/Li₂OHCl/Li with applied current density 1 mA/cm² at 140°C for 72hr (a) Li₂(OH)_{0.9}F_{0.1}Cl, (b) Li₂OHCl_{0.8}F_{0.2}, (c) Li₂(OH)_{0.9}Br_{0.1}Cl, and (d) Li₂OHCl_{0.8}F_{0.2}.

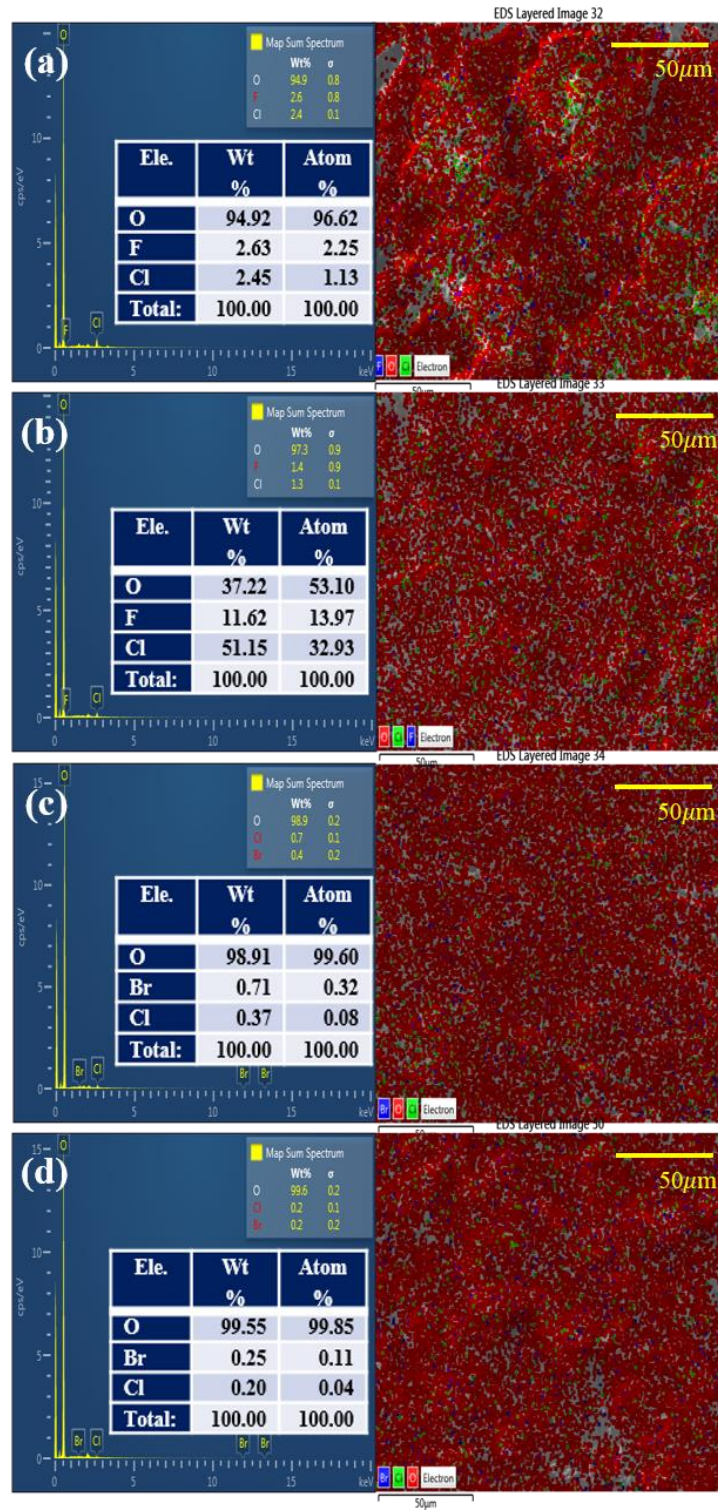


Figure 4.9 Results of EDS and mapping images of the symmetric cell Li/electrolyte/Li after DC-cycling tests at 140°C: (a) $\text{Li}_2(\text{OH})_{0.9}\text{F}_{0.1}\text{Cl}$, (b) $\text{Li}_2\text{OHCl}_{0.8}\text{F}_{0.2}$, (c) $\text{Li}_2(\text{OH})_{0.9}\text{Br}_{0.1}\text{Cl}$, and (d) $\text{Li}_2\text{OHCl}_{0.8}\text{Br}_{0.2}$.

Figure 4.10 (a) is Nyquist plot from EIS measurements for the antiperovskite electrolytes at room temperature. The calculated Li^+ conductivities of the electrolytes are listed with the total resistance in Table. 4.4. When comparing the values of $\text{Li}_2(\text{OH})_{0.9}\text{F}_{0.1}\text{Cl}$ $7.59 \times 10^{-5} \text{ Scm}^{-1}$ with that of previous studies, the conductivities calculated in this study were slightly higher but is similar to the values of the studies. The conductivity of the electrolyte in the previous study is $3.5 \times 10^{-5} \text{ Scm}^{-1}$ [1]. The conductivity of this study is almost two times larger than that of previous study but the same order value with that of the study. In comparison with the conductivities, the value increases in the order of $\text{Li}_2(\text{OH})_{0.9}\text{Br}_{0.1}\text{Cl} > \text{Li}_2(\text{OH})_{0.9}\text{F}_{0.1}\text{Cl} > \text{Li}_2\text{OHCl}_{0.8}\text{Br}_{0.2} > \text{Li}_2\text{OHCl}_{0.8}\text{F}_{0.2} > \text{Li}_2\text{OHCl}$. This result demonstrates that the phase transition by the substitution with the Br and F improved the Li^+ conductivity of the Li_2OHCl electrolyte. The Li^+ conductivities of $\text{Li}_2(\text{OH})_{0.9}\text{F}_{0.1}\text{Cl}$, $\text{Li}_2\text{OHCl}_{0.8}\text{F}_{0.2}$, $\text{Li}_2(\text{OH})_{0.9}\text{Br}_{0.1}\text{Cl}$, and $\text{Li}_2\text{OHCl}_{0.8}\text{Br}_{0.2}$ were 8 times, 3 times, 13 times, and 5 times higher than that of Li_2OHCl , respectively. Also, it can be explained that the improved Li^+ conductivities of $\text{Li}_2(\text{OH})_{0.9}\text{Br}_{0.1}\text{Cl}$ and $\text{Li}_2\text{OHCl}_{0.8}\text{Br}_{0.2}$ are due to the larger interstitial site in the cubic antiperovskite structure of the electrolytes by the substitution with large Br for small OH and Cl. The high Li^+ conductivities of the Br doped materials may be attributed to the mismatching effect by the incorporation of larger Br ion in the 12-coordinated dodecahedral center A-sites [10]. Alternate Br with diverse ionic radii in the A⁻ sites within the three-dimensional lattice will provide much free space for the Li^+ ions to hop in and pass through by interstitial route, i.e. Frenkel style [17]. This result can also be explained by comparing the Li^+ conductivities of $\text{Li}_2(\text{OH})_{0.9}\text{F}_{0.1}\text{Cl}$ and $\text{Li}_2(\text{OH})_{0.9}\text{Br}_{0.1}\text{Cl}$. When the smaller F and larger Br than OH are substituted for OH in Li_2OHCl , the conductivity of the $\text{Li}_2(\text{OH})_{0.9}\text{Br}_{0.1}\text{Cl}$ is about 2.8 times larger than that of

$\text{Li}_2(\text{OH})_{0.9}\text{F}_{0.1}\text{Cl}$. It means that the conductivity of Li_2OHX type materials is also can be improved by a larger halogen substitution like Li_3OX type materials. Another reason for the improved ionic conduction is that the activation energy for Li^+ diffusion is reduced as formed bonds such as Li-Br in $\text{Li}_2(\text{OH})_{0.9}\text{Br}_{0.1}\text{Cl}$ and $\text{Li}_2\text{OHCl}_{0.8}\text{Br}_{0.2}$. By the formation the weaker Li-Br bond than Li-Cl, lithium ion can be diffused better than LOC by phonon softening [3, 4]. Unlike the Br substituted materials, the improved Li^+ conductivity of $\text{Li}_2(\text{OH})_{0.9}\text{F}_{0.1}\text{Cl}$ is due to the reduction in the concentration of OH in Li_2OHCl . The Li^+ diffusion is interrupted by the coulombic repulsion and steric hindrance of the H^+ ions with a fixed O-H-X hydrogen bond [1]. Therefore, the Li^+ can be diffused well by decreasing the concentration of H^+ in spite of the smaller F substitution. Also, $\text{Li}_2(\text{OH})_{0.9}\text{F}_{0.1}\text{Cl}$ showed higher ionic conductivity than $\text{Li}_2\text{OHCl}_{0.8}\text{Br}_{0.2}$. It proves that the OH concentration has a greater effect on improving Li^+ conductivity of Li_2OHX type antiperovskite materials than the interstitial size of the Li_2OHCl crystal structure. In the case of the Li^+ conductivity of $\text{Li}_2\text{OHCl}_{0.8}\text{F}_{0.2}$, because the material did not apply the three factors for improving Li^+ conductivity described above explanation, it may be because of simplified Li^+ pass by the phase transition from orthorhombic to stable cubic structure. These results can also be explained by the calculated activation energy for Li^+ migration in Figure 4.10 (b) and Table. 3. The Arrhenius plots and activation energy was obtained from the Nyquist plots of the antiperovskite electrolytes with a range of the temperature from 25°C and 145°C. The activation energy from the plots increases in the order of $\text{Li}_2(\text{OH})_{0.9}\text{Br}_{0.1}\text{Cl} > \text{Li}_2(\text{OH})_{0.9}\text{F}_{0.1}\text{Cl} > \text{Li}_2\text{OHCl}_{0.8}\text{Br}_{0.2} > \text{Li}_2\text{OHCl}_{0.8}\text{F}_{0.2} > \text{Li}_2\text{OHCl}$. These results are correct with the order of the Li^+ conductivities.

Table. 4.4 Calculated Li⁺ conductivities and activation energies of the antiperovskite materials.

	Resistance (Ω)	Li⁺ conductivity (Scm^{-1})	E_a (eV)
Li ₂ OHCl	30404	9.20×10^{-6}	0.59
Li ₂ (OH) _{0.9} F _{0.1} Cl	5112	7.59×10^{-5}	0.53
Li ₂ OHCl _{0.8} F _{0.2}	13112	3.00×10^{-5}	0.57
Li ₂ (OH) _{0.9} Br _{0.1} Cl	3284	1.21×10^{-4}	0.51
Li ₂ OHCl _{0.8} Br _{0.2}	8774	4.37×10^{-5}	0.56

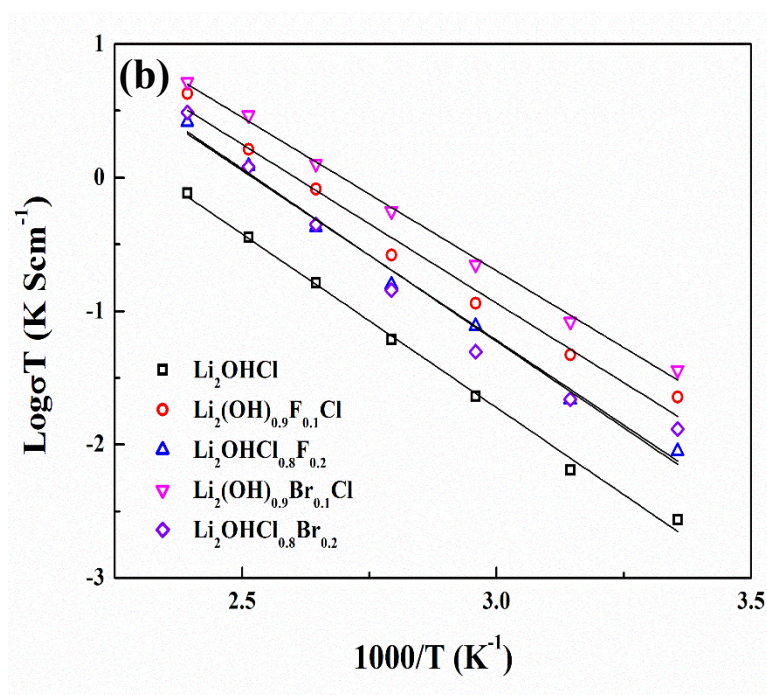
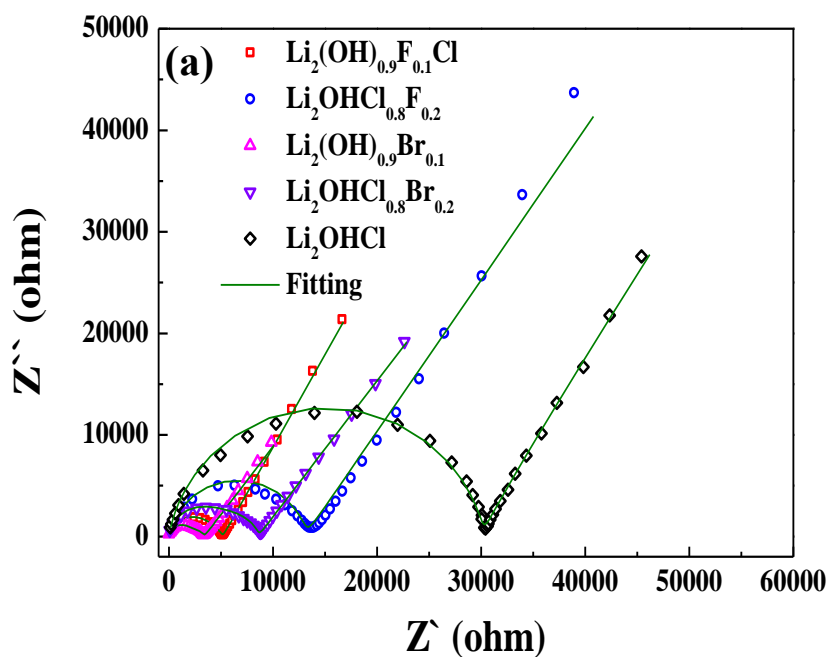


Figure 4.10 Results of (a) Nyquist plot from EIS measurements for the antiperovskite electrolytes and (b) Arrhenius plot of the total conductivity of the antiperovskite materials between 25°C and 145°C with In foil as electrodes; the activation energy E_a is derived by linear fitting of $\text{log} \sigma T$ versus $1/T$.

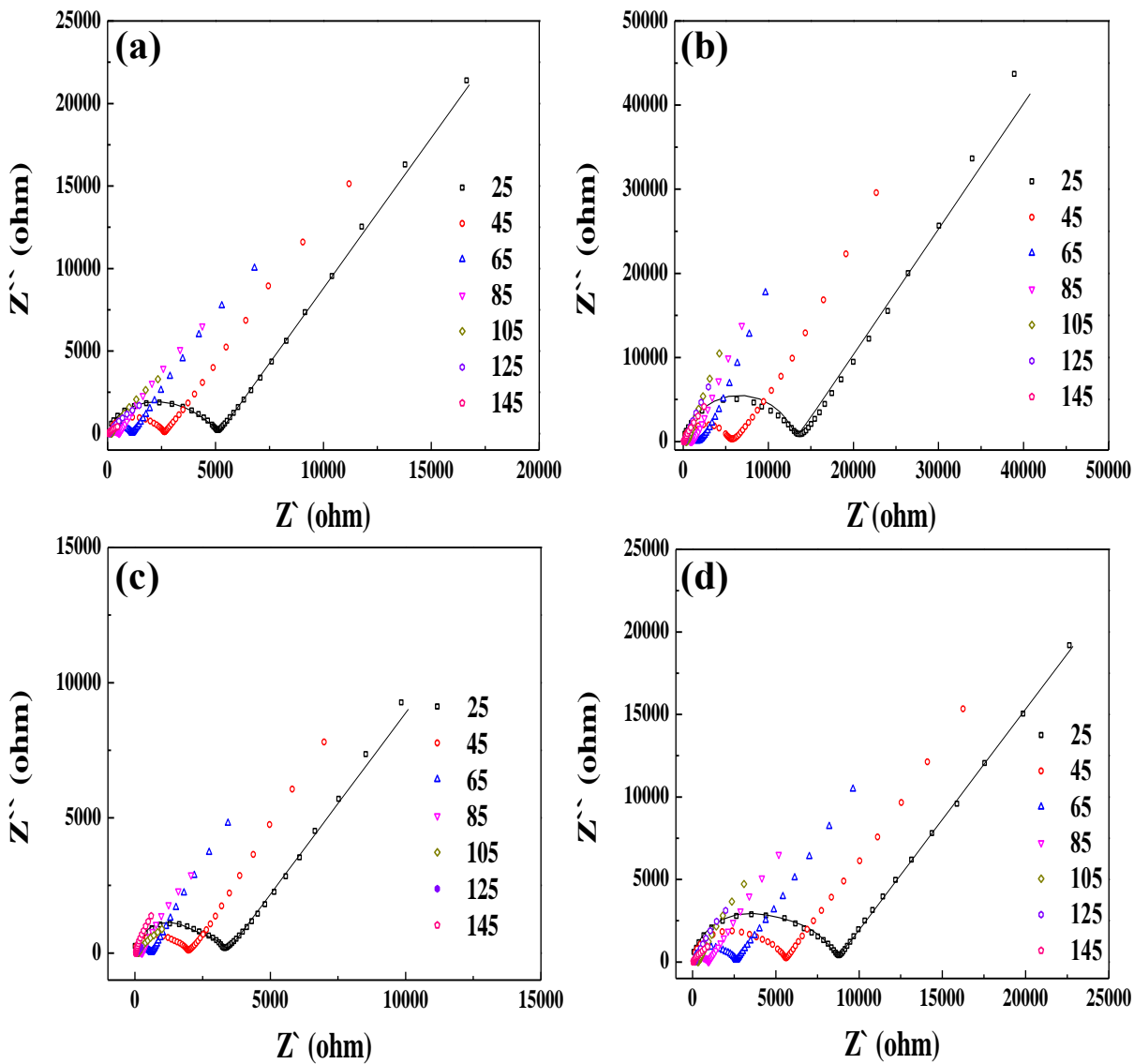


Figure 4.11 Results of Nyquist plot from EIS measurements for (a) $\text{Li}_2(\text{OH})_{0.9}\text{F}_{0.1}\text{Cl}$, (b) $\text{Li}_2\text{OHCl}_{0.8}\text{F}_{0.2}$, (c) $\text{Li}_2(\text{OH})_{0.9}\text{Br}_{0.1}\text{Cl}$, and (d) $\text{Li}_2\text{OHCl}_{0.8}\text{Br}_{0.2}$ with a range of the temperature from 25°C and 145°C.

4-4. Conclusion

From XRD and DSC results, it was confirmed that the structure of Li_2OHCl was transitioned from the orthorhombic phase to the pseudo cubic phase by substitution of F and Br. From the TGA data, it was observed that the melting points of the substituted materials were lower than that of Li_2OHCl when the phase transition occurred. The structure, thermal properties, and bond strength dependence by the substituted halogen species and substitution site were confirmed from the peak shift of XRD pattern, melting point from DSC, mass loss calculated by TGA measurement, and OH peak change in FT-IR spectra. As the results, the F substituted material showed more stable thermal properties due to the difference in ion binding strength depending on the sizes of F and Br, and the OH substituted materials showed more stable chemical properties than the Cl substituted materials. The F and Br substituted electrolytes showed improved electrochemical stability than Li_2OHCl from cyclic voltammetry, Hebb-Wagner polarization curve, and DC-cycling. F substituted materials showed lower electrical conductivity and stable electrochemical characteristics than those of Br substituted electrolytes. Analysis of the SEI layer formed after DC-cycling tests was carried out from SEM and EDS. From these results, it was confirmed that lithium-halogen materials including LiCl were hardly formed. As the results, structural stability, chemical stability, and electrochemical stability were improved by substituting F and Br for OH and Cl sites and it was shown that it could be applied to Li based batteries. Comparison with Li^+ conductivity of the electrolytes, the substituted materials showed improved Li^+ conductivity than Li_2OHCl by simple Li^+ pathway, large interstitial and

phonon softening, and higher Li^+ migration by decreasing OH concentration. Among the solid electrolytes, $\text{Li}_2(\text{OH})_{0.9}\text{Br}_{0.1}\text{Cl}$ showed higher Li^+ conductivity than those of the others because the conductivity was improved by all of the mechanisms. From the $\text{Li}_2(\text{OH})_{0.9}\text{F}_{0.1}\text{Cl}$ with higher Li^+ conductivity than that of $\text{Li}_2\text{OHCl}_{0.8}\text{Br}_{0.2}$, it was investigated that the Li^+ conductivity improvement of Li_2OHCl was more influenced by the OH concentration than the size of interstitial site and phonon softening effect.

References

- [1] Li, Y. *et al.* Fluorine Doped Antiperovskite Electrolyte for All Solid State Lithium Ion Batteries. *Angewandte Chemie International Edition* **55**, 9965-9968 (2016).
- [2] Zhang, J. *et al.* High pressure-high temperature synthesis of lithium-rich $\text{Li}_3\text{O}(\text{Cl}, \text{Br})$ and $\text{Li}_{3-x}\text{Ca}_{x/2}\text{OCl}$ antiperovskite halides. *Inorganic Chemistry Communications* **48**, 140-143 (2014).
- [3] Emly, A., Kioupakis, E. & Van der Ven, A. Phase stability and transport mechanisms in antiperovskite Li_3OCl and Li_3OBr superionic conductors. *Chemistry of Materials* **25**, 4663-4670 (2013).
- [4] Lu, Z. *et al.* Defect chemistry and lithium transport in Li_3OCl antiperovskite superionic conductors. *Physical Chemistry Chemical Physics* **17**, 32547-32555 (2015).
- [5] Eilbracht, C., Kockelmann, W., Hohlwein, D. & Jacobs, H. Orientational disorder in perovskite like structures of $\text{Li}_2\text{X}(\text{OD})$ ($\text{X}=\text{Cl}, \text{Br}$) and $\text{LiBr}\cdot\text{D}_2\text{O}$. *Physica B: Condensed Matter* **234**, 48-50 (1997).
- [6] Li, S. *et al.* Reaction mechanism studies towards effective fabrication of lithium-rich antiperovskites Li_3OX ($\text{X}=\text{Cl}, \text{Br}$). *Solid State Ionics* **284**, 14-19 (2016).
- [7] Braga, M., Ferreira, J. A., Stockhausen, V., Oliveira, J. & El-Azab, A. Novel Li_3ClO based glasses with superionic properties for lithium batteries. *Journal of Materials Chemistry A* **2**, 5470-5480 (2014).
- [8] Luo, Y.-R. *Comprehensive handbook of chemical bond energies*. (CRC press, 2007).
- [9] Hood, Z. D., Wang, H., Samuthira Pandian, A., Keum, J. K. & Liang, C. Li_2OHCl crystalline electrolyte for stable metallic lithium anodes. *Journal of the American Chemical Society* **138**, 1768-1771 (2016).
- [10] Zhao, Y. & Daemen, L. L. Superionic conductivity in lithium-rich antiperovskites. *Journal of the American Chemical Society* **134**, 15042-15047 (2012).

Chapter 5. Summary

We studied the possibility of Li_2OHCl , which is easy to synthesis as a solid electrolyte. To overcome the low ionic conductivity of the Li_2OHCl , we have studied both phase transition of the Li_2OHCl by the halogen anion substitution such as the F and Br substitution for OH and Cl site and a mechanism for improving Li^+ conductivity by the size effects of the substituted species and substituted site. In addition, the mechanism of chemical and electrochemical stability enhancement of Li_2OHCl materials by substitution species and sites was studied.

First, we studied Li_2OHCl as the base material in this study. As the results, the phase of Li_2OHCl was single orthorhombic structure. The materials showed mass loss of 11.38 wt% from TGA and low melting temperature 299°C . The Li_2OHCl pellet exhibited the stable electrochemical stability from cyclic voltammetry and DC-cycling and low Li^+ conductivity $9.20 \times 10^{-6} \text{ Scm}^{-1}$. After the DC-cycling tests, it was explained that Li_2OHCl is reacted with Li metal and generate Li_2O (99%) than LiCl . Comparison with previous study, we could know the basic experiments were well applied.

Second, we investigated $\text{Li}_2(\text{OH})_{0.1}\text{F}_{0.9}\text{Cl}$, $\text{Li}_2\text{OHCl}_{0.8}\text{F}_{0.2}$, $\text{Li}_2\text{OHCl}_{0.8}\text{Br}_{0.2}$, and $\text{Li}_2\text{OHCl}_{0.8}\text{F}_{0.2}$. From XRD, TGA, and so on, we observed that the phase of the substituted materials transferred from orthorhombic to stable cubic. Also, the chemical stabilities of the materials were improved in comparison with Li_2OHCl . From electrochemical experiments, the materials showed improved electrochemical stability and Li^+ conductivity. Compare to the electrochemical stability and electrical

conductivity, F substituted electrolytes showed the most stability and lowest electronic conductivity due to the stable binary bonds such as Li-F and H-F. Unlike the electrochemical stability, the Li^+ conductivity increased as like $\text{Li}_2\text{OHCl}_{0.8}\text{Br}_{0.2} > \text{Li}_2(\text{OH})_{0.1}\text{F}_{0.9}\text{Cl} > \text{Li}_2\text{OHCl}_{0.8}\text{F}_{0.2} > \text{Li}_2\text{OHCl}_{0.8}\text{F}_{0.2}$. From the results, we could analyze that the results are due to phonon softening effect and larger interstitial size of Br substituted materials than those of F substituted. Also, we were able to know that Li^+ conductivity improvement of Li_2OHCl was more influenced by the OH concentration than the size of interstitial site and phonon softening effect when comparing the Li^+ conductivity of $\text{Li}_2(\text{OH})_{0.1}\text{F}_{0.9}\text{Cl}$ and $\text{Li}_2\text{OHCl}_{0.8}\text{F}_{0.2}$.